U i T

**THE ARCTIC
UNIVERSITY
OF NORWAY**

Faculty of Science and Technology
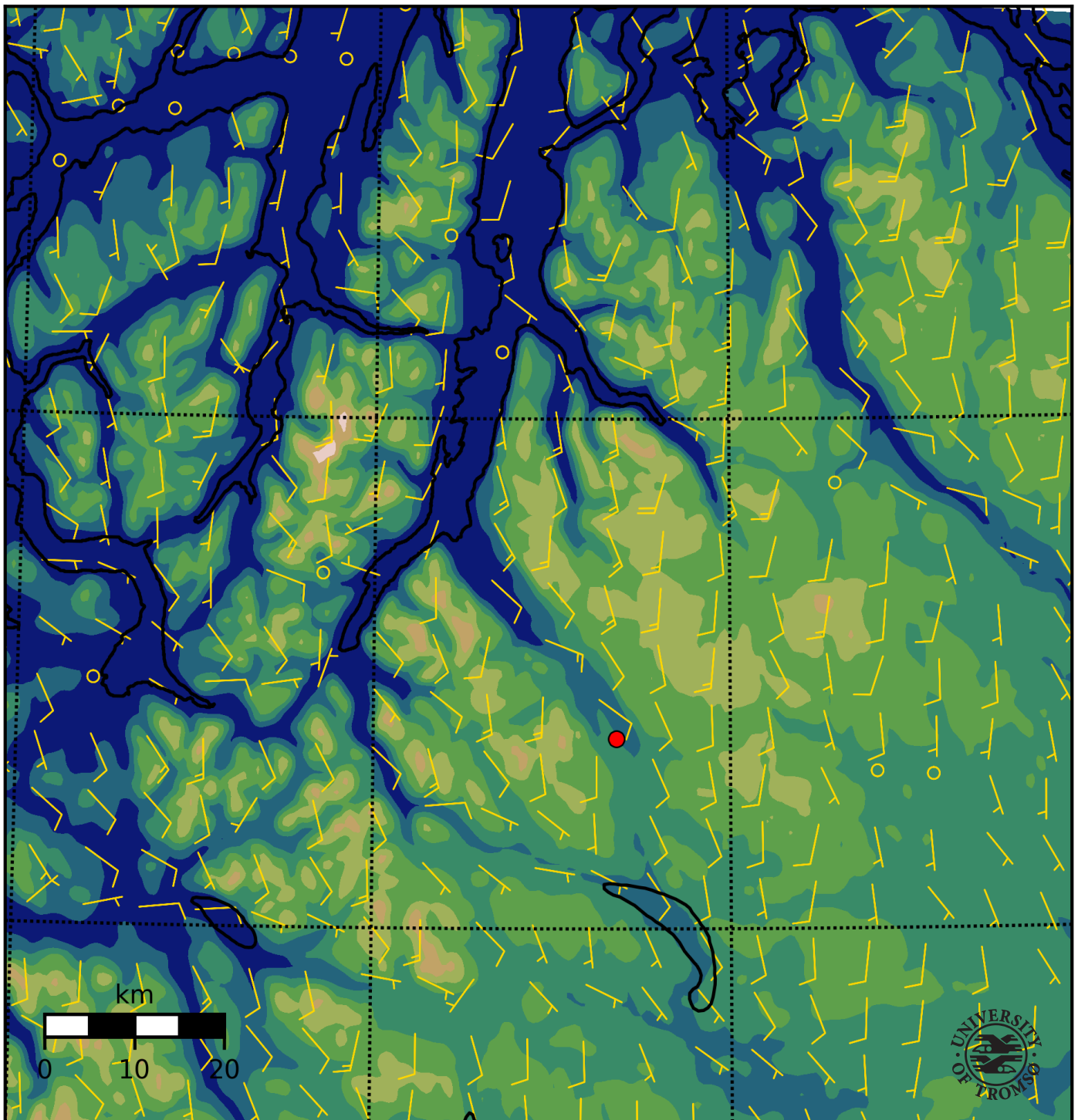Department of Physics and Technology

Wind resource assessment using mesoscale modelling

-A case study at the potential wind farm site Rieppi
—

Torgeir Blæsterdalen
FYS-3941 Master's thesis in applied physics and mathematics, June 2016

km

0   10   20

The cover image shows horizontal wind (yellow wind barbs) and the topography surrounding the Rieppi site (red dot).

Abstract

The growing wind power industry, increased occurrence of extreme weather, and the need for becoming independent of fossil fuels motivate the research on accurate simulation of near-surface wind. The aim of this study is wind resource assessment at the potential wind park site Rieppi, using two on-site measurement masts, simulations from the Weather Research and Forecasting (WRF) model, and ERA-Interim reanalysis data from the European Centre for Medium-range Weather Forcasts (ECMWF). The main focus has been on 2014 for investigating monthly and seasonal behaviour of the wind. A climatology of the period 2004-2013 will be used for assessing the representativeness of 2014.

The on-site measurements were compared to ERA-Interim data and WRF simulations in terms of Root Mean Square Error, correlation and Bias. Weibull distribution based on wind speed histograms and wind roses were also used for comparing the three data sources and for validating the WRF model.

The obtained differences between ERA-Interim and the on-site measurements, in terms of horizontal wind speeds and prevailing wind directions, show little consistency. The obtained wind roses from ERA-Interim show little agreement to the prevailing on-site wind directions. In contrast, despite a systematically underrepresentation of strong and gusty wind speeds, the WRF model provides more accurate simulation results than the ERA-Interim data. The simulated wind directions and low to moderate wind speeds show high consistency to the on-site measurements. The local wind resource maps obtained by WRF provide valuable information about the local wind patterns in the area. These factors show that the WRF model is a versatile and useful tool for early stage wind resource assessment, even in complex terrains like at the Rieppi site.

Acknowledgements

Contents

List of Figures

List of Tables

Abbreviations

ACM2 Asymmetric convective model, version 2. PBL scheme.

a.g.l Above ground level

ARW Advanced Research WRF (dynamical WRF solver)

BouLac Bougeaukt-Lacarrére. PBL scheme

CFL Courant-Fredrichs-Lewy. Stability condition for numerical integration.

ECMWF European Centre for Medium-range Weather Forcasts

ERA ECMWF reanalysis

ERA-Interim ECMWF global atmospheric reanalysis from January 1979, continuously updated in real time.

HWE High wind event

Lidar Light detection and ranging

LSM Land-surface model

MRF Medium Range Forecast

MSL Mean sea level

MYJ Mellor-Yamada-Janic. PBL scheme

NCAR National Center for Atmospheric Research

NCL NCAR Common Language

NMM Nonhydrostatic Mesoscale Model (dynamical WRF solver)

ODE Ordinary differential equation

PBL Planetary boundary layer

pdf probability density function

QNSE Quasi-normal scale elimination. PBL scheme

RK Runge-Kutta. Numerical integration method. Appended numbers, e.g. RK3 gives the order, i.e. RK3 is 3rd order Runge-Kutta.

RMS Root mean square

RMSE Root mean square error

SL Surface layer

TKE Turbulent kinetic energy. Collective term for PBL schemes.

UW University of Washington Moist Turbulence. PBL scheme.

WRF Weather research and forecasting model

WPS WRF preprocessing system

WSM5 WRF Single-Moment 5-class. Microphysics scheme.

YSU Yonsei University. PBL scheme

Nomenclature

In this thesis, vectors will consistently be denoted by fat, italic types and scalars in normal, italic types. Mathematical operators are in upright letters. The list below contains the symbols used in the thesis sorted in latin symbols, greek symbols and math operators. Different meaning of the symbols are separated by a semicolon.

$a = \bar{a} + a'$ Variable expressed as a sum of a base-state and a perturbed value

A Area

c_p Heat capacity at constant pressure

$c_{p,d}$ heat capacity for dry air at constant pressure

$c_{p,w}$ heat capacity for water vapour at constant pressure

e Turbulent kinetic energy per unit mass

E_k Kinetic energy

f Coriolis parameter; Also used for functions in general

$\boldsymbol{g}$ Acceleration vector due to gravity

g_0 Constant vector acceleration due to gravity

$\boldsymbol{i}, \boldsymbol{j}, \boldsymbol{k}$ Unit vectors in x, y, z direction

$\dot{m}$ Mass flow rate

L Horizontal length scale

p pressure

P Power

$\tilde{P}$ Power density, i.e. power divided by unit area

q Water content in air

Q Heat

R Gas constant. R_d gas constant for dry air. R_w gas constant for water vapour.

Re Reynolds number

Ro Rossby number

s^2 Estimated variance. s estimated standard deviation

T Temperature

$\boldsymbol{u} = (u, v, 0)$ Horizontal velocity; u and v is zonal and meridional direction

U Horizontal velocity scale

$\boldsymbol{v} = (u, v, w)$ 3-dimensional velocity; w is the vertical component of the velocity.

V Volume

$\dot{V}$ Volume flow rate

$\overline{x}$ Sample mean

α Inverse density; angle

β Rate of change of the Coriolis parameter with latitude

δ Infinitesimal change

Δ Change, e.g. $\Delta x = x_2 - x_1$

η Specific entropy; vertical levels

μ Viscosity; Theoretical mean

ν Kinematic viscosity, μ/ρ

λ Longitude

Ω Rotation vector

Φ Geopotential

ρ Density; Correlation coefficient

ϱ Chemical potential

σ^2 Theoretical variance. σ Theoretical standard deviation.

$\sum_i$ Sum with index i

Σ Covariance matrix

τ Stress tensor

θ Potential temperature

ϑ Latitude

$A^\top$ Transpose of matrix A

$\log(x)$ The natural logarithm of x

$\mathrm{Tr}(A)$ Trace of matrix A

∇_z Gradient operator at constant value of coordinate, e.g. $\nabla_z = \boldsymbol{i}\frac{\partial}{\partial x} + \boldsymbol{j}\frac{\partial}{\partial y}$

$\nabla\cdot$ Divergence operator

$\frac{\partial a}{\partial t}$ Partial derivative of a with respect to t

$\left(\frac{\partial a}{\partial t}\right)_b$ Partial derivative of a with respect to t at constant b

$\frac{\mathrm{d}}{\mathrm{d}t}$ Liebniz notation for derivation

$\frac{\mathrm{D}}{\mathrm{D}t}$ Material derivative

$\|\cdot\|_2$ 2-norm, e.g. $\|\boldsymbol{v}\|_2 = (\boldsymbol{v}^\top \boldsymbol{v})^{1/2}$

/1

Introduction

1.1   The need for accurate wind simulation

Rising energy demands [32] and an increased focus on global climate changes make renewable and sustainable energy alternatives a necessity for minimizing the global warming and becoming independent of fossil fuels.

As fossil fuels are the predominant global energy source, the replacement cannot be done by a single renewable energy source alone, as renewable energy only accounts for approximately 3.0% of the global power generation [9]. Fossil fuels have to be replaced by an agglomerate of sustainable alternatives. One of the fastest growing energy technologies the last decade is wind energy [8]. Accurate wind resource assessments are challenging due to the large temporal and spatial variations of the wind.

The potential wind farm site investigated in this thesis is approximately 300 km north of the Polar circle and located east of the Lyngen alps, in Troms county. The site will be referred to as Rieppi. The power company Troms Kraft AS has estimated a shortage of electrical power in Troms county over the past eleven years of approximately 871 GWh annually [71]. Because of the cold climate and the complex terrain surrounding Rieppi, assessing the available wind resource is a challenging and complex task. The cold climate can cause rime ice protrusion on the turbine blades which leads to reduced aerodynamical properties [34], material fatigue [26] and directly damage due to the ice [59]. Betz' limit tells us that the maximum wind energy an *ideal* wind turbine can

harvest is approximately 59% of the potential power in the wind [42]. The *realistic* amount of power depends on the choice of turbine, icing, wake effects from other turbines and most importantly the wind resource itself.

The investigation of a potential wind park site has to address the possibility of extreme winds that can damage the turbines and stall the power generation. The location of the wind farm should be chosen where there are little turbulence and strong, stable horizontal winds.

A very powerful tool in wind resource assessment and weather prediction in general, is the Weather Research and Forecasting (WRF) model. The model is the state-of-the-art model for mesoscale weather simulation [11]; [51]; [27]. In meteorology, mesoscale is used for the atmospheric phenomena that has a spatial horizontal resolution in the range 1 km to about 1000 km. Smaller and larger scales are often referred to as microscale and large scale (also referred to as synoptic scale) [66]. The resolution is flexible for global to local scale with emphasis on horizontal grid spacing of 1 to 100 km [49]; [77]. The model is open-source and therefore a flexible model that can be configured for various applications and thus it has a large spectrum of various physical, numerical and dynamical options for tailoring the model to be valid for very specific situations.

The location of a full-scale wind park will always be debated as modern turbines often have rotor diameters exceeding 100 meters and thus making a large encroachment in the nearby terrain [73]. A simulation tool that accurately depicts the local wind pattern is essential for planning efficient wind parks at the best possible location for accommodating the future energy demands.

1.2   Former research

The accurate characterization of the local wind resource is best surveyed using a comprehensive network of observational instruments that are instrumented for evaluating wind speeds [40]. The comprehensive network of high quality observations is a utopia, and the amount of such observations is limited in the northern part of Norway. At remote locations like off-shore, there might not be any available on-site measurements. A common method for initial evaluation of a wind resource is often a numerical weather prediction model [1]. The simulation results can then be used for ranking and selection of potential wind park sites.

In a study comparing WRF simulations to on-site measurements in Portugal, Poland and Romania, Soares et al. [67] found that the simulation results could

be adequate for wind resource assessment. Byrkjedal and Berge [10] found a good correlation between on-site observations and WRF simulations, although they pointed out that the WRF model seemed to overestimate wind speeds in complex terrain in general, but underestimating the wind speed at hilltops due to the smoothened model terrain.

The WRF model supports a broad range of physical, numerical and computational options. The diversity of these options makes it a complex task to select the best suited configuration options due to high-dimensional, multi-modal, non-linear physical interactions [55]. Because this thesis will focus on the near-surface wind, appropriate physical parameterizations will be important for simulating the winds in the boundary layer. The chosen height is 60 meters above ground level (abbreviated a.g.l.) which is a typical wind height considered by wind power studies [11].

As many physical processes like turbulence, cumulus convection and heat fluxes happen at smaller scales than the WRF model's temporal and spatial scale, they have to be parameterized [62]. The physics are divided into microphysics, cumulus parameterization, surface layer, land-surface model, planetary boundary layer (PBL) and radiation (long-wave and short-wave) [64]. All of these physical categories have a range of parameterization schemes which have to be determined. The parameterization schemes interact non-linearly with each other and with the dynamical WRF core. Sensitivity studies of the different parameterization schemes is an ongoing project and a large research field and while some parameterization schemes are best at some locations, they might might not be optimal for other locations with different climate and terrain.

1.3   Aim of the study

The aim of this study is to use data from on-site observations from two measurement masts, reanalysis data from the European Centre for Medium-range Weather Forcasts (ECMWF) and WRF simulations for making a wind resource assessment at the Rieppi site. The WRF model setup and its parameterizations will be explained and the model performance will be statistically evaluated. The main focus will be on mean horizontal wind speed, prevailing wind directions and the distribution of wind speeds. Other topics like temperature, turbulence and vertical wind fields will also be explored. Using on-site measurements and the WRF model for a whole year, I want to capture monthly and seasonal behaviour of the wind. A climatology for investigating the representativeness of 2014 will also be given.

Because the measurement masts only provides information about two points in the terrain, one motivation for using the WRF model is to create wind resource maps over the surroundings at the Rieppi site. The WRF model will be used for providing local wind resource maps for the site along with maps for turbulence in the surrounding area. The analysis of the varying wind patterns will aim at increasing the understanding of the wind resource at the Rieppi site and similar sites. If the WRF model shows satisfying results it could be used as a first-estimate of similar sites in arctic environments. If validated, the model can be used for providing information about sites where no on-site measurements are available, like remote land areas or off-shore locations.

1.4   Structure of the thesis

This thesis is structured in 6 chapters including the introduction.

Chapter 2 provides the relevant theory for the physics used in this thesis.

Chapter 3 presents the methodology for this thesis with describing the different sources of data and the statistical methods for comparing the wind data. A detailed description of the potential wind park site will be given is this chapter.

Chapter 4 describes the framework of the WRF model and some of its most important parameterizations used for running the simulations. The model configuration will be justified based on the findings by former sensitivity studies of the parameterization schemes.

Chapter 5 presents the results from the on-site observations, the data from the ECMWF and the WRF simulations. This chapter will also present comparisons and analysis of the data.

Chapter 6 will provide a summary of the wind simulations and some concluding remarks will be given. The end of Chapter 6 is dedicated to proposes for further work to extent and improve this study.

These six chapters make the main framework of this thesis. However, there are some topics like useful tables, statistical and physical derivations that are put in appendices at the end of the thesis. This is done for keeping a more concise text.

/2

Theoretical background

2.1 Conservation of momentum

One of the fundamental equations of fluid dynamics is the conservation of momentum. In certain forms, the momentum equations is referred to as the Navier-Stokes equations or the Euler equations and these are the cornerstone of fluid mechanics [12].

There are two reference frames for the rate of change of a fluid element. The fluid element in this context can be described as a small, indivisible fluid parcel having a fixed mass. The first reference frames are the Eulerian, where the reference frame is spatially fixed and the fluid flows though it. The other alternative is the Lagrangian, where the reference frame follows the fluid parcel [72]. The rate of change of the fluid's property (e.g. pressure or momentum) can be expressed as the material derivative (also called the Lagrangian derivative). The material derivative of a scalar b or vector $\boldsymbol{b}$ describes the rate of change in time of a parcel moving with velocity $\boldsymbol{v}$ and can be expressed

$$\frac{\mathrm{D}b}{\mathrm{D}t} = \frac{\partial b}{\partial t} + \boldsymbol{v} \cdot \nabla b \tag{2.1.1}$$

$$\frac{\mathrm{D}\boldsymbol{b}}{\mathrm{D}t} = \frac{\partial \boldsymbol{b}}{\partial t} + (\boldsymbol{v} \cdot \nabla)\boldsymbol{b}, \tag{2.1.2}$$

respectively. The first term on the right hand side is the local rate of change and the second term expresses advection.

5

The momentum of a fluid can be expressed as the mass times the fluid's velocity, namely $m\boldsymbol{v}$. The momentum-density field can therefore be expressed as ρv, where ρ is the density of the fluid. The total momentum of the fluid is therefore $\int_V \rho\boldsymbol{v}\mathrm{d}V$, where V is the fluids total volume. By Newtons second law, the rate of change of the fluid's momentum equals the force acting on it,

$$\frac{\mathrm{D}}{\mathrm{D}t}\int_V \rho\boldsymbol{v}\mathrm{d}V = \int_V F\mathrm{d}V. \tag{2.1.3}$$

By assuming that the density of the fluid is time-independent, Equation 2.1.3 can be rewritten as

$$\int_V \left(\rho\frac{\mathrm{D}\boldsymbol{v}}{\mathrm{D}t} - F\right)\mathrm{d}V = 0. \tag{2.1.4}$$

Since this can be performed for an arbitrary volume, the integrand must vanish, giving

$$\frac{\mathrm{D}\boldsymbol{v}}{\mathrm{D}t} = \frac{1}{\rho}(F_p + F_v + F_b), \tag{2.1.5}$$

where $F_p + F_v + F_b$ are the forces per volume acting on the fluid element, namely the pressure, the viscous force and body forces (e.g. gravitational forces) respectively.

The pressure force on a infinitesimal fluid parcel with surface element $\mathrm{d}S$ can be expressed

$$F = \oint_s p\mathrm{d}S, \tag{2.1.6}$$

where p is the pressure. By the divergence theorem, the pressure force can be re-expressed as

$$F = -\int_V \nabla p\mathrm{d}V \tag{2.1.7}$$

$$F_p = \frac{F}{V} = -\nabla p \tag{2.1.8}$$

where V is the volume encapsulated by the surface S.

For a Newtonian fluid, the viscous force per unit volume can be expressed $F_v = \mu\nabla^2\boldsymbol{v}$, where μ is the fluid's viscosity.

By inserting F_p and F_v, Equation 2.1.5 can be rewritten as

$$\frac{\mathrm{D}\boldsymbol{v}}{\mathrm{D}t} = \frac{1}{\rho}(\nabla + \mu\nabla^2\boldsymbol{v} + F_b) \tag{2.1.9}$$

$$\frac{\partial\boldsymbol{v}}{\partial t} + (\boldsymbol{v}\cdot\nabla)\boldsymbol{v} = -\frac{1}{\rho}\nabla p + v\nabla^2\boldsymbol{v} + F, \tag{2.1.10}$$

where the material derivative is expanded. Here $v \equiv \mu/\rho$ is the *kinematic viscosity*. The body forces is the gravitational acceleration vector.

Equation 2.1.10 is referred to as the Navier-Stokes equations. If the fluid is inviscid, the equation is reduced to the so-called Euler equations.

For a fluid in the rotating frame, the Navier-Stokes equation must include the Coriolis-term $f \equiv 2\Omega \sin \vartheta$ and the Eq. 2.1.10 becomes

$$\frac{\partial \boldsymbol{v}}{\partial t} + (\boldsymbol{v} \cdot \nabla)\boldsymbol{v} + f \times \boldsymbol{v} = -\frac{1}{\rho}\nabla p + \nu\nabla^2\boldsymbol{v} + \boldsymbol{F}. \qquad (2.1.11)$$

A derivation of the Coriolis parameter and the Coriolis force can be examined in Appendix A: *Coriolis force and the Coriolis parmater*.

2.2 Hydrostatic balance

The vertical component of the momentum equation (Eq. 2.1.11) is

$$\frac{\mathrm{D}w}{\mathrm{D}t} = -\frac{1}{\rho}\frac{\partial p}{\partial z} - g, \qquad (2.2.1)$$

where w is the vertical velocity of the fluid. The equation shows that the vertical acceleration is due to the gravitational force and the vertical pressure gradient force.

Typical scaling of the magnitude of the variables show that the vertical acceleration of the fluid ($\mathrm{D}w/\mathrm{D}t$) is small compared to the gravity g [72], and thus, the pressure gradient force and the gravity balances each other, yielding the equation

$$\frac{\partial p}{\partial z} = -\rho g. \qquad (2.2.2)$$

This relation is referred to as the *hydrostatic approximation* or *hydrostatic balance* [29]; [72]. The minus sign arises because the pressure decreases as the height increases. Although the gravitational acceleration changes with latitude and altitude, it is common to replace it with the constant g_0 which is the global average gravity at sea level ($\sim 9.81\mathrm{m/s}^2$) [44].

All physical constants used in this thesis is tabulated in Appendix B: *Physical constants*.

2.3 The equation of state

The relation of the pressure, temperature and density of a substance is an *equation of state* [12]. The equation of state can be expressed

$$p\alpha = RT, \qquad \text{or} \qquad p = \rho RT \qquad (2.3.1)$$

where ρ is the density of the fluid, α is the specific volume, T is the thermodynamic (absolute) temperature and R is the gas constant for the gas in question given as $R = nk$, where n is the number of molecules per unit mass. k is the Bolzmann's constant.

Gases that obey the equation of state are referred to as *ideal gases* [12] and thus the equation of state is sometimes referred to as the *ideal gas law*. The air in the Earth's atmosphere is close to the ideal gas [72].

The so-called *specific* gas constant can be expressed as $R_s = c_p - c_v$ where c_p and c_v are the fluids heat capacity at constant pressure and volume respectively. The heat capacities are derived in Appendix C: *Atmospheric thermodynamics*. The gas constant for moist air can be expressed

$$R = R_d(1 - q) + R_w q, \tag{2.3.2}$$

where q is the amount of water vapour in the air, R_d and R_w are the gas constants for dry air and water vapour respectively.

By declaring that the atmosphere consists of dry air plus moist air from water vapour, the specific heat at constant pressure can be expressed

$$c_p = c_{p,d}(1 - q) + c_{p,w} q, \tag{2.3.3}$$

where $c_{p,d}$ and $c_{p,w}$ is the specific heat for dry air and water vapour at constant volume.

2.4   Geometric height from barometric pressure

Pressure is force per area, and the atmospheric pressure is the weight of the fluid column above an area. To derive a relation between the atmospheric pressure and the geometric height above sea level, I will start out by making some simplifying assumptions:

   i) The fluid is only composed of dry air and its composition does not change.

  ii) The fluid is in hydrostatic balance.

 iii) The temperature throughout the fluid column is constant.

Dividing the hydrostatic balance obtained in the last subsection (Eq. 2.2.2) by the ideal gas law (Eq. 2.3.1) gives

$$\frac{\mathrm{d}p}{p} \approx -\frac{g\,\mathrm{d}z}{RT}. \tag{2.4.1}$$

Integrating (2.4.1) gives the barometric pressure

$$p(z) \approx p_0 \exp\left(-\frac{gz}{RT}\right), \tag{2.4.2}$$

where p_0 is the surface pressure. From this equation, it is clear that the pressure decreases exponential with altitude. Solving with respect to height gives the approximate geometric height of a given pressure level above ground level as a function of pressure, namely

$$z(p) \approx -\frac{RT}{g} \log\left(\frac{p(z)}{p_0}\right). \tag{2.4.3}$$

Both the temperature and the acceleration due to gravity is height dependent, but the temperature variations are small compared to the mean temperature ($\frac{dT}{T} \ll 1$). The gravity has very small deviations through the lower atmosphere.

Potential energy is the work required to raise an object to a certain height. According to Vallis [72], geopotential is the work required to raise an object of 1 kg to an altitude z in the atmosphere and can be described as

$$\Phi = gz. \tag{2.4.4}$$

2.5   Wind power

As mentioned in the introduction, the focus of this thesis is wind resource assessment. Because the wind power is the most central topic in planning a wind park, the wind power potential at the Rieppi site will also be considered in this thesis.

The kinetic energy in a volume flowing through a cross-section A can be expressed $E = 1/2m\boldsymbol{u}^2$ with the corresponding power

$$P = \frac{1}{2}\rho A \boldsymbol{u}^3, \tag{2.5.1}$$

where $\boldsymbol{u}$ is the vertical wind velocity perpendicular to the cross-section A. Because the power is proportional to the cube of the wind speed, small variations in the wind speed leads to large variations in the power output.

Note that power is denoted by capital p and pressure is denoted by lower-case p. The *power density* is the power per area.

An illustration of a power curve is sketched in Fig. 2.1. A wind turbine has a so-called cut-in speed which is the minimum wind speed the turbine needs for

generating power. At higher wind speed, typically at 12 - 17 m/s, the turbine reaches the limit of what its generator is capable of and it approaches the rated wind power. The rated power is the maximum power the turbine can generate. The wind speed corresponding to the rated power is referred to as rated wind speed. After this limit is reached, the wind turbine will not generate
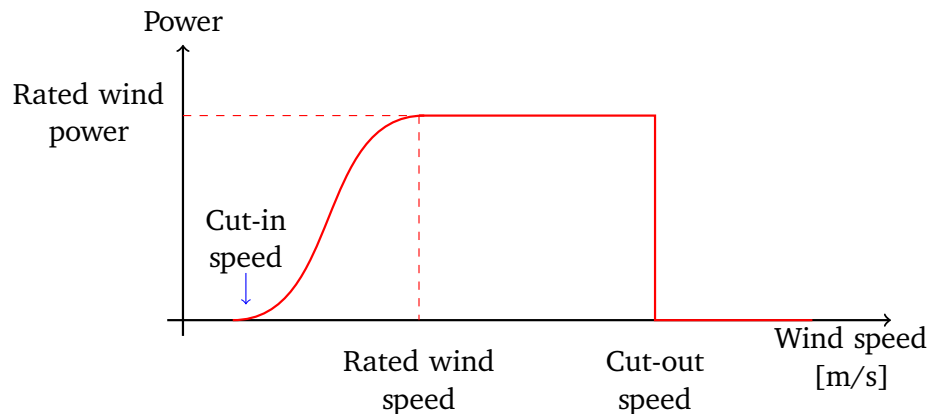
Figure 2.1: Illustration of a power curve. The sketch illustrates cut-in, cut-out speed and rated power.

more electricity even if the wind speed increases. At a certain wind speed, the turbine will pitch its rotor blades in order to stall the turbine to prevent the thrust force from the wind to damage the turbine.

2.6   Betz' limit

The Betz' limit derives a maximum power one can extract from a wind turbine. If one extracted 100% of the energy from a moving air parcel, the parcel would have lost all its momentum and its downstream velocity would be zero, preventing other air parcels to pass. When harvesting wind energy, the velocity of the air is reduced, and because of continuum, the cross sectional area of the air stream will increase as sketched in Fig. 2.2. The Betz' limit or Betz' law gives the maximum power an *ideal* wind turbine can harvest. The underlaying assumptions for the derivation of Betz' limit is

- The mass and momentum of the airstream is conserved.

- The rotor is an idealized rotor, meaning that it is infinitely thin, it has no hub, it has infinitely many blades where the airfoils has no drag. This rotor is referred to as an "actuator disk".
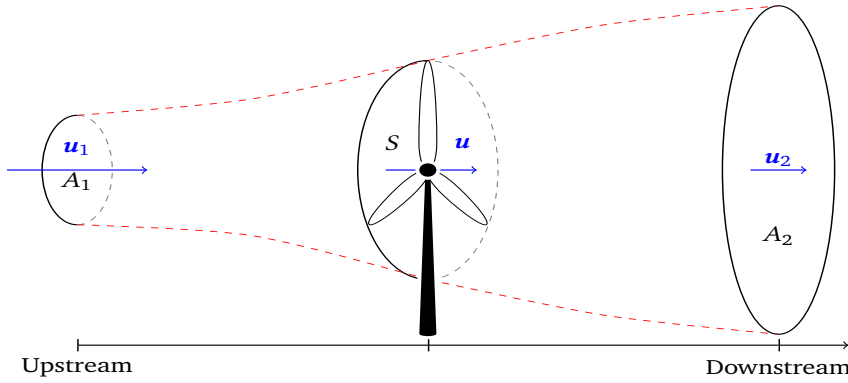
Figure 2.2: Sketch of the air stream upstream and downstream of a wind turbine.

- The flow into and out of the rotor is axial, as sketched in Fig. 2.2.

- The fluid is incompressible, homogeneous and the flow is steady with no heat transfer.

Defining the volume flow rate as the volume flowing through a cross section A per unit time as

$$\dot{V} = \int_A \boldsymbol{u}\mathrm{d}A = \boldsymbol{u}A, \tag{2.6.1}$$

where $\boldsymbol{u}$ is the horizontal average velocity the fluid has through the cross section. The mass flow rate is then related to the volume flow rate by

$$\dot{m} = \rho\dot{V} = \rho A\boldsymbol{u}. \tag{2.6.2}$$

By noting that the fluid's velocity at the turbine can be expressed as $\boldsymbol{u} = \Delta\boldsymbol{x}/\Delta t$ and that the volume of the fluid is $V = A\Delta\boldsymbol{x}$, the mass flow can also be formulated as

$$\dot{m} = \frac{\rho A\Delta\boldsymbol{x}}{\Delta t} = \frac{\rho V}{\Delta t} = \frac{m}{\Delta t}, \tag{2.6.3}$$

where the density ρ is mass divided by its volume. Because the flow is steady and the mass is conserved, the mass flow is constant through the turbine giving the relation

$$\rho A_1\boldsymbol{u}_1 = \rho S\boldsymbol{u} = \rho A_2\boldsymbol{u}_2, \tag{2.6.4}$$

where the subscript 1 denotes the upstream wind velocity and area of the fluid and subscript 2 denotes the downstream, as illustrated in Fig. 2.2.
Newton's 2nd law gives the force exerted on the wind by the rotor

$$\begin{aligned}
F &= m\frac{\Delta\boldsymbol{u}}{\Delta t} = \dot{m}(\boldsymbol{u}_1 - \boldsymbol{u}_2) \\
&= \rho S\boldsymbol{u}(\boldsymbol{u}_1 - \boldsymbol{u}_2),
\end{aligned} \tag{2.6.5}$$

where the two expressions for mass flow is inserted. The power corresponding to this force is $P = \Delta F x / \Delta t$. Because the flow is steady, the force is constant, and the power can be expressed as

$$P = F \frac{\Delta x}{\Delta t} = Fu = \rho S u^2 \cdot (u_1 - u_2). \tag{2.6.6}$$

The power can also be explained as work per time where the kinetic energy expresses the work

$$\begin{aligned} P &= \frac{\Delta E_k}{\Delta t} = \frac{1}{2} \frac{m}{\Delta t} u_1^2 - \frac{1}{2} \frac{m}{\Delta t} u_2^2 \\ &= \frac{1}{2} \rho S u (u_1^2 - u_2^2), \end{aligned} \tag{2.6.7}$$

The velocity through the cross section S can then be found by setting Eq. 2.6.6 equal to Eq. 2.6.7

$$\begin{aligned} \rho S u^2 \cdot (u_1 - u_2) &= \frac{1}{2} \rho S u (u_1^2 - u_2^2) \\ \implies u &= \frac{1}{2}(u_1 - u_2). \end{aligned} \tag{2.6.8}$$

Inserting the velocity through the turbine (Eq. 2.6.8) into Eq. 2.6.7 then gives the wind power at the turbine, namely

$$P = \frac{1}{4} \rho S u_1^3 \left(1 + \frac{u_2}{u_1} - \left(\frac{u_2}{u_1} \right)^2 - \left(\frac{u_2}{u_1} \right)^3 \right). \tag{2.6.9}$$

The maximum power can be found by finding the ideal ratio between the upstream and the downstream velocities. Substituting $a = u_2/u_1$ for easier notation. a is sometimes referred to as the *axial induction factor* [42]. The extremas of the power is found by

$$\begin{aligned} \frac{\partial P}{\partial a} &= \frac{\partial}{\partial a} \left(\frac{1}{4} \rho S u_1^3 (1 + a - a^2 - a^3) \right) \\ &= \frac{1}{4} \rho S u_1^3 \left(1 - 2a - 3a^2 \right) \\ &= 0. \end{aligned} \tag{2.6.10}$$

Solving this gives $a = \{-1, 1/3\}$. Because $P(-1) = 0$, the optimal ratio is $a = u_2/u_1 = 1/3$ and the optimal power is

$$\begin{aligned} P_{optimal} &= P(1/3) \\ &= \frac{1}{2} \cdot \frac{16}{27} \rho S u_1^3. \end{aligned} \tag{2.6.11}$$

The power coefficient is the ratio between the power one can get from the wind over the power potential. The power potential from a fluid at velocity $\boldsymbol{u}_1$ in a cylindrical shape with crossection S is $P_{potential} = 1/2\rho S\boldsymbol{u}_1^3$. The maximum power coefficient from an ideal wind turbine is therefore

$$
\begin{aligned}
C_{p,max} &= \frac{P_{optimal}}{P_{potential}} \\
&= \frac{\frac{1}{2} \cdot \frac{16}{27}\rho S\boldsymbol{u}_1^3}{\frac{1}{2}\rho S\boldsymbol{u}_1^3} \\
&= \frac{16}{27},
\end{aligned}
\tag{2.6.12}
$$

which is also known as Betz' coefficient or the Betz' limit [42]. This implies that an *ideal* turbine can harvest $16/27 \approx 59,3\,\%$ of the energy from the wind.

2.7 Turbulence

Typical scaling for the momentum equation can be expressed as U for the velocity, T time, length scale L, typical scale of the pressure deviation Φ, namely

$$
\underbrace{\frac{\partial \boldsymbol{v}}{\partial t}}_{U/T} + \underbrace{(\boldsymbol{v} \cdot \nabla)\boldsymbol{v}}_{U^2/L} = - \underbrace{\nabla\phi}_{\Phi/L} + \underbrace{\nu\nabla^2\boldsymbol{v}}_{\nu U/L^2}.
\tag{2.7.1}
$$

The second term on the left-hand side can be referred to as the advection term and the second term on the right-hand side can be referred to as the viscous term. The ratio of the advection term to the viscous term, $(U^2/L)/(\nu U/L^2) = UL/\nu$, is the Reynolds number, namely

$$
Re \equiv \frac{UL}{\nu}.
\tag{2.7.2}
$$

A low Reynolds number indicates that the fluid flow is laminar, and a high Reynolds number indicates that the flow is turbulent [12].

Turbulence is a large an complex topic in fluid mechanics and the full derivation and detailed explanation is not the scope of this thesis. Vallis [72] defined turbulence as:

> *Turbulence is high Reynolds number fluid flow, dominated by nonlinearity, containing both spatial and temporal disorder.*

Turbulence can be visualized as small irregular swirls of fluid. These swirls are often referred to as *eddies*. Turbulence can be divided into three main categories: buoyancy, shear production and dissipation [68].

The "strength" of the turbulence in a flow is represented by the *turbulent kinetic energy*, abbreviated TKE. A variable can be expressed by a base-state (also referred to as a mean-state) and a perturbed quantity. For kinetic energy this can be expressed

$$E_k = \overline{E_k} + E'_k, \tag{2.7.3}$$

where E'_k is the turbulent kinetic energy. For convenience I divide by the mass and define the turbulence energy per unit mass as

$$e \equiv \frac{E'_k}{m} = \frac{1}{2}\left(u'^2 + v'^2 + w'^2\right), \tag{2.7.4}$$

according to Launder and Spalding [38] and Jones and Launder [35]. The evolving TKE can be generated by buoyancy and mechanical eddies [68].

Buoyancy

The most important contribution of the buoyancy term is the temperature flux, where thermal advection makes hot air rise, leading to instability in the horizontal fluid layers. At large vertical temperature gradients, the temperature buoyancy can dominate evolution of TKE, leading to a large generation rate of turbulence close to the ground surface. The buoyancy term is obviously strongly influenced by diurnal variations and has a strong seasonal dependence. At stable conditions, an air parcel displaced to a higher altitude would experience a negative buoyancy due to the temperature drop in the parcel, and be displaced towards the starting point. Thus, the buoyancy term can also consume TKE and acts as a sink of the TKE evolution and stabilising the fluid flow.

Mechanical eddies

The mechanical eddies can be created from frictional drag, when wind shears develop as the air is flowing over the ground. The shear is a stress force, i.e. the force that produce a deformation in a body. When fluids are deflected by objects, their wakes will be created adjacent to the objects. This wakes are illustrated in Fig. 2.3 where one can see that the wake effect in the leeward side of the turbines.

The shear stress in the atmosphere is mainly due to pressure, Reynolds stress and viscous stress. The pressure stress originates from pressure gradients and acts on fluids at rest. Reynolds stress is a turbulent momentum flux and can be described by a fluid cube where some parts of the cube has a different velocity than the other parts of the cube. This could result is a variety of deformations of the cube. The Reynolds stress can originate from the surface roughness and

Figure 2.3: Illustration of wake effects in leeward side of wind turbines. The figure is borrowed from the National Oceanic and Atmospheric Administration (NOAA) [31]

the no-slip approximation, leading to frictional drag. The cartesian components of the Reynolds stress tensor is called *kinematic units* with the components $u'u'$, $u'v'$ and $u'w'$ [68].

The last contribution to the TKE evolution is viscous dissipation also referred to as viscous stress. The viscous stress arises from intermolecular forces when one portion of the fluid moves in another direction and/or at a different rate than the other portions of the fluid. The intermolecular forces are measured as viscosity. This term is only a sink, where the TKE is dissipated as the fluid are deformed due to the viscous effects. The viscous dissipation increases as the eddy size decreases.

/3

Methodology

3.1   Site and time

The Rieppi site is located east of the Lyngen alps in the norther part of Norway as marked by the red square in Fig. 3.1a. Figure 3.1b is the area inside the red square and depicts the topography of the surrounding landscape around the site. The main measurement mast is maked with a red dot. The coastline in Fig. 3.1b is marked with a black line. As shown in Fig. 3.1b, the site is approximately 550 meters above mean sea level (MSL) surrounded by mountainous terrain. The valley lies between mountains in the northeast and southwest that are up to 1400 meters above MSL.

The vegetation of the site is mainly heathland on barren ground. There are some birch trees in leeward sides. The trees rarely get any higher than a couple of meters. Based on an average during a period of 30 years (from 1961 to 1990), Skibotn in the NW end of the valley is one of the five places in Norway receiving least precipitation, only 300 mm annually [41].

Figure 3.2a marks the area of the potential wind park with orange and there are suggested locations for 26 wind turbines. Figure 3.2b shows the wind park site with a black boarder along with the compass directions at the site. The two red dots in Fig. 3.2b are the two measurement mast.

(a)

(b)
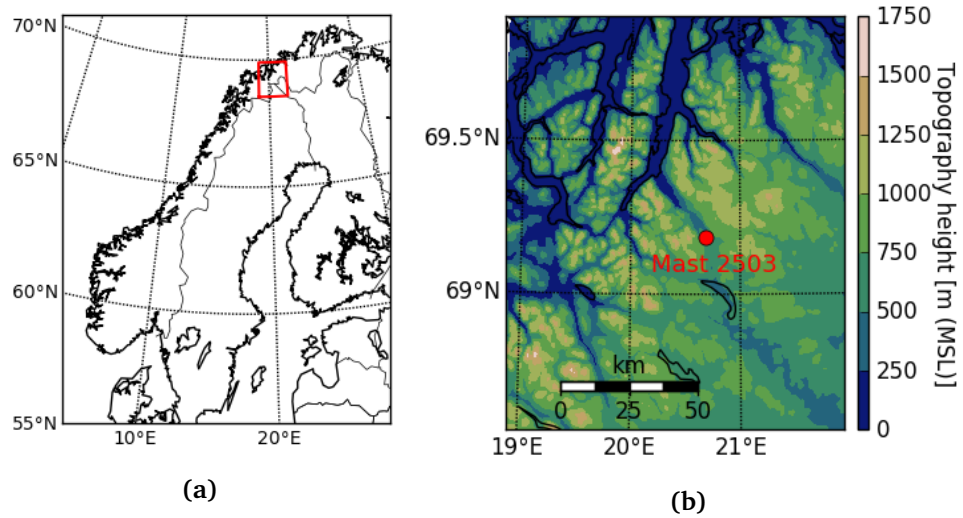
Figure 3.1: a: Overview of the site. b: The main measurement mast is marked with a
red dot along with the surrounding topography.

(a)

(b)
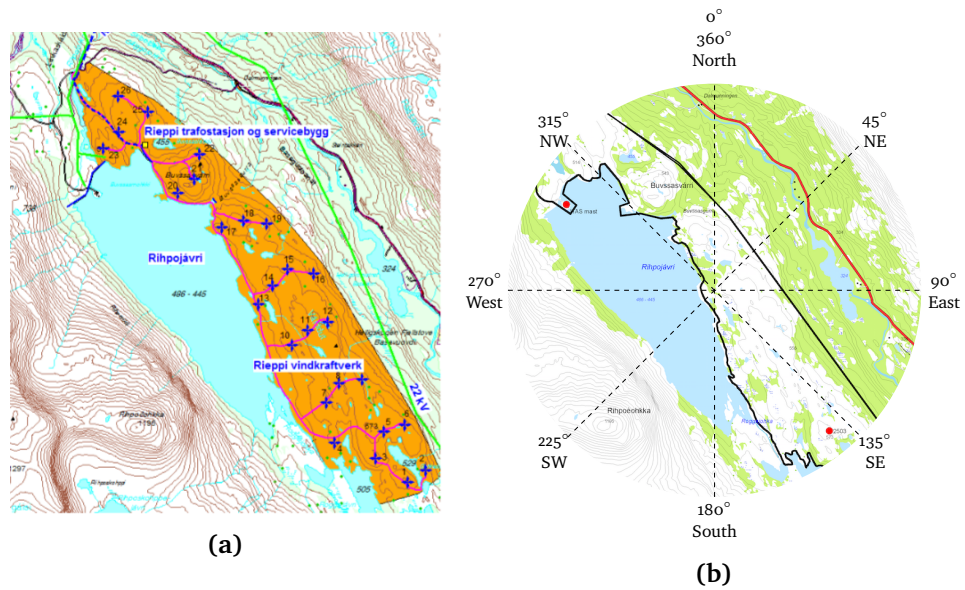
Figure 3.2: a: Overview of the wind park area. b: Directions at the wind park. The red
dots shows the location of the two measurement masts. The SE red dot
in (b) is "Mast 2503" which provides the main on-site measurements. The
NW red dot denotes the 10-meter mast referred to as WAS. Figure 3.2a
and Fig. 3.2b are retrieved from [71]. Higher resolution maps with english
notations were not available.

The study time is from January to December, 2014. The sampling interval of the

on-site observations are 10 minutes which captures rapid changes in direction, temperature and wind speed. The motivation for choosing measurements for a whole year is to capture monthly and seasonally variations.

A climatology based on on-site measurements from 2004 to 2013 is also computed for assessing the representativeness of the measurements for 2014.

3.2 Data sources

3.2.1 On-site measurements

The on-site measurements are from two masts at the Rieppi site, namely mast 2503 and mast WAS. The setup of the mast and data collection is done by Kjeller Vindteknikk and the data is distributed by Troms Kraft AS, who has ordered the data. The data available for this thesis is measurements for 2014 at mast 2503 and measurements for the period 2003 - 2014 at the WAS mast. The two masts are shown with red dots on Fig. 3.2b where WAS is the mast to northwest and 2503 is the mast to the southeast. Observations from these masts will be referred to as "on-site observations".

Mast 2503

Mast 2503 is located 567 meters above mean sea level (MSL) on a northwest oriented ridge at the location 20.6804 E, 69.1867 N. The mast is approximately 50 meters above ground level (a.g.l.) and measures temperature, wind speed and wind direction. Wind speed is measured by five cup anemometers at elevations 10.4 m, 30 m, 42.4 m and two at 49.1 m. Wind directions are measured by two sensors at 9.7 m and 42.1 m. Temperature is measured by one sensor at 2 meters a.g.l. The on-site observations used in this thesis are from mast 2503 with the exception of the climatology for the site, which is from the WAS mast.

Mast WAS

The northwest red dot in Fig. 3.2b marks the WAS mast. The mast is approximately 490 meters above MSL at 20.5799 E, 69.2233 N. This mast is 10 meters tall and measures temperature, wind speed and wind directions at 10 meters elevation. The WAS mast is located on a small peninsula in the Rihpojávri lake. As mentioned above, the WAS mast is the secondary mast used as a reference point to the 2503 mast to double-check measurements from 2503 and for mak-

ing the climatology for the area. This mast is used for the climatology because this is the only mast where Troms Kraft AS has provided measurements older than 2014.

3.2.2   ERA-Interim

The European Centre for Medium-Range Weather Forecasts (ECMWF) provides the reanalysis data set ERA-Interim of climatological data from January 1979 to present [17], [23].

Reanalysis data is obtained by assimilating historical and present observational data using a consistent assimilation scheme on all the data into a global weather prediction model. The observational data are collected by numerous instruments like satellite instruments, weather stations, ships, buoys etc. [24].

The temporal resolution of a large number of surface, atmospheric and oceanic parameters is 3 hours. Some meteorological estimates has a resolution of 6 hours [17]. The spatial resolution is given as approximately 80 km horizontally, and with 60 vertical levels, where the highest being 0.1 hPa [22]. ERA-Interim data provides four analysis per day, for 00, 06, 12 and 18 UTC [36].

3.2.3   The WRF model

The WRF model is used for simulation with ERA-Interim as input data. The comparisons between the on-site observations and the WRF simulations will determine whether or not the model could be used for reproducing temperature and the wind regimes at Rieppi. If the WRF data shows high consistency, they can corroborate the on-site measurements. A major advantage of using a numerical weather prediction model is the ability of evaluating fields of interest, like for example wind fields, turbulence, precipitation, land-use, solar irradiation etc. Model output can therefore provide information of the weather in the surroundings of Rieppi and not just the location where the measurement masts are located.

The temporal and spatial resolution of the output data from WRF is to some extent user-defined. A more detailed presentation of the WRF model and its functionality will be presented in Chapter 4.

3.3 Statistical methods

3.3.1 Fundamental statistics

The expectation value, or theoretical mean vector of a feature vector $x = [x_1, x_2, ..., x_n]^\top$ can be expressed

$$\boldsymbol{\mu} = E[\boldsymbol{x}] = \sum_{i=1}^{n} x_i p_i, \tag{3.3.1}$$

where p_i is the probability of the i-th event. n is the total number of features. The estimated mean from a sample is denoted $\overline{x}$.

The theoretical variance of x can be expressed

$$\sigma^2 = Var[\boldsymbol{x}] = E\left[(\boldsymbol{x} - \boldsymbol{\mu})^2\right] \tag{3.3.2}$$

$$= \sum_{i=1}^{N} (\boldsymbol{x}_i - \boldsymbol{\mu})^2 p_i. \tag{3.3.3}$$

The standard deviation is the square root of the variance. The sample variance is denoted s^2 and the sample standard deviation s.

The general n-dimensional covariance matrix has the form

$$\Sigma = \begin{bmatrix} \sigma_1^2 & \sigma_{12} & \cdots & \sigma_{1n} \\ \sigma_{21} & \sigma_2^2 & \cdots & \sigma_{2n} \\ \vdots & \vdots & \ddots & \vdots \\ \sigma_{n1} & \sigma_{n2} & \cdots & \sigma_n^2 \end{bmatrix}, \tag{3.3.4}$$

where the matrix elements can be expressed

$$\sigma_{ij} = E\left[(x_i - \mu_i)(x_j - \mu_j)\right]. \tag{3.3.5}$$

Covariance normalized to unity is called correlation coefficient and can be expressed as

$$\rho = \frac{\Sigma_{xy}}{\sigma_x \sigma_y}, \tag{3.3.6}$$

according to Walpole et al. [74].

Analogues to the variance, the Root Mean Squared Error RMSE is a measure of the average distance between two data series X and Y and is calculated by

$$\text{RMSE} = \sqrt{\frac{1}{n} \sum_{i=1}^{n} (X_i - Y_i)^2}, \tag{3.3.7}$$

where n is the total number of samples. If the factor two is omitted from Eq. 3.3.7, one can evaluate the data *tendency*, namely the Bias

$$\text{Bias} = \frac{1}{n} \sum_{i=1}^{n} \left(X_i - Y_i \right). \tag{3.3.8}$$

To exemplify the Bias, one can denote X as the real, i.e. the observed values and Y as the simulation values. If the Bias is positive, it means that the simulated values tend to overestimate the real data and if the Bias is negative, it indicates that the simulated values tend to underestimate the real values [11].

The standard deviation, RMSE and the Bias together are good indicators for the error between two data sets. If a simulation shows high RMSE and/or Bias, but low standard deviation, it is a strong indicator for systematic error(s), but it yields that the physics is correct. Moreover, if the standard deviation is high, it indicates that the error is random and in this case, the physics might be incorrect, even if the RMSE and/or Bias is low.

3.3.2   Directional statistics

Because the ordinary mean of the two wind directions 5 and 355 degrees would erroneous give 180 degrees and not 0 or 360 degrees, it is easy to see that the ordinary linear statistics must be modified to be valid for directional statistics. Firstly, the mean direction from a sample of n directions can be expressed as

$$\bar{r} = \frac{1}{n} \sum_{i=1}^{n} r_i, \qquad \text{for} \qquad i = 1, 2, ..., n, \tag{3.3.9}$$

where $r_i = (r \cos \alpha_i, r \sin \alpha_i)$ is the polar representation of the cartesian components. α is the angle in radians. According to Jammalamadaka and Sengupta [33], the resultant vector can be defined as the sum of the n unit vectors, namely

$$\boldsymbol{R} = \left(\frac{1}{n} \sum_{i=1}^{n} \cos \alpha_i, \frac{1}{n} \sum_{i=1}^{n} \sin \alpha_i \right) = (C, S), \tag{3.3.10}$$

where C and S are used for easier notation. The length of the resultant vector $R = \|\boldsymbol{R}\|_2$ is a measure of the spread of the data [43]. $\| \cdot \|_2$ denotes the 2-norm. If the directions $\alpha_1, ..., \alpha_n$ are tightly clustered, R approaches 1, and vice versa, if the angles are widely dispersed, R will approach zero. The circular variance can be expressed as

$$\sigma^2 = 2(1 - R). \tag{3.3.11}$$

This is proved in Appendix D: *Derivation of circular sample variance.*

For computing the directional correlation coefficient, I start by noting that a perturbation from a variable X can be expressed $x_i = X_i - \mu_x$. Using this and the above expressions for μ and σ, Eq. 3.3.6 can be rewritten to

$$\rho_{xy} = \frac{\sum_{i=1}^{n} \left[(x_i - \mu_x)(y_i - \mu_y) \right]}{\sqrt{\sum_{i=1}^{n} x_i^2} \sqrt{\sum_{i=1}^{n} y_i^2}}$$

$$= \frac{\sum_{i=1}^{n} x_i y_i}{\sqrt{\sum_{i=1}^{n} x_i^2} \sqrt{\sum_{i=1}^{n} y_i^2}}.$$

(3.3.12)

Following the procedure shown by Gniazdowski [28], the numerator is only a dot product between x and y and that the denominator is the product of the lengths of x and y. The correlation coefficient can then be rewritten as

$$\rho_{xy} = \frac{x \cdot y}{\|x\|_2 \cdot \|y\|_2}$$

(3.3.13)

$$= \cos(x, y),$$

(3.3.14)

It is important to notice that a high correlation coefficient from Eq. 3.3.13 is not necessarily the same as claiming that the directions of x and y are the same, but that x and y has equal deviation from the mean.

A good way of representing both wind speed and wind direction is a so-called *wind rose*. A wind rose is a polar representation of a histogram visualizing both direction and the amount of data in each direction. The wind rose is divided into bins where the length of each bin represents the occurrence of wind speeds in that bin. Figure 3.3 shows two examples of wind roses where the left is used for indicating wind speed and direction and the right is used for comparing wind directions from four different sources. The right wind rose does not include wind speed information.

Note that the wind rose on the left gives the occurrence of each bin in percent and the wind rose on the right gives occurrence as a ratio.

3.3.3 Wind speed distribution

A commonly used continuous probability distribution of wind speeds is the Weibull distribution [16] and [58]. The Weibull distribution can be used for determining the theoretical wind speed distribution, the mean wind velocity and the variance. The Weibull probability density function is given by

$$f(u; a, b) = \frac{b}{a} \left(\frac{u}{a} \right)^{(b-1)} \exp\left(-\left(\frac{u}{a} \right)^{b} \right), \qquad \text{for} \qquad u \geq 0, \qquad (3.3.15)$$
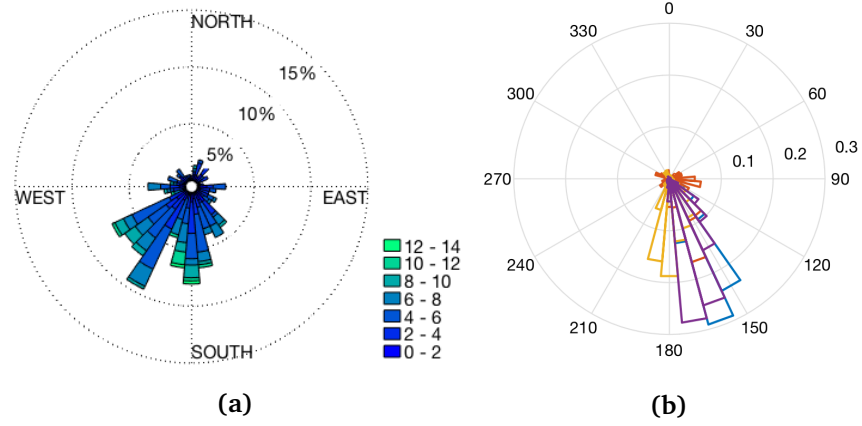
Figure 3.3: Examples of wind roses. The colors in the wind rose in (a) indicates the wind speeds in m/s. The colors in (b) indicates bins from different measurements.

where the parameters a and b are the scale and shape parameter respectively [16]. At certain values for a and b, the Weibull distribution has the same shape as other distributions like the Gaussian, exponential and the Rayleigh distribution. This is plotted in Fig. 3.4. A correct procedure for calculating a and b is therefore crucial.

The estimated mean and variance of the Weibull distribution is

$$\hat{\mu} = E[\boldsymbol{u}] = a\Gamma\left(1 + \frac{1}{b}\right) \tag{3.3.16}$$

$$\hat{\sigma}^2 = Var[\boldsymbol{u}] = a^2\left[\Gamma\left(1 + \frac{2}{b}\right) - \Gamma^2\left(1 + \frac{1}{b}\right)\right] \tag{3.3.17}$$

respectively. Γ is the gamma function defined by

$$\Gamma(k) = \int_0^\infty u^{k-1}\exp(-u)\mathrm{d}u, \qquad \text{for} \qquad k > 0. \tag{3.3.18}$$

according to [74].

There are different methods for calculating scale and shape parameters in the Weibull distribution, e.g. the maximum likelihood method, the proposed maximum likelihood method or the graphical method [58]. Seguro and Lambert suggests that the maximum likelihood method may be the best suitable.

The maximum likelihood method for parameters b and a can be expressed

by

$$b = \left(\frac{\sum_{i=1}^{N} u_i^b \log(u_i)}{\sum_{i=1}^{N} u_i^b} - \frac{\sum_{i=1}^{N} \log(u_i)}{N} \right)^{-1} \tag{3.3.19}$$

$$a = \left(\frac{1}{N} \sum_{i=1}^{N} u_i^b \right)^{1/b}, \tag{3.3.20}$$

where N is the number of (nonzero) wind speed data points and $\boldsymbol{u}_i$ is the wind speed in timestep i. log denotes the natural logarithm. Because Equation 3.3.19 is an implicit method, it must be solved by iteration and a convergence criterion has to be chosen. Equation 3.3.20 can subsequently be solved explicitly.
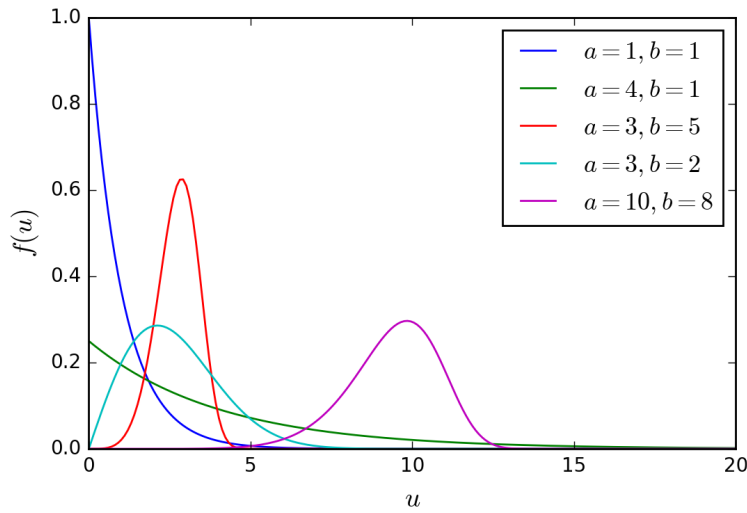
Figure 3.4: Weibull example of different parameters of a and b in Eq. 3.3.15

For investigating whether a dataset fits the Weibull distribution, one can plot the normalized histogram of the dataset. A histogram is a graphical representation of the distribution of the data which shows the number of measurements at discretized levels. A normalized histogram is the number of measurements divided by the total number of elements. The normalized histogram is therefore a representation of the probability of each value and can be expressed

$$p_r(u_k) = \frac{n_k}{N}, \qquad \text{for} \qquad k = 0, 1, 2, ..., L - 1, \tag{3.3.21}$$

where p_r is the probability of the occurrence of the wind speed u_k. n_k is the number of measurements at the value u_k. L is the total number of values, i.e. the number of unique u_k. N is the total number of data points.

4

The WRF model

The development of the WRF model began in the late 1990's and after the birth of the first release in November 2000, the WRF model has been used in a wide range of meteorological applications for the research and operational forecasts. Some of the principal participators in the WRF project has been the Mesoscale Meteorology Division of the National Centre for Atmospheric Research (NCAR/MMM), the National Centers for Environmental Prediction (NOAA/NCEP), the Forecast Systems Laboratory (NOAA/FSL), the University of Oklahoma Center for the Analysis and Prediction of Storms (CAPS), and the U.S. Air Force Weather Agency (AFWA) [49].

The WRF model consists of two large blocks; WPS and WRF. The WPS are an abbreviation for WRF preprocessing, and it contains three programs that assimilates and/or produces terretrial and meteorological boundary and initial conditions. The WRF part further assimilates the input data from the WPS step and runs the actual simulation [50].

4.1   The WRF model framework

The Weather Research and Forecasting (WRF) model is a simulation tool for numerical weather prediction used in operational applications and in research. The model is by many considered as a state-of-the-art model [27]; [11]; [37]; [64] for predicting mesoscale weather.

The WRF model is open source and because of this availability many researchers, Universities and other agencies has contributed to different modifications like physical parametrization schemes, numerics, and the informatics. As a result of this large-scale collaboration, the model is versatile with a large spectre of physical and numerical options and it parallelize well on many processors. The output file from a typical simulation run consists of more than 150 variables.

The WRF version used in this thesis is the WRF V3.7.1.

Because WRF is a model that demands large computational resources and computer memory for running high resolution simulations from real input data, the simulations were run on the supercomputer *Stallo* at the University of Tromsø - The arctic university of Norway. The use of Stallo has been a necessity for this study as the total amount of memory required for the simulations exceeds 25 TB and without the ability of running the model on many parallel processors simultaneously, the simulations would not have finished in time for the submission of this thesis.

The program flow of one simulation of the WRF model involves several steps. The main components in the program flow is sketched in Fig. 4.1. The explanation is based on the description of the WRF model by Skamarock et al. [63], Skamarock et al. [64] and the WRF-ARW User's guide [75].

4.1.1   Input to preprocessing

The model needs two types of input; terrestrial data and meteorological data. Other than the topography, the terrestrial data can contain vegetation, albedo, lake depths and soil types and other parameters. The user has to find the dataset best suited with regard to number of parameters and resolution. In this thesis, the input data was downloaded from the National Centre for Atmospheric Research (NCAR) [65].

The initial and boundary meteorological conditions used in this study are retrieved from ERA-Interim. As emphasised in Chapter 3, section 3.2.2, the temporal resolution is 6 hours and the spatial is approximately 80 km. The meteorological input data has 60 vertical levels.

The meteorological input could also be downloaded from other sources like on-site measurements, satellites or from a previous WRF simulations.

4.1.2   Preprocessing

The WRF preprocessing system is abbreviated WPS and the preprocessing prepares the model domain and sets the initial and boundary values. The preprocessing is done by the three programs *geogrid*, *ungrib* and *metgrid*.

Namelist (WPS)

The namelist in the WPS step sets which WRF core that should be used (ARW or NMM), the simulation date and time, information on the input data and the size of the simulation domains. The number of domains is also set in the *namelist.wps* file. An example of a namelist file can be examined in Appendix E: *Namelists*.

The namelist interact with all the three programs in the WPS framework, as sketched in Fig. 4.1. Each of the WPS programs reads parameters such as simulation start and end time, time steps, number of domains, longitude and latitude etc. from the namelist file. Output from WPS is used as input to the actual simulation in WRF.

Geogrid

The geographical data is interpolating using the geogrid program. The geogrid program reads the entries in the namelist file defining the simulation domain(s). The geogrid program creates a static landscape model in the simulation domain, containing for example terrain height, monthly vegetation, albedo (also maximum and minimum snow albedo), soil categories, annual mean deep soil temperature etc. The geogrid program is usually ran once as the landscape does not change during one model run.

Ungrib

The initial meteorological data are GRIB-formatted files. GRIB is an abbreviation Gridded Binary data and is a meteorological format standard set by the World Meteorological Organisation (WMO) [52]. The GRIB files contains time-varying meteorological fields. The meteorological fields are downloaded in the step *input to preprocessing*. The GRIB files are typically from other weather models or observational data. The GRIB files are packed for efficient storing and thus it has to be "unpacked" or "degribbed" before it can be used in the WRF model.

Metgrid

The output from the ungrib and geogrid program is the input to the metgrid program. The metgrid program horizontally interpolates the meteorological data from the ungrib program onto the simulation domain. The metgrid program merges the geographical input data and the meteorological input data for initialize the simulation domain. Because the metgrid program uses the output from the time-dependent ungrib program, the metgrid is also time-dependent.

4.1.3   WRF

Namelist (WRF)

Similar to the preprocessing step, the namelist in the WRF step is defining the simulation parameters. The namelist in the WRF step is much more comprehensive than the preprocessing. In this file, all parameters and physical options must be specified. This includes for example simulation time, domain options, physics options, dynamics and boundary conditions. These options will be discussed in section 4.2.

Real

The name "Real" for the program is chosen when real data are used. In contrast, one can also replace the "Real" program by one called "Ideal". The Ideal program is used when an initial condition is constructed, instead of observational data.

The output from metgrid is horizontally interpolated meteorological fields onto a terrestrial simulation domain. The real program vertically interpolates the meteorological fields to the model grid. The output from Real is the fully interpolated 4-dimensional simulation domain. It is 4-D because of the time and space-dependence of the meteorological fields.

WRF

The fully interpolated 4-D simulation domain from the Real program is the input to the WRF model run. All steps prior to the WRF step are just initialization and setting boundary values. In this step the actual simulation is executed for the whole simulation time.

4.1.4 Postprocessing

The output file from WRF is NetCDF files containing the simulation variables. NetCDF is an abbreviation of Network Common Data Form and is a platform-independent self-describing library for scientific data. The output file of a simulation contains much information with over 150 variables. The extraction and analysis of the output data was done in Matlab, Python and NCL.

4.2 Parametrizations and experimental setup

Much of this section is from NCAR's technical note on the WRF-ARW Version 3 [64]. The different parametrization schemes will not be discussed in detail. Nor will they be mathematically explained or derived as this is not the aim of this thesis.

4.2.1 Dynamic solvers

There are two dynamical solvers within the WRF software framework, namely the Advanced Research WRF (ARW) and the Non-hydrostatic Mesoscale Model (NMM). The dynamic solver is the key component of the modeling system. The ARW solver is primarily developed at NCAR, and the NMM is primarily developed at the National Centers for Environmental Prediction (NCEP).

Bernardet et al. [4] aimed at determining the inter-core differences between the ARW and the NMM cores. They concluded that with their setup, there were no statistically significant difference between the cores.

The physics packages are largely shared by both ARW and NMM, but there are some schemes that are only compatible with either the ARW or the NMM solver.

In this thesis, the ARW is chosen. The main reasons for this choice is that it allows two-way nesting and a flexible ratio of the domains, meaning that the ratio between the domains can be chosen freely [64].

4.2.2 Domains and nesting

The meteorological input data described in subsection 4.1.1 serves as initial and boundary conditions for the simulation. When running simulations in the WRF model, the user has to specify the number of domains. This is specified in
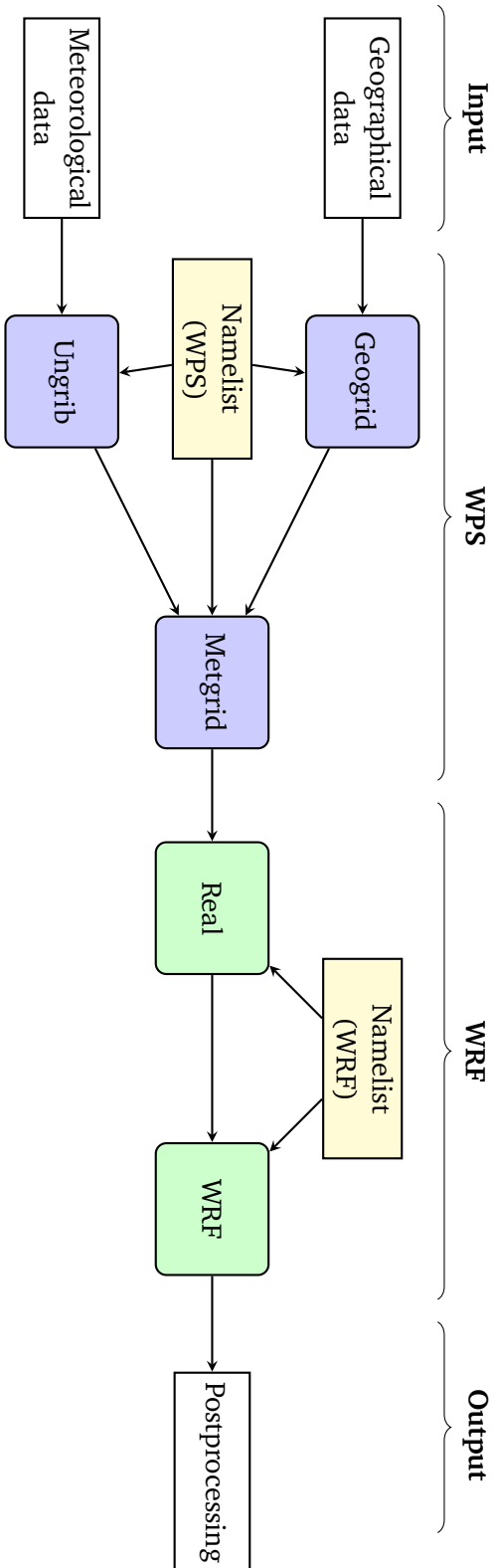
Figure 4.1: Flowchart of the different components in the WRF model. The white boxes are the input and output and is not a part of the model.

the WPS namelist. The domains are horizontally nested, meaning that they are similar objects of graduated sizes, so that the smaller domains fit into the larger. The largest domain is referred to as the parent domain, denoted D01. In this thesis, the most used configuration is three domains. Figure 4.2a show three domains, where the parent domain is the frame of the figure, and domain D02 and D03 are the nested domains. All the three domains has the center point at the Rieppi site marked with a red dot. The innermost domain in Fig. 4.2a has the highest resolution and the resolution decreases with domain 2 and 1.

Nesting options

There are two grid nesting options; 1-way nesting and 2-way nesting and the nests themselves can be arranged differently. Both 1-way and 2-way nesting is a downscaling from the largest, coarsest domain to the finer domains. In this process, the parent grid is simulated with the meteorological input described in subsection 4.1.1. The simulation output from the parent domain is then the initial and lateral boundary condition for the finer grid domain. After getting the input from the parent grid, the finer grid is simulated. This procedure continues to the innermost, highest resolution domain is simulated.

In 1-way nesting this is the only information exchange between the domains, hence the name 1-way nesting. In 2-way nesting the output from the finer grid is fed back to the coarser grid where the fine grid solution replaces the coarser grid's at the overlapping grid points inside the finer grid.

Different nest configurations are sketched in Fig. 4.2b where different domains has different colors. Figure (b.1) is an example of so-called *telescoping* domains. The green domain is the parent domain for the blue domain. The blue domain acts as parent domain for the red domain, and so forth. This means that when telescoping domains are used, the finer domain gets its initial and boundary values from the larger, enclosing domain.

Figure 4.2b.2 is also allowed as long as the domains does not overlap [64], hence the configurations sketched in (b.3) and (b.4) are *not* allowed. The blue and red domain in (b.2) are referred to as *siblings*. Each sibling domain can have any telescoped depth, i.e. any number of finer nests inside as long as they does not overlap. Configuration (b.2) is useful when more than one site in the simulation domain is of interest, but it is too resource demanding to run fine grid simulations for the whole area.

The domain sizes are determined by the domain grid spacing, where the grid spacing is user-defined. As noted in Chapter 1, the resolution ranges from global to subgrid scale, but with emphasis on horizontal grid spacings
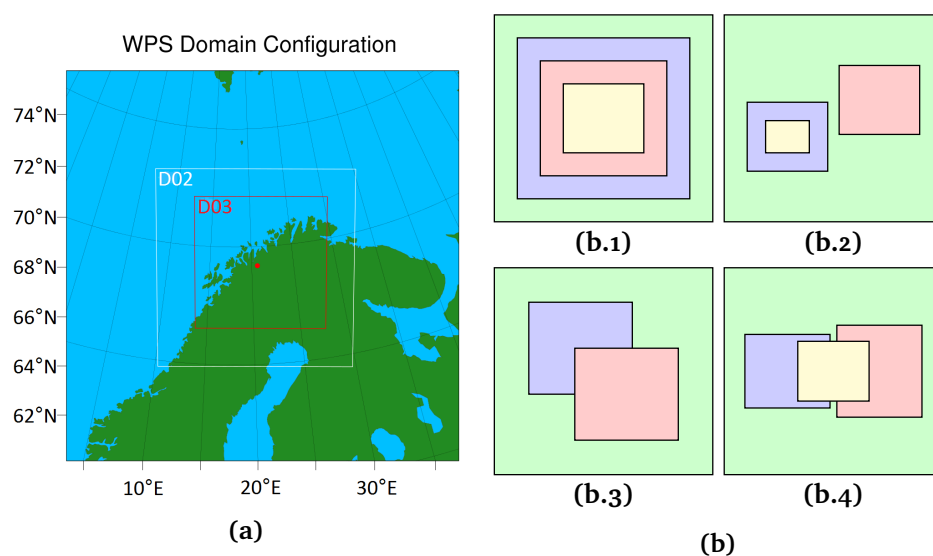
Figure 4.2: Figure (a) showing the setup of three telescoping domains, all centred at the Rieppi site (red dot). Figure (b) shows different nest configurations. (b.3) and (b.4) are not allowed.

ranging from 1 - 100 km according to Michalakes et al. [49]. At small scales though, one has to carefully consider the integration time step, terrestrial resolution and other factors that can lead to an unstable simulation. Also, some parametrization schemes perform better at subgrid-scale simulations than other [60]. A consideration of a more practical nature is the computation efficiency, which increases as the resolution decreases.

In this thesis, the most used nest configuration is three telescoping domains with the horizontal grid spacings

- D01: dx = 18000 m, dy = 18000 m

- D02: dx = 6000 m, dy = 6000 m

- D03: dx = 2000 m, dy = 2000 m.

The reason for this choice is a trade-off between computation cost and resolution.

Grid spacing of dx = 1000 m, dy 1000 m and dx = 500 m, dy = 500 m was also tested. At grid-spacing of 1 km, the model sometimes became unstable, and at 500 m grid-spacing it crashed. The reason for the crash is not known.

For computational efficiency, 1-way nesting was chosen from the parent domain,

but 2-way nesting was chosen on domain 2 and domain 3.

4.2.3 Map projections

The ARW solver supports four map projections; the Lambert conformal, polar stereographic, Mercator and latitude-longitude projections [64]. The Lambert conformal, polar stereographic and Mercator projections are all isotropic, meaning that the relation $\Delta x/\Delta y|_{earth}$ is constant everywhere on the sphere. As a rule of thumb, the polar stereographic projection is best suited for high latitudes, the Lambert conformal projection is well-suited for mid-latitude domains and the Mercator projection should be used for low latitudes [76]. The latitude-longitude projection is required for global WRF simulations.

Because the Rieppi site is at the latitude 69 $^\circ$ N, the polar stereographic map projection is used. If any of the other projections were used, there would be larger distortion in the distances of the projected maps.

4.2.4 Numerics

Integration scheme

The time-integration schemes available in the WRF model is either 2nd or 3rd order Runge-Kutta (RK2 or RK3 respectively). The RK3 is the recommended integration scheme [53]. Sauer [57] argues that higher order Runge-Kutta schemes generally has a faster convergence than lower-order Runge-Kutta schemes like RK1 or RK2. Runge-Kutta schemes are explained and in Appendix F: *Numerical integration*.

The transport of a geophysical quantity by the velocity field is often referred to as advection [21].

Time step constraint

When using the Runge-Kutta method for time-integration, the time step Δt must be determined. The time step is user-defined and the choice of the time step is important for the stability of the integration. A large time step is computational efficient, but a too large time steps can lead to a unstable solution. The Courant-Fredrichs-Lewy (CFL) condition is a time step constraint condition for convergence of an ordinary differential equation. The CFL condition is necessary for stability but the condition alone does not *guarantee* stability [21].

For the case of determining the time step constraint for a wind simulation where the horizontal wind speed is u and the simulation domain has a spatial discrete grid spacing of Δx, the CFL condition can be expressed as

$$0 \leq \frac{u \Delta t}{\Delta x} \leq 1. \tag{4.2.1}$$

The Courant number in one dimension is defined as

$$Cr = \frac{u \Delta t}{\Delta x} \tag{4.2.2}$$

according to Skamarock et al. [64].

The maximum Courant numbers for one-dimensional linear advection is obtained from Wicker and Skamarock [78] and tabulated below. The extension in two and three dimensions is done by multiplying the time step by a factor $1/\sqrt{2}$ and $1/\sqrt{3}$ respectively [78].

Table 4.1: Maximum Courant numbers for 1-D linear advection. For 3-D the Courant numbers must be multiplied with a factor $1/\sqrt{3}$.

Time scheme	Spatial order			
	3rd	4th	5th	6th
Leapfrog	*Unstable*	0.72	*Unstable*	0.62
RK2	0.88	*Unstable*	0.30	*Unstable*
RK3	1.61	1.26	1.42	1.08

According to Wicker and Skamarock [78], the maximum time step for the RK3 integration in 3-D applications, the time step should satisfy

$$\Delta t_{max} < \frac{Cr}{\sqrt{3}} \cdot \frac{\Delta x}{u_{max}}, \tag{4.2.3}$$

here Cr denotes the Courant number obtained from Tab. 4.1, Δx is the spatial grid spacing of the larges simulation domain and u_{max} is an estimate of the maximum expected horizontal wind velocity throughout the simulation. To ensure a buffer, it is advised to chose Δt_{max} 25 % smaller than calculated by (4.2.3). When estimating the highest wind speed u_{max} one should consider the wind speeds throughout the vertical simulation domain. Hence, $u_{max} \approx 100$ m/s is not unrealistic in many cases.

For the ARW core of WRF, it is advised that the maximum time step should be approximately 6 times the grid distance of the largest domain in meters [64].

In this thesis, the most used grid spacing of the largest simulation domain is 18000 meters. The 5th order advection scheme is chosen on the basis that

it enables a larger time step than the 6th order advection scheme. With a maximum wind velocity of 100 m/s, 5th order advection scheme, Eq. 4.2.3 gives that the time step with a buffer should be smaller than 111 seconds. From the rule of thumb mentioned above the maximum time step is 108 seconds. The time step was chosen to 90 seconds for most simulations. At certain simulations, the model has crashed and the procedure to fix this has been to reduce the time step, which normally works.

Throughout the simulation, it is likely that the maximum stable time step is larger than the fixed time step limited by (4.2.3). The ARW has an option referred to as *Adaptive time step*. The adaptively-chosen time step is usually larger than the fixed time step tends to be, and for this reason the integration is faster. It is based on the wind fields that is instantaneously evolving in the simulation. The adaptive time step is an option that is only available for the ARW core [53].

Grid nudging

It is not unusual that the WRF model diverges in long simulations. An option for long time simulations is to use a *nudging* technique, or so-called *Newtonian relaxation*. Grid nudging is a component of the WRF model's four dimensional data assimilation system and the technique is that the atmospheric model is *nudged* or *relaxed* toward the time- and space-interpolated analyses and/or observations over the integration period [64], [11].

4.2.5 Terrain; the link between WRF and actual terrain

I will start this subsection by some spherical observations. Firstly, a small excursion along the surface of sphere can be expressed

$$(\delta \boldsymbol{x}, \delta \boldsymbol{y}, \boldsymbol{z}) = (r\delta\lambda \cos\vartheta_o, r\delta\vartheta, z), \qquad (4.2.4)$$

where r is the radius of the sphere, λ is the longitude, and ϑ is the latitude. The subscript o denotes the observational point. The excursion was done at constant altitude.

The output variables from the WRF simulations are discrete data points and these grid points do generally not coincide with the actual longitude-latitude grid. Analogues to the geometry above, the distance from mast 2503 to all WRF grid points from a simulation can be expressed using the Pythagorean

trigonometry

$$d(i,j) = \left(r^2 \cos^2\left(\frac{\vartheta_o + \vartheta(i,j)}{2} \right)(\lambda_o - \lambda(i,j))^2 + r^2(\vartheta_o - \vartheta(i,j))^2 \right)^{1/2}. \quad (4.2.5)$$

Here r is the radius of the Earth, the Rieppi site is at (λ_o, ϑ_o) and $(\lambda(i,j), \vartheta(i,j))$ denotes the WRF grid points. The best candidate for representing the Rieppi site is therefore WRF grid point with the smallest distance. The unit of Eq. 4.2.5 is meter.

A pseudo-code for extracting an example-variable at the grid point closest to the Rieppi site calculated using Eq. 4.2.5 is given as a pseudo-code below.

```
% Read variable from WRF output file
variable = ncread('path to WRF output file', 'variable name');

% Longitude and latitude of the Rieppi site
R_lon = 20.6804;
R_lat = 69.1867;

% Find the distance to all grid points
for longitudes && latitudes in variable
   d(i,j) = ...
end

% Find the minimum distance to the Rieppi site
[min_lon, min_lat] = find(minimum d(i,j));

save('Save variable to file')
```

4.2.6   Vertical coordinates

The eta vertical coordinate was first defined by Mesinger [45] and the motivation was to remove or minimize the errors that occurred when computing the diffusion, advection or pressure gradient force along steep slopes [6]. The main idea is that the bottom vertical coordinates is terrain-following for avoiding problems regarding the boundary condition at the ground surface [46]. By using eta coordinates, the ground surface is the first eta coordinate. The eta coordinate is pressure based and normalized. The eta coordinates in the WRF model is given in [64] as

$$\eta = \frac{p_h - p_{ht}}{\mu_d}, \quad (4.2.6)$$

where $\mu_d = p_{hs} - p_{ht}$. p_h is hydrostatic component of the pressure. p_{hs} and p_{ht} is pressure along the surface and the top boundary respectively. Eta coordinates are sketched in Fig. 4.3.
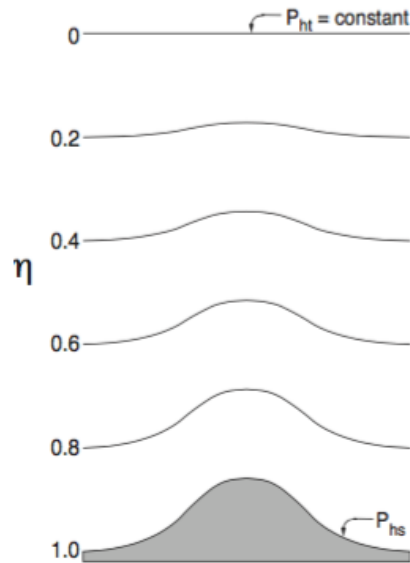
Figure 4.3: Illustration of the height coordinates in the WRF model.Image from Skamarock et al. [64].

The vertical distribution of the coordinates have a exponential shape as depicted in Fig. 4.4, allowing higher resolution nearer the ground surface to accommodate the small-scale changes near the surface in the boundary layer [14].

The vertical coordinates are based on the definition of geopotential, discussed in Chapter 2, Eq. 2.4.4. WRF expresses the geopotential as a base-state plus a perturbed value, namely $\Phi = \overline{\Phi} + \Phi'$, and thus, the geometric height can be expressed as

$$z = \frac{\overline{\Phi} + \Phi'}{g_0}, \tag{4.2.7}$$

where g_0 is the acceleration due to gravity. It is important to notice that the WRF model gives the geometrical height of the geopotential relative to the mean sea level, not to the ground surface.

4.2.7 Microphysics schemes

The microphysics parametrizations handles water vapour, cloud and precipitation processes. The number of variables, ice-phase, mixed-phase processes and the computational cost must be considered when assessing the suitable schemes. As a rule of thumb mixed-phase schemes should be used at grid sizes

(a)

(b)
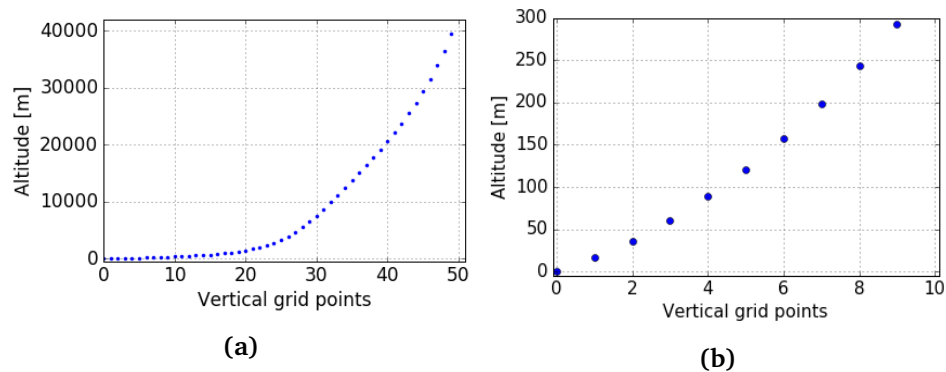
Figure 4.4: a: Approximation of the geometrical height of the vertical distribution of the grid points in the WRF model. b: Height distribution of the 10 grid points closest to the ground surface.

less than 10 km, especially if the simulation domain where there are much convection or icing. For coarser simulation domains the mixed-phase schemes should not be used because of the computational expenses [64].

In this thesis the WRF Single-Moment 5-class (WSM5) scheme is used. The rationale for this is that the grid sizes for the parent domain is more coarse than 10 km, and thus a mixed-phase microphysics scheme is not used. The WSM5 has not the mixed-phase scheme and it is referred to as 5-class because it predicts vapour, rain, snow, cloud ice and cloud water. The WSM5 scheme is efficient at intermediate grid sizes, i.e. approximately 1 km to 100 km.

4.2.8 Cumulus parametrization

The cumulus parametrization handles the sub-grid-scale effects of convective and/or shallow clouds. These schemes are only valid for grid sizes larger than 10 km because of the spatial resolution needed to release latent heat from the fluid columns at the WRF grids.

In this thesis the Betts-Miller-Janic scheme is used.

4.2.9 Radiation schemes

These schemes handles the atmospheric heating due to direct and diffuse radiation from the Sun and radiation from the ground heating. There are two types of radiation; longwave and shortwave. Shortwave radiation includes radiation with wavelengths in or close to the visible spectre. The only source

of shortwave radiation is the Sun. The shortwave radiation processes include absorption, reflection and scattering of the molecules in the atmosphere. Long wave radiation includes thermal and infrared radiation absorbed or emitted by the gasses in the atmosphere.

In this thesis, the New Goddard shortwave scheme [13] is used for both the shortwave and the longwave radiation schemes.

4.2.10   Surface layer schemes

To calculate the physical interactions between the surface and the atmosphere different parametrization schemes are used. The surface layer (SL) schemes calculate friction velocity at the model surface and the exchange coefficients needed to calculate the surface heat, surface stress and moisture fluxes. The surface layer provides stability-dependent information about the land-surface model above.

The Eta scheme is chosen for this study.

4.2.11   Land-surface model

The land-surface model (LSM) use the calculations from the SL scheme, information from the radiative scheme and precipitation from the microphysics scheme. The LSM merges these schemes along with the land's state variables, the land-surface properties and calculates moisture fluxes over land and sea-ice points [64]. The LSM provide the lower boundary condition for the vertical transport in the PBL. The LSMs handles vegetation, root and canopy effects and surface-snow conditions for modelling thermal and moisture fluxes at the surface. The LSM can be viewed as a vertical profile of each WRF grid point that provides information about for example the soil temperature profile, soil moisture profile, the surface skin temperature and the snow-cover [64].

In this thesis, the Noah LSM is used. This scheme is the unified code for research and operational purposes [64].

4.2.12   Planetary boundary layer schemes

The lowest part of the atmosphere is known as the planetary boundary layer (PBL) or the atomspheric boundary layer. The PBL is extending from the ground surface to the so-called "free atmosphere" where the wind is at *geostrophic balance*. Geostrophic balance is derived in Appendix G: *Geostrophic balance*. The

PBL schemes were developed for improved modelling the fluxes of heat, moisture and momentum in the atmosphere [18] and the accurate representation of meteorological condition at typical wind turbine heights depends on the correct parameterization scheme for the PBL. Balzarini et al. [2] argues that PBL parameters are one of the most uncertain parameters in model estimates.

The PBL schemes handles the vertical sub-grid-scale fluxes due to eddy transports in the atmospheric column. The surface fluxes are provided by the SL and LSM schemes. There are two types of available PBL parameterization schemes, namely first order closure schemes and turbulent kinetic energy closure schemes. Turbulent kinetic energy closure schemes are most relevant for this study, as turbulent kinetic energy will be studied.

The turbulent kinetic energy (TKE) closure schemes are one and a half order closure schemes [64]. The Bougeaukt-Lacarrére (BouLac), Mellor-Yamada-Janic (MYJ) and the Quasi-normal scale elimination (QNSE) are all TKE parametrization schemes for the PBL [7].

The QNSE scheme is a model that are mainly suitable for a stably stratified fluid flow and for weakly unstable conditions [69]. The QNSE scheme is similar to the MYJ scheme during neutral and unstable conditions, but differs at stable conditions [18].

In their study [61] found that no PBL scheme satisfactorily simulated stable boundary layer and that the local TKE closure schemes generally performs better than the first-order schemes. The different surface layer schemes strongly influenced the thermodynamic surface variables. In a study done by Dimitrova et al. [19] the best suited PBL scheme of near-surface temperature (2 meters a.g.l.) and near-surface wind (10 meters a.g.l.) was the QNSE scheme.

The MYJ scheme is used in this study.

4.2.13   Parameterization remarks

This section will present the concluding remarks obtained from former studies of parameterization sensitivity.

In their study of seasonal dependence of WRF model biases, García-Díez et al. [27] pointed out that the model mean bias strongly depend on the season. They concluded that fitting parameterization schemes based on short-term studies could lead to a misrepresentation for other seasons. A sensitivity study done by Carvalho et al. [11] shows that the error in wind simulations can be significantly reduced by choosing the best suited numerical and physical WRF

configurations along with increasing the resolution of the terrain data. In their study on the three PBL schemes MYJ, Yonsei University (YSU) and asymmetric convective model, version 2 (ACM2), Hu et al. [30] found that the differences between these three schemes was predominantly due to the differences in the vertical mixing strength and the vertical wind from above the PBL.

In a study by Shin and Hong [61] the five PBL schemes YSU, ACM2, MYJ, BouLac and the QNSE scheme were compared with a focus toward the near-surface PBL properties. The simulation time was a single day and the comparisons revealed that the surface variables showed larger discrepancies during daytime and showed convergence during nighttime. They pointed out that the TKE closure schemes showed better performance than the first order schemes at stable conditions.

In a study for the Keiga nuclear power plant, Shrivastava et al. [62] concluded that no single combination of the WRF physics options gave superior results for all meteorological variables at the site. They concluded that in the case of simulating wind speed and direction, the combination of the MYJ (also referred to as Eta) PBL scheme, the Monon Obhukhov (also referred to as Eta) SL scheme and the Noah LSM scheme reproduced the on-site observations reasonably well in most of the considered cases.

4.2.14   Summary of WRF configurations

Some of the parametrizations chosen for the simulations throughout in this thesis is summarized in Tab. 4.2. This is just an overview of some configuration option but there are several more. Both namelists are appended and can be examined in Appendix E: *Namelists*.

Table 4.2: Overview of some of the WRF configurations used throughout this thesis. The asterisk is used to denote that this is the most common configuration, although not the only one used.

WRF model	WRF V3.7.1
WRF dynamical solver	ARW
Domains	3*, telescoping nests
2-way nesting	D01: False
	D02: True
	D03: True
Domain grid spacing*	D01: dx = 18000 m, dy = 18000 m
	D02: dx = 6000 m, dy = 6000 m
	D03: dx = 2000 m, dy = 2000 m
Map projection	Polar stereographic
Time step	90 seconds* (see Eq. 4.2.3)
Adaptive time step	False
Integration scheme	RK3
Advection scheme	5th order advection
Temporal resolution of out-files	10 minutes intervals
Number of vertical levels*	51, see Fig. 4.4.
Microphysics	WSM5
SL scheme	Monin Obhukhov
Land-surface model	Noah Land-Surface model
PBL scheme	MYJ, TKE scheme
Cumulus	Betts-Miller-Janic scheme
Number of soil layers	4
Longwave radiation	New Goddard
Shortwave radiation	New Goddard
Urban physics	Multi-layer BEP scheme (works only with the MYJ and BouLac PBL schemes)
Grid nudging (Newtonian relaxation)	No grid nudging
Eddy coefficient option	Horizontal Smagorinsky 1st order closure (recommended for real-data cases)
Turbulence and mixing	2nd order diffusion term (recommended for real-data cases)
Base-state sea level temperature	290 K

/5

Results

This chapter will present the results from on-site observations, reanalysis data from ERA-Interim and WRF simulations for establishing the capability and limitations of describing the wind resources at Rieppi. The data obtained from these three sources will be compared and discussed.

5.1   On-site measurements

An overview of the monthly mean wind speeds and standard deviations from mast 2503 are given in Fig. 5.1. The red dotted line represents the sample mean for the 2014 and is calculated to 7.47 m/s. As one can see from Fig. 5.1, the winter months have generally higher wind speeds than the summer months.
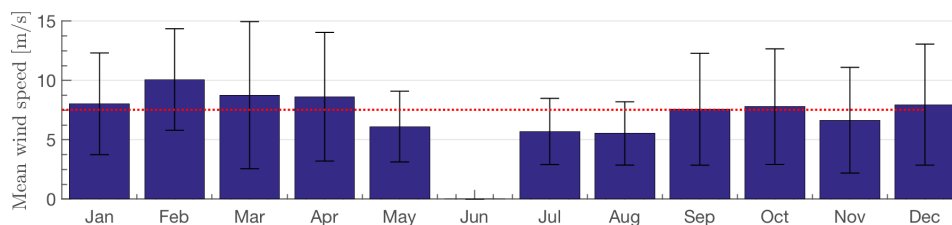
Figure 5.1: Monthly wind speed means with standard deviations for 2014, measured at mast 2503. The red dotted line represents the mean yearly wind speed of 7.47 m/s in 2014.

The winter months generally have a higher standard deviation than the summer months.

Figure 5.2 shows time series of the wind speeds at mast 2503 for 2014. The wind speeds in Fig. 5.2 are hourly averages. The red dashed line is the sample mean of the month.

At May 27, a lightening struck mast 2503. The logged measurements started again one month later, on June 27. Some of the sensors continued giving untrustworthy readings after June 27. The temperature sensor at 2 meters above ground level (abbreviated a.g.l.) recorded a temperature of -86 °C at June 28 with a standard deviation of zero. Because mast 2503 is lacking measurements, June is represented by the measurements from the WAS mas. This is plotted with a yellow line in Fig. 5.2. After June 28, at 10:20, the measurements seem reasonable.

It is not known if some or all sensors were replaced after the lightening.
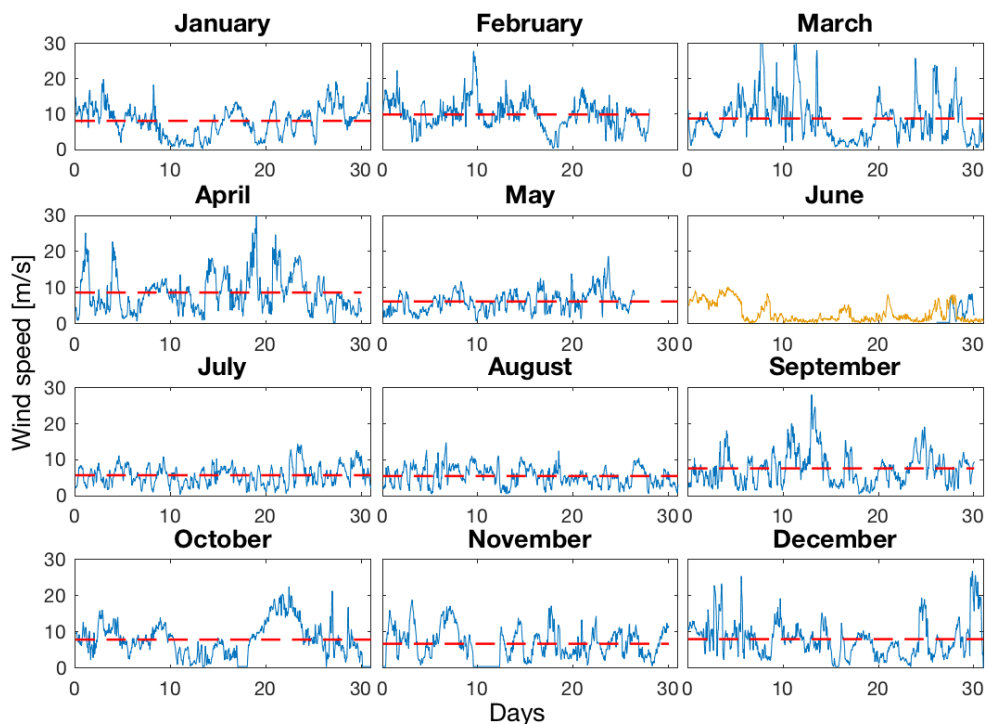
Figure 5.2: Plot of monthly wind speeds at mast 2503 for 2014. The dashed red line is the monthly mean.

Another irregularity in the observational data occurred November 10 to November 13, where the sensor logged zero wind speed and zero standard deviation. This indicates that the anemometer was either obstructed or damaged. A possible obstruction agent at this time of the year is icing.

A thorough examination of Fig. 5.2 and the recorded measurements reveals that there are three events with recorded wind speeds around zero. The first of these events occurs April 27, the second at October 17 and the third at October 30. For all three events, the wind speed display values close to zero, but not exactly zero, and the standard deviation is also non-zero. Judging from the other measurements it is very unusual that the wind speeds are close to zero, < 0,5 m/s for several hours. The reason for these calm wind speeds are not evident, but indicates that the anemometer was not functioning correctly.

5.1.1 On-site wind speed distribution

A normalized histogram of the wind speed distribution is plotted in Fig. 5.3 together with the theoretical Weibull probability density function (pdf) calculated from Eq. 3.3.15. The scale parameter a and shape parameter b are calculated using Eq. 3.3.20 and Eq. 3.3.19 to 8.36 m/s and approximately 1.36, respectively. The estimated mean from the Weibull pdf was calculated to 7.48 m/s with a standard deviation of approximately 4.7 m/s. The Weibull-estimated mean is close to the mean from the measurements of 7.47 m/s. The histogram
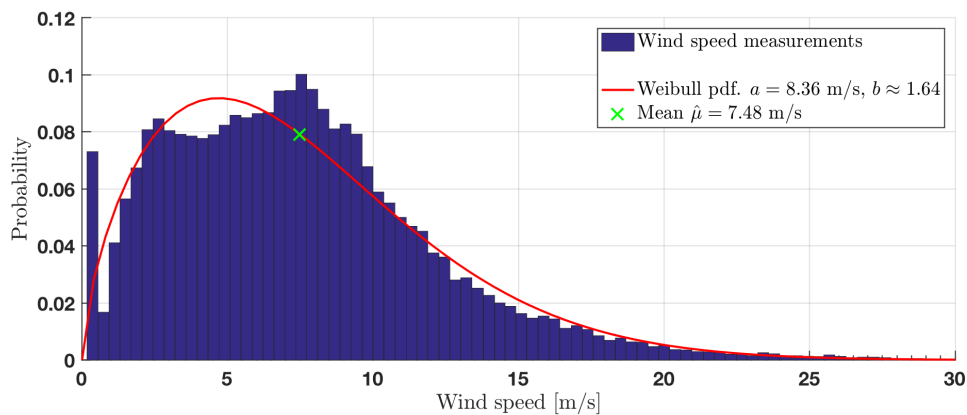
Figure 5.3: Normalized histogram of the on-site measurements with the fitted Weibull pdf (red line). The Weibull-estimated mean is marked with a green 'x'.

in Fig. 5.3 shows three distinct peaks. Conradsen et al. [16] pointed out that cup anemometers typically have relatively high wind speed thresholds. This can result in an exaggeration of calm and low wind speeds. The first standalone peak may originate from this threshold. The two other peaks at around 2,5 m/s

and 8 m/s point towards a bimodal distribution. The reason for this behaviour might be due to the surrounding topography at Rieppi, where the wind speed probability depends on the direction of the wind. Both the histogram and the Weibull pdf shows that the occurrence and the probability of extreme winds over 25 m/s are very rare, only 0,5% of all recorded wind speeds exceeds 25 m/s.

5.1.2 Prevailing wind directions

The valley surrounding the Rieppi site, namely the Skibotn valley, is oriented in the SE-NW direction (see Fig. 3.1b and Fig. 3.2b). As one might expect, the dominant wind direction is following the valley, namely from SE towards NW and from NW towards SE. An overview of the measured wind speeds and the corresponding directions is plotted in Fig. 5.4. In this figure, one can observe that the highest recorded wind speeds are from WNW at approximately 280 °. It seems like wind speeds from WNW has a higher probability go high wind speeds than the other peak at SSE. This supports the bimodal behaviour of the Weibull distribution discussed in the previous section. The sample mean is plotted with a green dash-dot line. The red dashed line is plotted at 12 m/s, which is a high wind threshold that will be discussed in a later section. The mean wind direction for 2014 was 159.8 degrees, using Eq. 3.3.9 according to Berens et al. [3].
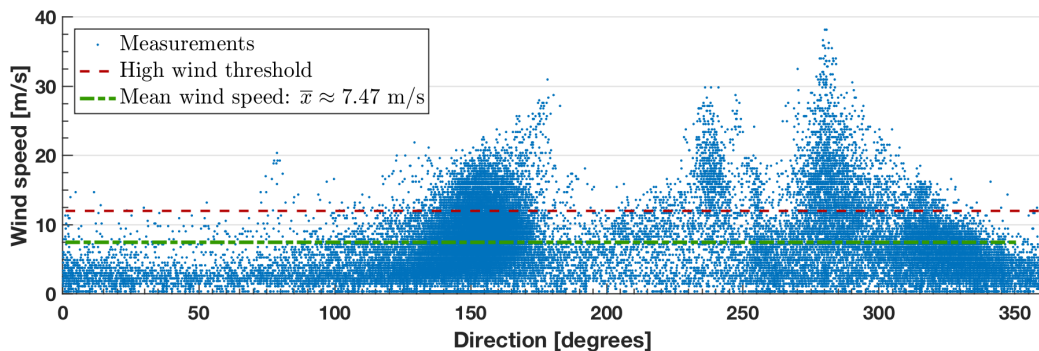
Figure 5.4: Measured wind speeds and direction for 2014. The high wind threshold of 12 m/s and the mean wind speed are indicated with a red and green line, respectively.

The wind direction denotes where the wind is from. That means that a wind direction of 315 ° is a wind from NW.

For investigating seasonal variances in the wind speed and directions, wind roses corresponding to each quarterly are plotted in Fig. 5.5a - 5.5d. Figure 5.5e

is the sum of all measurements at mast 2503 for 2014.

The length of the sectors in the wind rose plots are set dynamically. This is done so that it is easy to distinguish between wind speeds and sectors. One has to be aware of this and not get confused and concluding that the wind speeds in April to June, Fig. 5.5b, have equally high wind speeds as July to September in Fig. 5.5c.

5.1.3   Historical on-site measurements

For assessing whether or not 2014 was a representative year, a climatology of wind speed and wind directions has been made. Because the WAS mast is the only mast with data older than 2014, measurements from this mast are used for the climatology. The WAS mast is a 10 meter tall mast, and thus not perfect for investigating the wind speed and generalize this to mast 2503, which is 50 meters a.g.l.

The measurements available from the WAS mast begin in October 2003. The climatology is made from daily averages from January 1, 2004 to the December 31, 2013. The monthly means and standard deviations are tabulated in Tab. 5.1. From the sum of all months, one can observe that 2014 is about 3,4% below the climatology mean. The seasonal variations seems to be larger in 2014 than the seasonal variance in the climatology.

Table 5.1: Monthly wind speed means and standard deviations for climatology (2004-2013) are compared to 2014. The measurements are from the WAS mast.

Month	$\overline{x}_{\text{climatology}}$	$s_{\text{climatology}}$	$\overline{x}_{2014}$	s_{2014}
January	7.29	5.29	6.13	5.81
February	7.89	5.67	10.39	5.71
March	6.61	5.11	7.14	5.23
April	6.83	4.46	7.74	4.94
May	6.02	3.95	4.68	3.51
June	5.06	3.11	4.27	2.91
July	5.15	3.20	4.36	3.08
August	4.96	3.20	4.07	2.80
September	6.34	3.71	5.58	3.88
October	6.38	4.41	8.37	6.06
November	6.95	4.97	5.67	4.99
December	7.26	5.45	6.12	5.20
Sum of all months	6.43	4.80	6.21	5.00

The wind speed means and standard deviations are plotted in Fig. 5.6, where

(a) January to March

(b) April to June

(c) July to September

(d) October to December

(e) Wind speed over one year.
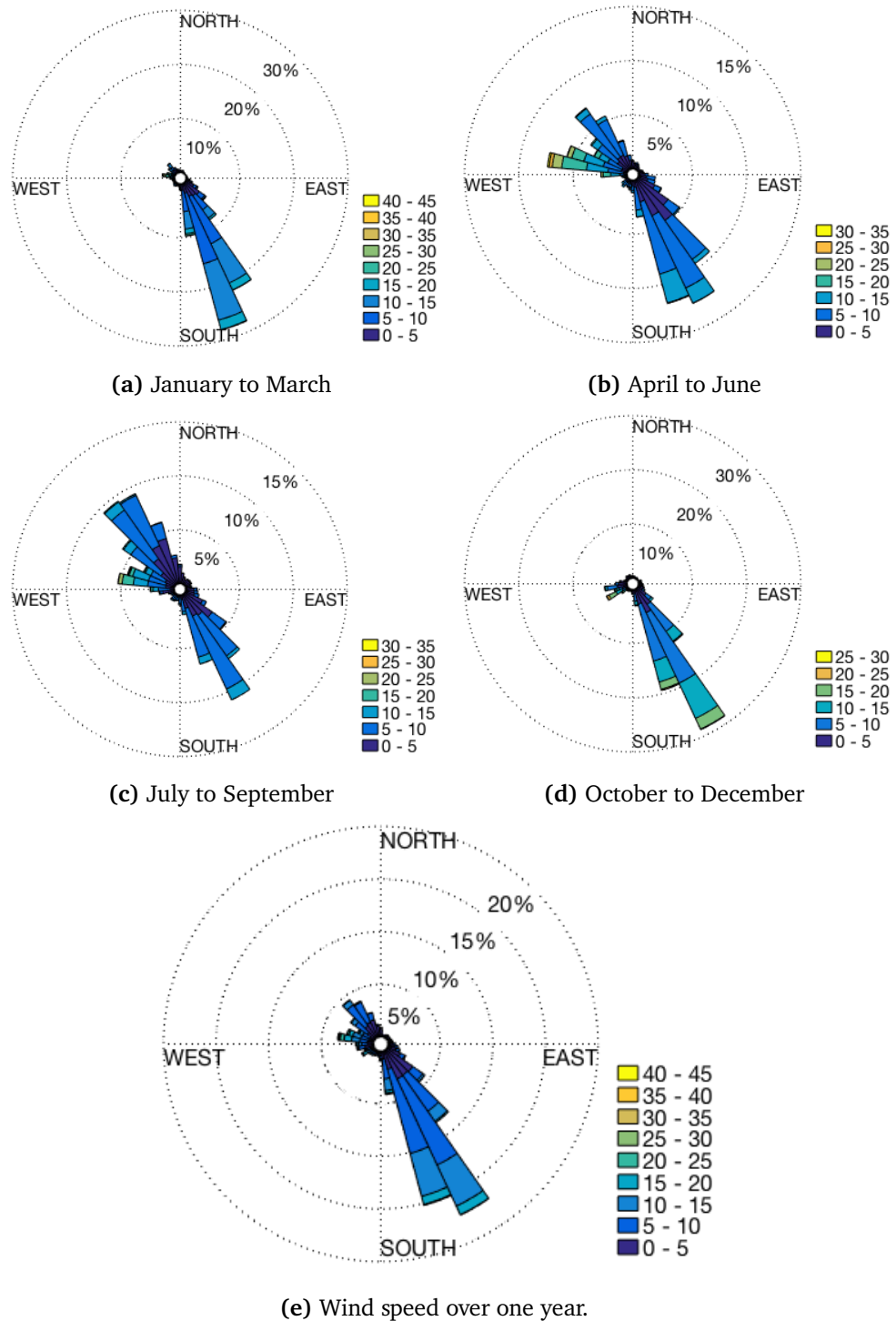
Figure 5.5: Wind roses of one year (2014) measured at 49.1 m elevation at site 2503. Fig. a-d is quarterly wind distrubutions, and Fig. e is the sum of a, b, c and d. The unit of the colorbar right of the wind roses is m/s.

the blue circles and error bars represent the mean and standard deviation of the wind speed from climatology and the red triangles and error bars represent the mean and standard deviation for measurements from 2014. For highlighting the differences between the two time series, 4th order polynomials are fitted to the monthly means. The blue dashed line is fitted to the climatology and the red dash-dot line is fitted to the measurements from 2014.
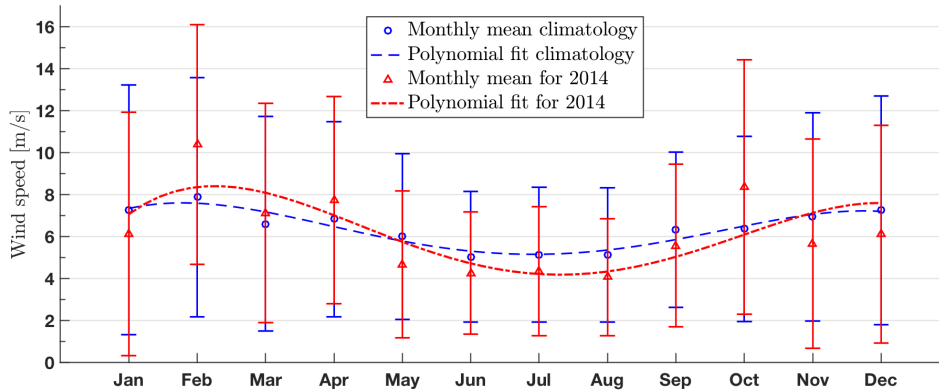
Figure 5.6: Monthly wind speed means from the climatology (blue) is compared to measurements from 2014 (red). The dashed and dash-dot line are fitted by using 4th order polynomials for better visualization.

Figure 5.7 shows the comparisons between wind speed and wind direction from the climatology and measurements from 2014. The sample means and high wind threshold are also plotted. It might be difficult to see the sample mean from the climatology (yellow dotted line) because the sample mean from 2014 is plotted above (purple dash-dot line). This indicates that the two sample means are similar.
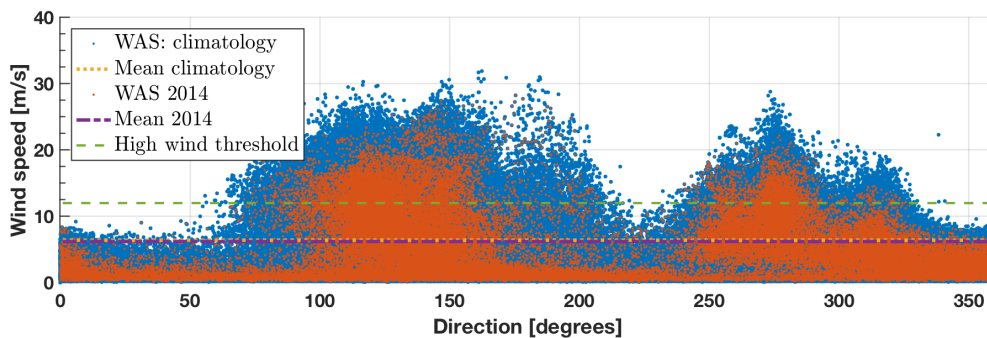
Figure 5.7: Wind speed vs. direction for comparing the climatology (blue) against the measurements for 2014 (orange) from the WAS mast. The mean wind speed for the climatology is market with yellow dashed line, the mean wind is marked with a purple dashed line. The high wind threshold is also shown.

Normalized histograms the climatology and measurements from 2014 are plotted in Fig. 5.8a and 5.8b. A Weibull pdf is plotted and the estimated means are marked. The Weibull-estimated mean for 2014 was calculated to approximately 6.20 m/s. The sample mean from the data set is 6.21 m/s. The Weibull-estimated mean for the climatology is 6.43 m/s, which is the same as the sample mean.

(a)   **(b)**
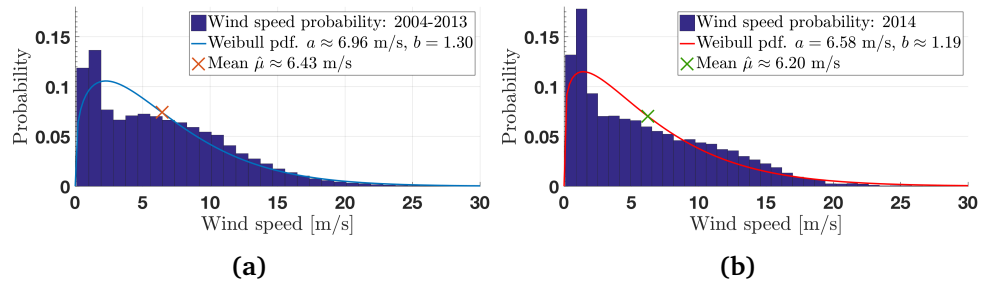
Figure 5.8: Wind speed distribution measured at the WAS mast. a: Weibull distribution for the period 2004-2013. Weibull pdf with blue curve. b: Weibull distribution for 2014, Weibull pdf with red curve.

Figure 5.8 shows that wind speeds between 0 and 2,5 m/s are dominating the distribution. One would expect a higher frequency of very low wind speeds when comparing to the 40 meter taller 2503 mast which is also located at higher terrain. This, in combination with the threshold of the anemometer discussed in subsection 5.1.1, might explain the overrepresentation of the very low wind speeds at mast WAS.

In summary, the overall mean wind speed from 2014 is approximately 3,4% below the mean for the period 2004-2013 and although there are larger seasonal variations when regarding the monthly mean wind speeds in 2014 than in the climatology, the main seasonal trend is the same, i.e. winter months have higher mean wind speed than summer months. The Weibull-estimated mean wind speeds corroborates the sample means. Additionally, Fig. 5.7 indicates that the prevailing wind directions in 2014 is similar to the climatology. Based on these aspects, I regard 2014 to be sufficient for representing the wind speeds and directions at Rieppi.

5.2 ERA-Interim reanalysis data

As emphasised in Chapter 3, the ERA-Interim reanalysis data have a spatial horizontal resolution of approximately 80 km and a temporal resolution of 6 hours.

The mean, standard deviation and correlation coefficients between the on-site observations and ERA-Interim are calculated and tabulated in Tab. 5.2. A comparison of wind speed and direction and temperature at 2 meters a.g.l. from on-site measurements and ERA-Interim is plotted in Fig. 5.9. The lacking measurements from the on-site observations are due to the lightening incident mentioned in section 5.1.

Table 5.2: Comparisons of mean wind speeds and standard deviations from on-site observations and ERA-Interim with the corresponding correlation coefficients.

Variable	On-site		ERA-Interim		Correlation coeff.
	$\overline{x}_{obs}$	s_{obs}	$\overline{x}_{ERA}$	s_{ERA}	
Wind speed	7.47	4.68	4.31	2.39	0.413
Wind direction	159.8	95.7	173.5	92.9	0.781
Temp. at 2 m a.g.l.	-0.72	10.56	-0.06	8.61	0.786
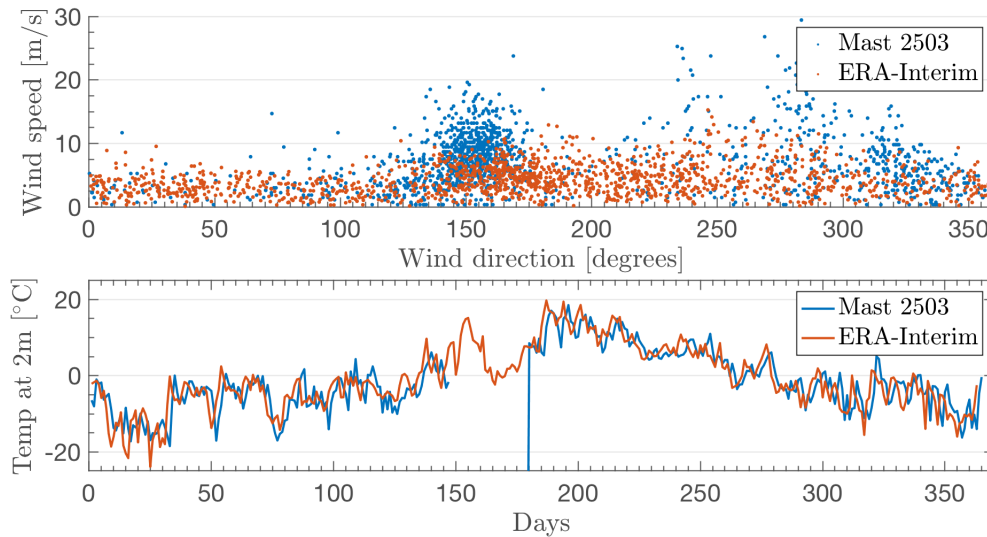
Figure 5.9: Comparisons of wind speed and direction (top) and temperature (bottom) between on-site observations and ERA-Interim.

Figure 5.9 indicates that ERA-Interim fails at representing the prevailing wind directions from the on-site observations. Moreover, the reanalysis data might have a higher density of data at winds from SE, but the distinct two peaks at $\sim 150\,°$ and $\sim 280\,°$ from the on-site observations (these two are more evident in Fig. 5.4) is not reflected in wind speeds from the ERA-Interim data.

Despite the low correlation of the upper plot of Fig. 5.9, the temperature from ERA-Interim has a high correlation with the on-site observations. The high correlation is corroborated by the lower plot in Fig. 5.9.

5.3   WRF simulations

All months in 2014 are simulated using WRF. The model setup for all the monthly simulations is summarized in Chapter 3, Tab. 4.2.

The correlations and RMSE between the WRF domains and mast 2503 can be examined in Tab. 5.3. The compared parameters in Tab. 5.3 are wind speed, wind direction and temperature at 2 meters a.g.l. Monthly means and standard deviations are tabulated in Tab. 5.4 for on-site observations, ERA-Interim, and all three WRF domains.

Due to the previously mentioned lightening that led to corrupted data between May 27 and June 27, the WRF simulation for May is cropped at May 27 for making the comparisons to the on-site observations valid. This "cropping" is denoted by a asterisk in Tab. 5.3. Because of the lack of measurements, June is not simulated.

Table 5.3: Table of correlation coefficients and RMSE between on-site observations and WRF outputs for all the three domains using Eq. 3.3.6, Eq. 3.3.13 and Eq. 3.3.7. June is omitted.

		Domain 1	Domain 2	Domain 3
January	Correlation wind speed	0.334	0.406	0.424
	Correlation wind dir.	0.890	0.902	0.934
	Correlation 2 m temp	0.513	0.528	0.523
	RMSE wind speed	206.5	156.4	147.3
	RMSE 2 m temp.	10.60	76.5	48.9
February	Correlation wind speed	0.336	0.519	0.625
	Correlation wind dir.	0.963	0.975	0.968
	Correlation 2 m temp	0.891	0.894	0.880
	RMSE wind speed	215.8	52.4	94.3
	RMSE 2 m temp.	229.3	153.2	174.3
March	Correlation wind speed	0.641	0.631	0.660
	Correlation wind dir.	0.931	0.934	0.933
	Correlation 2 m temp	0.920	0.917	0.910
	RMSE wind speed	13.2	23.5	56.6
	RMSE 2 m temp.	224.5	117.3	112.6
April	Correlation wind speed	0.634	0.604	0.603
	Correlation wind dir.	0.940	0.944	0.923
	Correlation 2 m temp	0.868	0.867	0.865
	RMSE wind speed	29.5	82.3	61.5
	RMSE 2 m temp.	289.4	194.8	175.3

Table 5.3: Table of correlation coefficients and RMSE between on-site observations and WRF outputs for all the three domains using Eq. 3.3.6, Eq. 3.3.13 and Eq. 3.3.7. June is omitted.

		Domain 1	**Domain 2**	**Domain 3**
May [*]	Correlation wind speed	0.339	0.478	0.512
	Correlation wind dir.	0.892	0.919	0.892
	Correlation 2 m temp	0.893	0.900	0.903
	RMSE wind speed	55.9	15.1	82.7
	RMSE 2 m temp.	288.4	213.6	197.5
July	Correlation wind speed	0.588	0.654	0.637
	Correlation wind dir.	0.928	0.919	0.925
	Correlation 2 m temp	0.903	0.910	0.911
	RMSE wind speed	96.1	56.6	65.4
	RMSE 2 m temp.	110.9	37.7	20.8
August	Correlation wind speed	0.457	0.525	0.497
	Correlation wind dir.	0.890	0.897	0.877
	Correlation 2 m temp	0.935	0.937	0.939
	RMSE wind speed	60.6	66.4	72.7
	RMSE 2 m temp.	180.7	79.9	54.2
September	Correlation wind speed	0.670	0.541	0.584
	Correlation wind dir.	0.815	0.813	0.787
	Correlation 2 m temp	0.934	0.944	0.943
	RMSE wind speed	18.3	52.1	169.8
	RMSE 2 m temp.	173.2	78.5	48.1
October	Correlation wind speed	0.698	0.801	0.795
	Correlation wind dir.	0.925	0.942	0.890
	Correlation 2 m temp	0.930	0.935	0.934
	RMSE wind speed	125.1	71.1	113.5
	RMSE 2 m temp.	162.4	61.2	48.1
November	Correlation wind speed	0.175	0.492	0.665
	Correlation wind dir.	0.922	0.943	0.918
	Correlation 2 m temp	0.818	0.833	0.829
	RMSE wind speed	56.8	2.7	101.7
	RMSE 2 m temp.	73.2	11.1	9.5
December	Correlation wind speed	0.563	0.582	0.549
	Correlation wind dir.	0.924	0.956	0.935
	Correlation 2 m temp	0.837	0.832	0.808
	RMSE wind speed	95.3	34.1	132.4
	RMSE 2 m temp.	188.0	95.0	121.5
Total	Correlation wind speed	0.526	0.600	0.633
	Correlation wind dir.	0.897	0.907	0.900
	Correlation 2 m temp	0.953	0.955	0.955

Based on the monthly comparisons of on-site measurements agains the three
WRF simulation domains, some remarks on the domain performance can be
done. From Tab. 5.3 and Fig. 5.10 it is not obvious that domain 3 is more
accurate than the coarser domains 1 and 2. In fact, domain 2 has the highest
correlation coefficient for many months. The wind speed shows an overall lower
correlation than the wind direction and temperature at 2 meters a.g.l.

The total sum of 2014 in Tab. 5.3 shows that domain 3 has the highest correlation
coefficient for wind speed and domain 2 has the highest coefficient for wind
direction. At the 2 m temperature, all three domains give similar results with
domain 2 and 3 giving the highest correlation coefficients.

Figure 5.10 shows a visulization of the correlation coefficient from Tab. 5.3. The
correlation between all WRF-domains and the on-site observations are high,
as emphasised in Tab. 5.3.
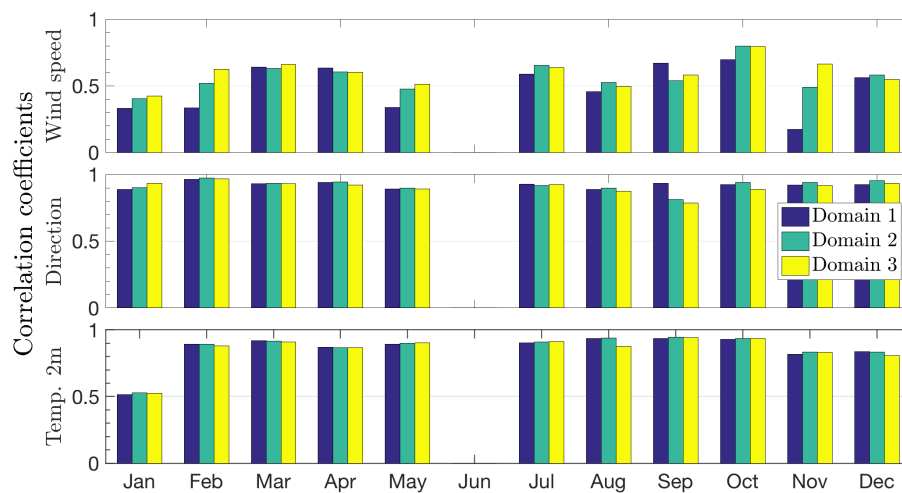
Figure 5.10: Graphical representation of the correlation coefficients from Tab. 5.3.
The wind speed, wind direction and temperature at 2 meters a.g.l. are
used for comparing the on-site observations to all three WRF simulation
domains.

For a more thorough investigation of the differences between monthly on-
site observations, ERA-Interim and the WRF simulations, July and October are
plotted in Fig. 5.11 and Fig. 5.12. The figures presents horizontal wind speed and
temperature at 2 meter for July and October. The figures shows comparisons
of on-site measurements (blue line), ERA-Interim (green circles) and WRF
simulations for domain 1, 2 and 3, (red, yellow and purple, respecitvely).
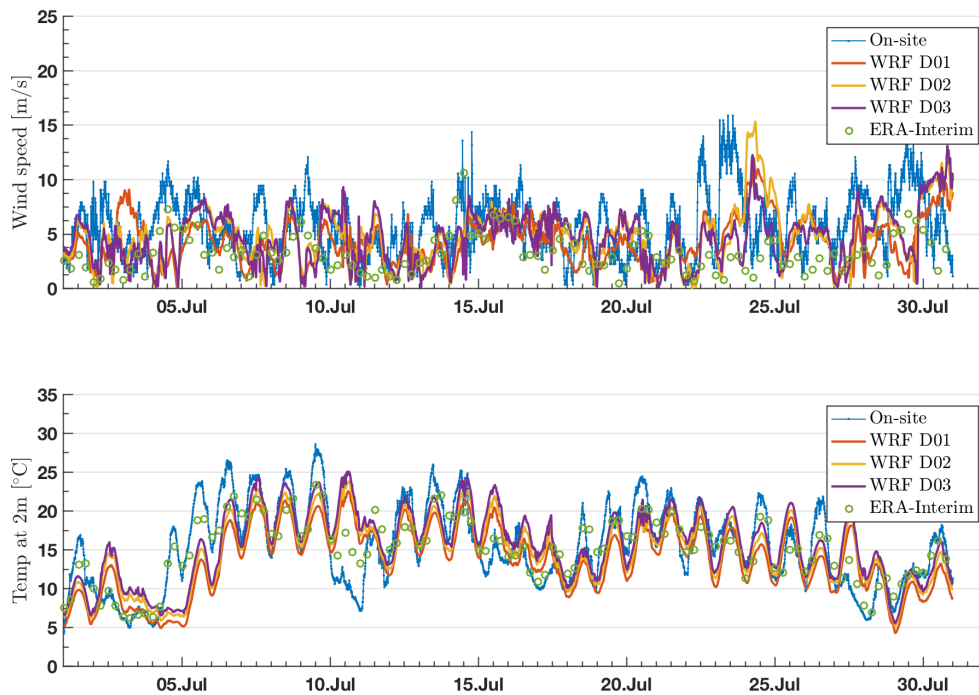
Figure 5.11: Wind speed (top) and temperature at 2 meters a.g.l. (bottom) at Rieppi for July 2014. Plot of all three domains of WRF (D01, D02 and D03), on-site observations and ERA-Interim.

July has generally low wind speeds, i.e. below 10 m/s and the WRF simulation seems to represent the wind speeds accurately, with a RMSE of 65.4 m/s (between domain 3 and on-site obs.). There are some events that WRF is not able to represent, like July 23 to July 24, where the WRF model underestimates the on-site wind speeds. It seems like the WRF model is unable to capture wind gusts like for example at mid-day July 14, where there are two spikes from the on-site measurements at almost 15 m/s, while the WRF-simulation shows wind speeds below 10 m/s.

October has a higher measured mean wind speed of 7,8 m/s and a standard deviation of 4,7 m/s. The RMSE between WRF domain 3 and the on-site observations is 113,5 m/s. Figure 5.12 indicates that WRF is more accurate at representing low wind speeds than higher wind speeds. This is particularly evident in the time period October 21 to October 24, where WRF systematically underestimates the wind speed. From the figure it seems like ERA-Interim is also not able to represent these high wind speeds. Because ERA-Interim is used as initial and boundary data, the poor WRF results might be caused by the low input wind speeds from ERA-Interim. As implied by Tab. 5.3, the temperature at 2 meter is accurate most of the time, even though some large deviations

occur, e.g. July 10 to July 11.
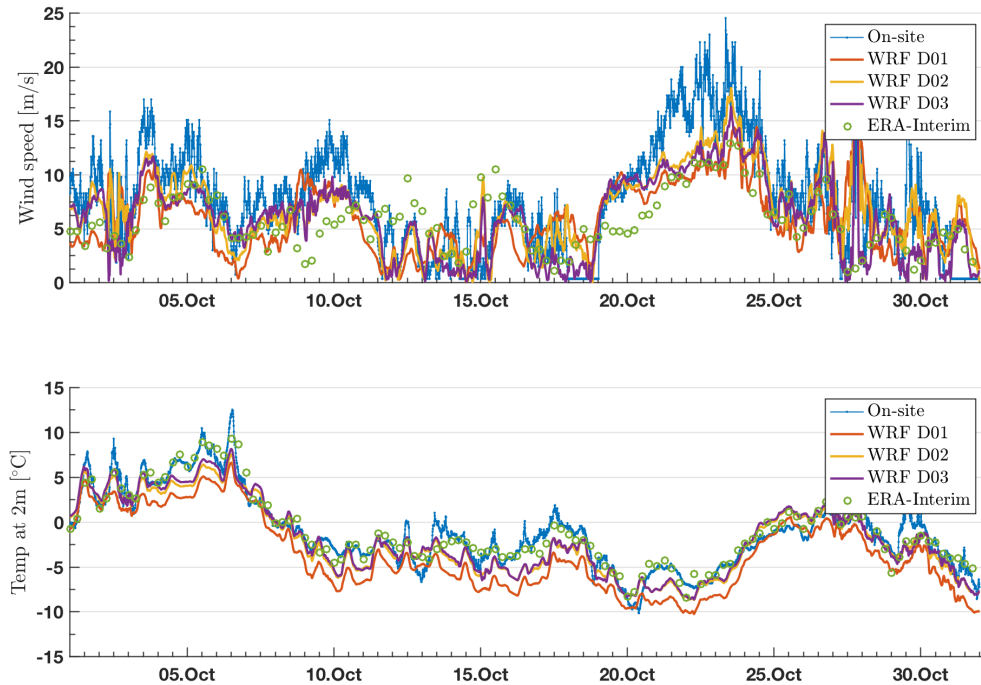
Figure 5.12: Wind speed (top) and temperature at 2 meters a.g.l. (bottom) at Rieppi
for October 2014.

5.3.1   Comparing the data sources

Table 5.4 shows comparisons of the sample mean and standard deviations from
on-site observations, ERA-Interim and all three domains from WRF. The WRF
and on-site data is computed from 6 hour averages to match ERA-Interim. The
asterisk indicates that May is cropped. The data presented in the table affirms
that the three WRF domains give similar results at the Rieppi site. Domain 2 is
closest to the on-site sample mean, but has a larger standard deviation than
the other domains. Like Fig. 5.1, the table highlights that months with high
mean wind speeds also have a higher standard deviation.

From Tab. 5.4, it is clear that both ERA-Interim and WRF systematically under-
estimate the actual wind speeds. The ERA-Interim data show especially low
mean wind speeds. Interestingly, the second domain generally predicts higher
wind speeds than the other two domains, and both domain 1 and 2 gives a more
accurate mean wind speed than domain 3 based on the monthly means. The
reason for this might be that domain 1 has the largest grid spacing of 18000
meters between each grid point both in the east-west and the south-north
direction. Domain 2 has a grid spacing of 6000 m and domain 3 has a grid

Table 5.4: Comparisons between monthly mean wind speeds from on-site observations, ERA-Interim and three domains of WRF. The asterisk in May denotes that it is cropped. The mean from June is omitted.

Month	On-site $\overline{x}$	On-site s	ERA-I. $\overline{x}_{ERA}$	ERA-I. s_{ERA}	WRF, D01 $\overline{x}_{D01}$	WRF, D01 s_{D01}	WRF, D02 $\overline{x}_{D02}$	WRF, D02 s_{D02}	WRF, D03 $\overline{x}_{D03}$	WRF, D03 s_{D03}
Jan	8.0	4.2	4.4	2.0	4.9	3.0	5.7	3.7	5.7	3.1
Feb	10.1	4.3	5.6	2.0	6.6	3.1	9.2	3.2	9.6	2.9
Mar	8.8	6.2	4.3	2,1	8.6	5.5	9.1	6.0	7.9	5.4
Apr	8.6	5.4	5.6	3.0	9.1	4.8	9.9	5.6	7.7	5.6
May *	5.6	3.0	5.6	2.9	5.2	3.2	5.9	4.4	4.8	3.6
Jun	–	–	–	–	–	–	–	–	–	–
Jul	5.7	2.8	3.2	1.8	4.2	2.1	4.9	2.6	4.7	2.4
Aug	5.5	2.7	2.8	1.7	4.6	2.4	4.5	2.4	4.4	2.1
Sep	7.6	4.7	3.3	1.5	7.3	3.8	6.8	4.5	5.0	3.7
Oct	7.8	4.9	5.8	2.7	5.9	3.1	6.7	3.6	6.1	3.7
Nov	6.6	4.5	4.1	1.9	5.8	3.0	6.7	3.8	5.1	3.0
Dec	8.0	5.1	3.9	2.0	6.5	4.0	7.5	3.9	6.0	3.7
Total	7.5	4.7	4.3	2.4	6.3	3.9	7.0	4.5	6.0	3.9

spacing of 2000 m. The higher wind speed correlation might be due to the domain resolution where domain 1 perhaps is too coarse to capture the local wind pattern. Table 5.4 shows that the standard deviation increases at higher wind speeds.

The data tendencies are investigated using the Bias presented in Chapter 3. Figure 5.13 show the wind speeds for 2014, measured at mast 2503 against the wind speed from ERA-Interim and the three WRF domains. The on-site observations are extracted at the same time as the ERA-Interim data, i.e. with a 6 hours temporal resolution. The red line in Fig. 5.13 is a least-squares fitted regression line. If the Bias between two data sets is zero, they data points would be entered around the yellow dotted line. Figure 5.13 corroborate the underestimation of the on-site wind speeds where ERA-Interim has the largest bias. The smallest Bias is between on-site obs. and WRF, domain 2, as indicated in Tab. 5.4.

A similar tendency was found by Passner and Knapp [56], where a similar domain setup, i.e. 3 nested domains with grid spacing 18000 m, 6000 m and 2000m gave a smaller Bias for the largest domain than for the highest resolution domain. Passner and Knapp [56] also found that the simulation results from the coarsest domain provided highest correlation coefficient for temperature.
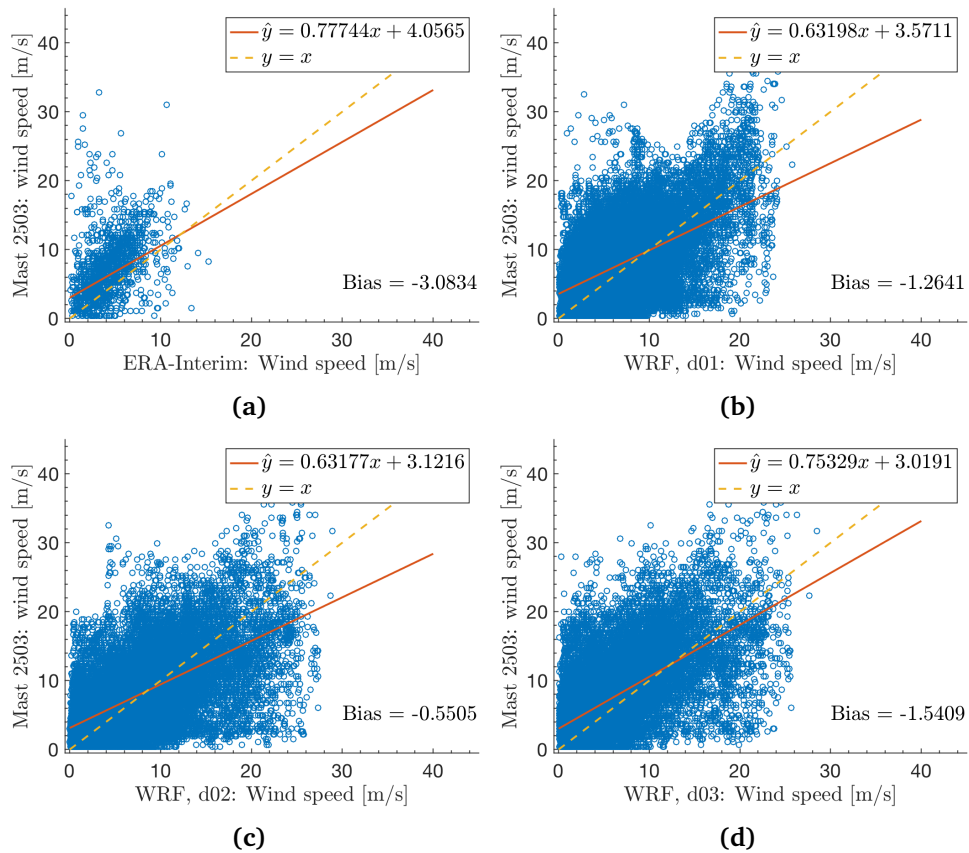
Figure 5.13: Evaluation of the Bias tendencies of wind speeds in 2014. The red line is a linear regression fit. The yellow dashed line corresponds to zero Bias. a: On-site observations for wind speed from mast 2504 agains ERA-Interim. b,c,d: On-site obs. against WRF, domain 1,2 and 3, respectively.

As domain 3 has the highest resolution and therefore the most detailed wind field, this is used for comparing the wind directions to the measurement mast and ERA-Interim. Quarterly wind roses are plotted in Fig. 5.14. The bottom row in Fig. 5.14 presents the sum of all wind directions in 2014.

The figure demonstrates that the wind directions obtained from ERA-Interim fail at representing the measured wind direction, while WRF, domain 3 show good agreement in most cases. One can also see that the wind speeds are lower in the ERA-Interim and the WRF column than the measured wind speed. It is important to note that the circles representing the percentage occurrence of wind speed and direction are set dynamically. This means that the length of one bin in one wind rose is not necessarily the same as a equal bin in another wind rose. The dotted circles indicates the duration of each bin.

Figure 5.14: Comparisons of the directions from on-site observations, ERA-Interim and WRF domain 3. The percentage of the wind roses are set dynamically.

5.3.2 Domain resolution

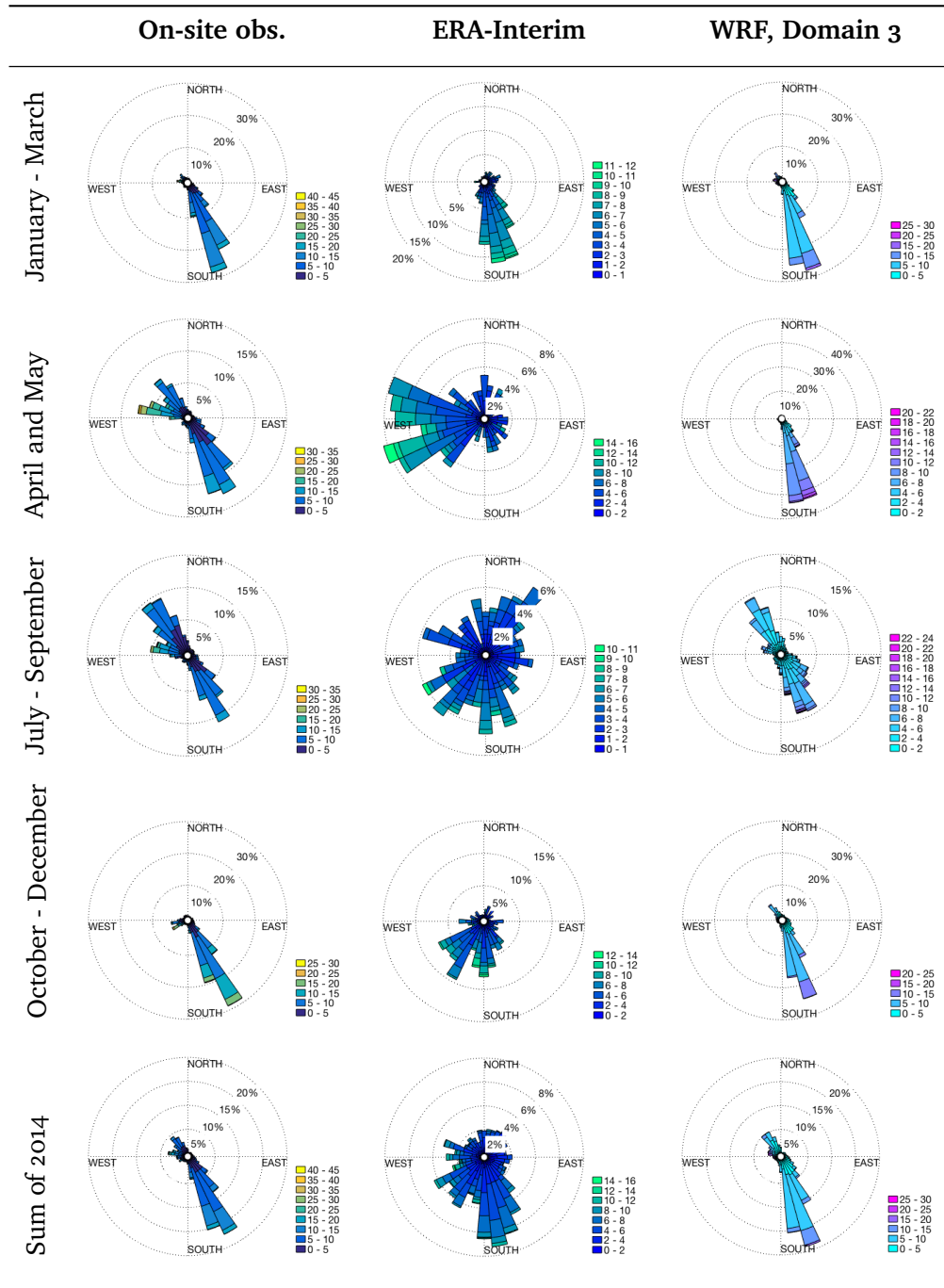From Tab. 5.3, Tab. 5.4, Fig. 5.10, Fig. 5.11 and Fig. 5.12 it is not transparent which domain configuration is best suited for reproducing the on-site measurements. Domain 2 seems to be best at accurately simulating the temperature at 2 meters a.g.l. and is closest to the measured total mean wind speed for 2014. Domain 3 gives the highest correlation coefficient for reproducing the wind speeds measured at mast 2503.

As mentioned in Chapter 3, the domain grid spacing is:

- D01: dx = 18000 m, dy = 18000 m

- D02: dx = 6000 m, dy = 6000 m

- D03: dx = 2000 m, dy = 2000 m.

For investigating the effect of domain resolution, the horizontal wind field over the Skibotn valley is simulated. The horizontal wind field is extracted at approximately 60 meters, according to the equation for geometric height (Eq. 2.4.3) and geopotential (Eq. 4.2.7) from Chapter 2.

Figure 5.15 shows the horizontal wind speed as a surface-contour plot along with wind barbs that indicate wind direction and speed. The time of the plot is December 1, at 12:00. Mast 2503 is marked with a black dot. The time is chosen because wind from SSE is typical for the site. Explanation of the wind barbs can be found in Appendix H: *Beauforts wind force scale*.

Wind barbs are usually plotted to that they do not overlap but in this case the wind barb density corresponds to the resolution of the grid spacing. One wind barb corresponds to one grid point in the WRF model. Figure 5.15a shows that the wind field from domain 1 is too coarse to capture the local wind flow through the valley and the surrounding topography has little influence on the wind field. Figure 5.15b provides more directional variation, and the terrain effects is more significant than domain 1, but domain 3 in Fig. 5.15c gives a superior wind field resolution. Domain 3 presents a detailed overview of the wind pattern throughout the valley and in the surrounding terrain. One effect of the higher resolution is that the maximum wind speeds on the mountain tops are higher at higher domain resolution. This increased wind speed at the tops might be due the interpolated simulation domain. Domains with a coarsely interpolated topography might not capture mountain peaks and ridges and thus underestimating the wind speed at these tops.

(a)

(b)

(c)
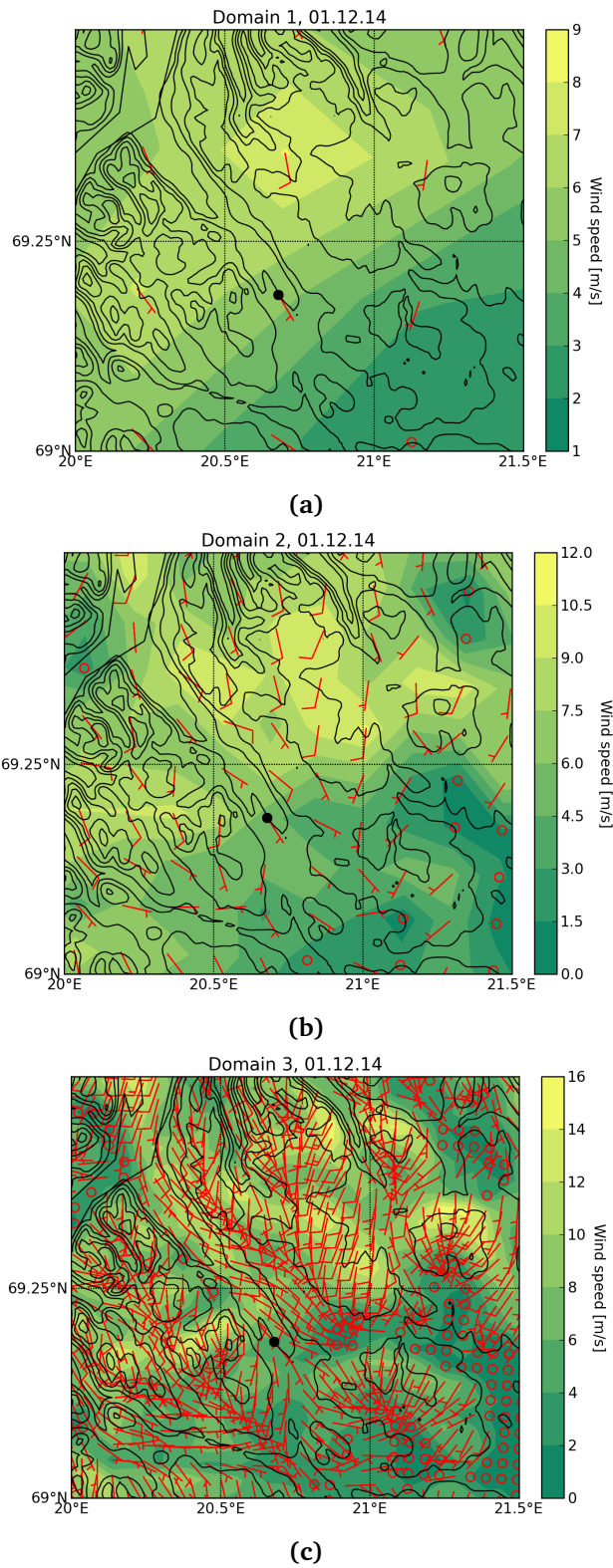
Figure 5.15: Wind field at 10 meters a.g.l. as a contour-surface plot with wind barbs for domain 1,2 and 3 in a, b and c respectively. The date and time is 1.December 2014 at 12:00. Mast 2503 is marked with a black dot.

In Fig. 5.15, the wind speed and direction at the site are approximately the same in all domains.

As the terrain effect seems to be more evident in domain 3 than the coarser domains, one would expect the wind direction in domain 3 to be more directionally stable than domain 1 and 2. Figure 5.16 exemplifies the differences in spread in wind directions from the three domains. The figure depicts comparisons between wind directions from on-site observations (blue) and the WRF domain 1, 2 and 3 (red, yellow and purple respectively).

(a) January   **(b)** March   **(c)** May

(d) August   **(e)** September   **(f)** October
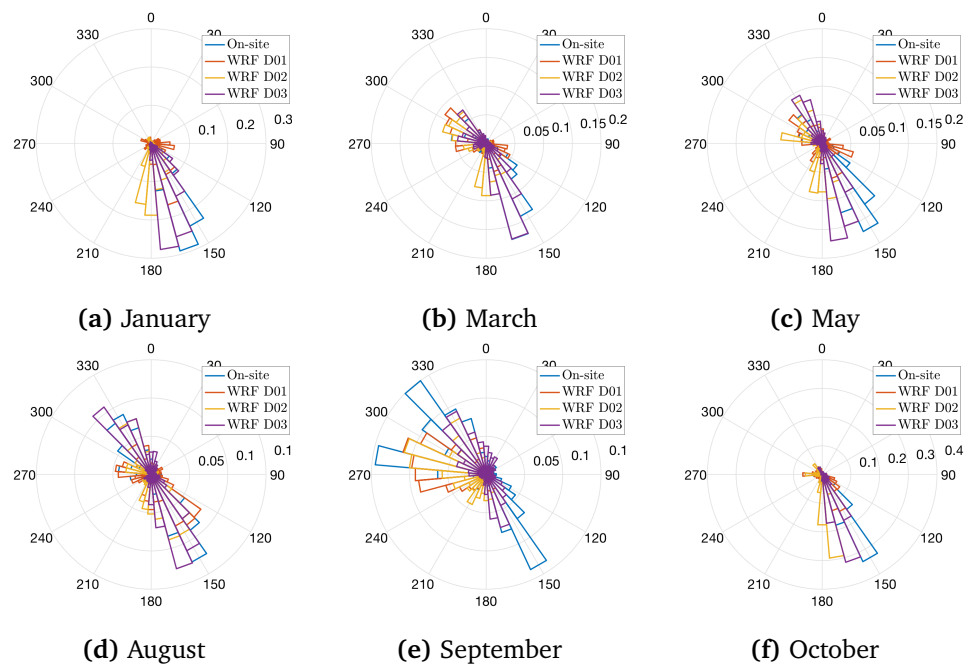
Figure 5.16: Wind sector comparisons between different domains and on-site observations from mast 2503. The radius of the circles denotes the fraction of the time each bin corresponds to.

Figure 5.16 indicates that the bins from domain 1 and 2 (orange and yellow respectively) are shorter and more widely dispersed than domain 3 (purple) and the wind directions from the on-site measurements. This point towards that domain 3 is more directionally stable than the two coarser domains. The examination of Fig. 5.16 shows that domain 3 provide the best agreement to the on-site measurements.

5.3.3 Potential power density estimates

As noted in Chapter 2, the power in the wind is proportional to the wind speed cubed. It is therefore obvious that a inaccurate prediction of high wind speeds leads to large inaccuracies when estimating the potential power.

In this thesis, the focus is on the *potential* power in the wind. The Betz' limit yields a theoretical maximum wind power of approximately 56,3% of the potential power as discussed in Chapter 2, section 2.6. A real turbine will clearly produce less power than this due to other factors like mechanical friction in the turbine, turbulence and icing.

The power density is the power divided by the unit area and can be expressed as

$$\tilde{P} = \frac{P}{A} = \frac{1}{2}\rho \boldsymbol{u}^3.$$
(5.3.1)

The power density is used for giving a quantitative power that is independent of the rotor diameter. To compute the potential power in the wind one would need the density of the fluid ρ and the horizontal wind speed $\boldsymbol{u}$. The ideal gas law (discussed in Chapter 2) yields that the density of a ideal gas can be expressed as

$$\rho = \frac{p}{RT},$$
(5.3.2)

where p is the pressure, R is the gas constant and T is the temperature of the fluid. As temperature and pressure change with altitude, so will the density of the fluid.

The power potential was calculated by approximating the density using surface pressure, temperature at 2 meters a.g.l. and the gas constant for dry air. For testing whether or not this approximation was valid, the fluids density was also estimated by calculating:

1. the gas constant for moist air

2. pressure at 60 meters a.g.l.

3. temperature at 60 meters a.g.l.

The pressure from WRF is given by a base-state and a perturbed state, and the pressure at a altitude z can be expressed as $p(z) = \bar{p}(z) + p'(z)$.

The four-dimensional temperature is not given explicitly in the WRF model, but the temperature at a certain altitude has to be calculated using *potential*

temperature. Potential temperature is defined as

$$\theta \equiv T\left(\frac{p_R}{p}\right)^{\kappa},\tag{5.3.3}$$

according to Vallis [72]. Potential temperature is derived and explained in Appendix I: *Potential temperature*. The reference pressure p_R is usually the temperature at the surface and will be denoted p_S. κ is defined as the ratio R/c_p and for moist air this is written as

$$\kappa \equiv \frac{R}{c_p} = \frac{R_d(1-q) + R_w q}{c_{p,d}(1-q) + c_{p,w} q},\tag{5.3.4}$$

As presented in Chapter 2. The constants can be examined in Appendix B: *Physical constants*.

The density can then be calculated by

$$\rho(z) = \frac{\overline{p}(z) + p'(z)}{\left(R_d(1-q) + R_w q\right)\theta\left(\frac{\overline{p}(z)+p'(z)}{p_S}\right)^{\kappa}},\tag{5.3.5}$$

where p_0 is the surface pressure. All quantities in Eq. 5.3.5 are either constants or can be extracted from the WRF model.

Using temperature and pressure at approximately 60 meters a.g.l. and the inclusion of moisture in the gas constant did not have any significant effect of the potential power estimate compared to the approximation where surface pressure, temperature at 2 meters a.g.l. and the gas constant for dry air.

The power potential is plotted for each quarterly in Fig. 5.17a-d. Figure 5.18 is the sum of 2014. The figure shows the normalized histogram from the on-site measurements for the period. The Weibull pdf of the on-site data is fitted to the wind speeds and plotted with a whole blue line. The blue dashed line shows the Weibull pdf fitted to simulation results from WRF, domain 3. The WRF data is extracted at approximately 60 meters a.g.l.

(a) January to March

(b) April to May

(c) July to September

(d) October to December
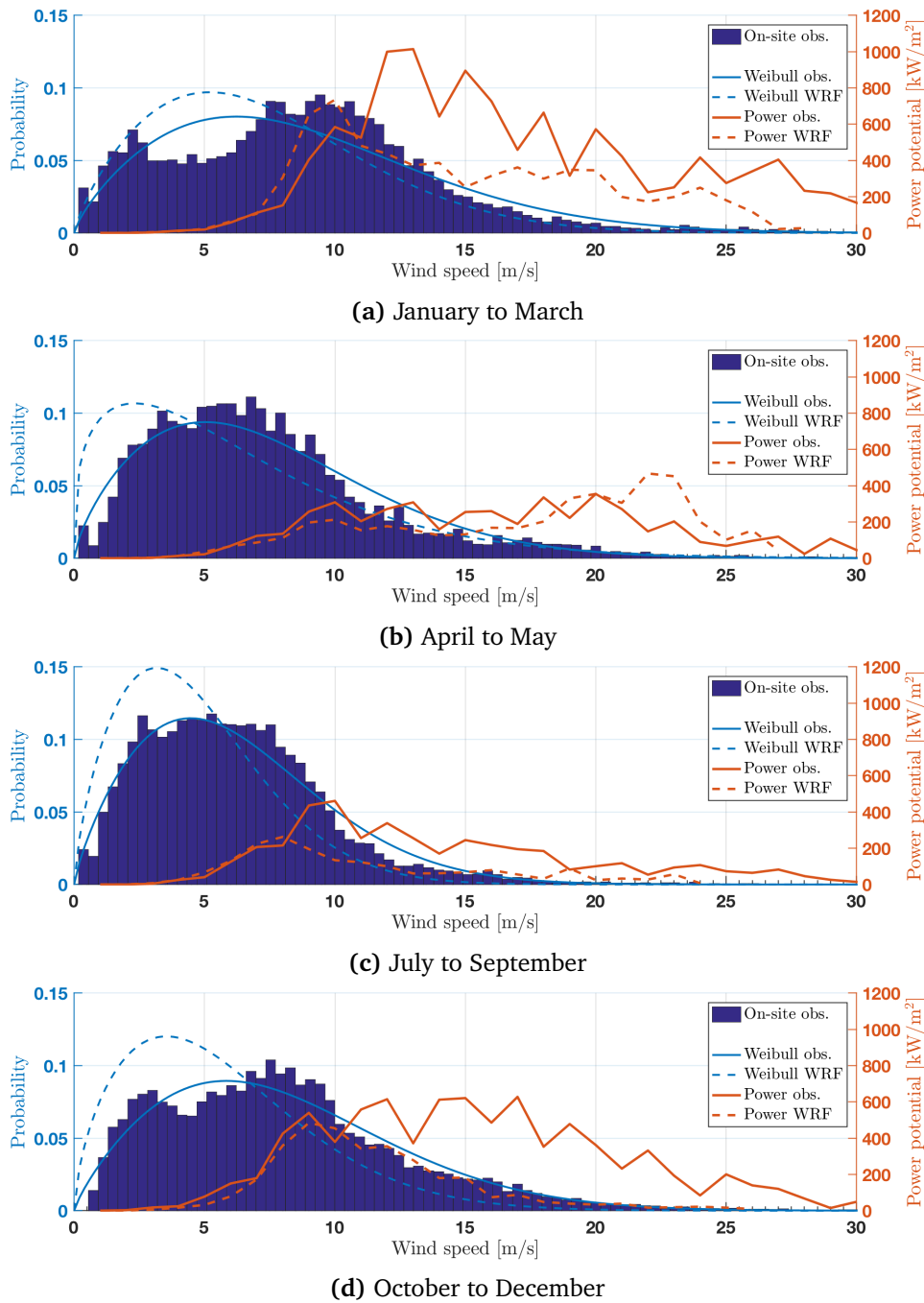
Figure 5.17: The on-site observations are plotted as normalized bar diagrams with Weibull pdf fitted (blue line). The dashed blue line is the Weibull pdf corresponding to the WRF-simulated wind speeds. The right axis (orange) denotes the power potential. The whole red-orange line denotes the power potential corresponding to the ons-site wind. The dashed red-orange line denotes the power potential corresponding to the WRF-simulated wind speed. Note that June is not part of the distribution.
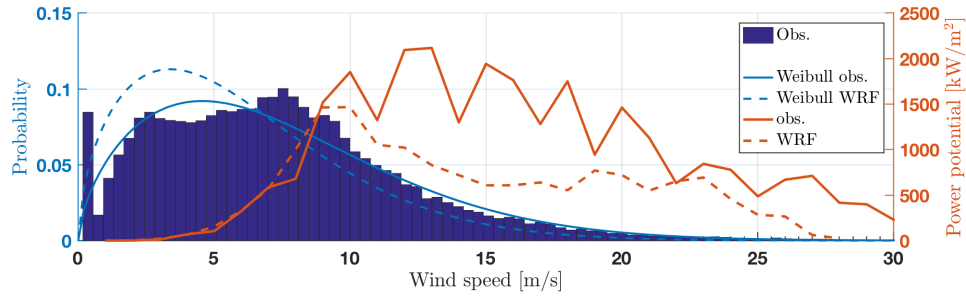
Figure 5.18: Normalized histogram for on-site observations, fitted Weibull pdf, and power potential from on-site measurements and WRF for 2014.

The histograms from on-site and WRF are sorted into unique wind speeds and each measurement and simulation at that wind speed is counted. The accumulated power density is the number of measurements multiplied by the power that the wind speed corresponds to. The total wind power can be expressed as

$$\tilde{P}_{tot} = \sum_{i=1}^{N} n_i \tilde{P}_i \tag{5.3.6}$$

where N is the number of unique wind speeds, n_i is the number of measurements at that unique wind speed and $\tilde{P}_i$ is the power density.

The accumulated power potential is tabulated in Tab. 5.5. As shown in Fig. 5.17, the WRF model systematically underestimates the power potential in all quarterlies. This has a large impact on the total accumulated power potential for 2014.

**Table 5.5:** Power potential corresponding to the power curves in Fig. 5.17.

	Power potential	
	On-site	**WRF, do3**
January to March	12.14 MW/m^2	6.67 MW/m^2
April to May	4.95 MW/m^2	4.42 MW/m^2
July to September	4.26 MW/m^2	1.86 MW/m^2
October to December	8.32 MW/m^2	3.35 MW/m^2
Total for 2014	29.67 MW/m^2	16.30 MW/m^2

As noted in Chapter 2, the Betz' limit gives that a ideal wind turbine can harvest 16/27 of the entries in Tab. 5.5. This implies that the power potential estimates from on-site measurements from an ideal wind turbine will give 17,58 MW/m^2 annually, and the WRF-estimated potential power for the same ideal turbine will give approximately 9,66 MW/m^2 at the wind distribution seen in 2014.

5.3.4   High winds

As discussed in the previous section, WRF generally underestimates high wind speeds for the months investigated.

Detecting and simulating strong winds is necessary for almost all above-ground structures like masts, tall bridges and wind turbines. In their case-study of the wind park at Nygårdsfjellet, Bilal et al. [5] stated that approximately 87% of the rated power for installed turbines occur at wind speeds of 12 m/s and above.

Wind speed of 12 m/s and above will be referred to as high wind and when it occurs it will be referred to as a high wind event, abbreviated HWE.

High wind events lasting longer than 15 hours are given in Tab. 5.6. The wind speeds are hourly averages.

Table 5.6: Table of the 15 most significant high wind events in 2014. The measurements are taken at site 2503. The wind speed and direction is measured at 49.1 m and 42.1 meters a.g.l.

No.	Start date [dd.mm.yyyy]	Duration [hours]	Mean wind speed [m/s]	Mean direction [degrees]
1	27.01.2014	15	14.9	150.4
2	10.02.2014	21	18.2	160.4
3	21.02.2014	17	13.9	161.9
4	08.03.2014	18	20.6	272.8
5	12.03.2014	19	18.9	281.3
6	26.03.2014	15	17.2	300.3
7	01.04.2014	17	15.7	286.8
8	14.04.2014	20	14.1	291.8
9	23.04.2014	21	14.8	281.4
10	13.09.2014	28	16.6	283.6
11	21.10.2014	46	14.7	153.7
12	23.10.2014	22.5	14.6	157.8
13	07.11.2014	29	14.1	148.8
14	25.12.2014	17	14.5	239.5
15	30.12.2014	28	18.0	230.0

Table 5.6 shows that the majority of the high winds are from WNW and SSE. This indicates that winds at high speeds follow the Skibotn valley. There are also two high wind events from SW. Using the largest WRF domain for investigating the meteorological conditions in the northern part of Norway at these events (HWE14 and HWE15) reveal that there are strong low pressure regimes in the Norwegian sea travelling north along the Norwegian coast at both events. As

the typical local wind flow pattern is rectified by the terrain surrounding Rieppi,
the strong low pressure regimes at HWE14 and HWE15 lead unusual strong
winds that do not follow the terrain as much as is common for this area.

None of the high wind events occurred in the time period May to August.
Because of the lacking measurements from mast 2503 for June, the WAS mast
is used for investigating the wind speeds in June. The WAS measurements
corroborates that there are no high wind events in June. Table 5.6 indicates
that the majority of the high wind events occur at winter time.

5.3.5   Local wind resource maps

High wind events are used for investigating the local wind resource maps.
As these scenarios are most interesting from the viewpoint of potential wind
power, (discussed in section 5.3.4) and turbulent kinetic energy.

The area of interest
for the local wind re-
source maps is the
mountain ridges and
the valley closest to
the Rieppi site. This
area is chosen for in-
vestigating how the
wind behaves upon
encountering the sur-
rounding mountains
and the valley. Fig-
ure 5.19 shows the
Rieppi site with mast
2503 marked with a
red dot.
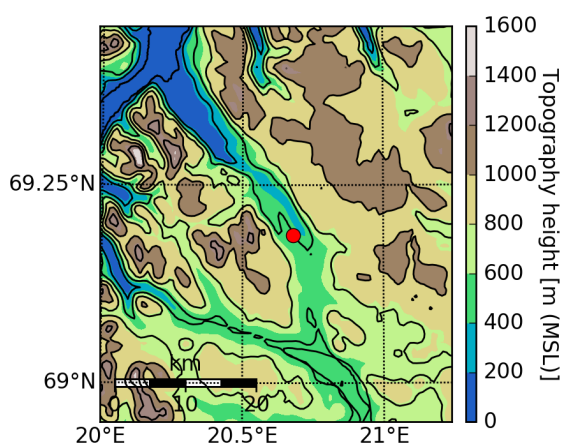
Figure 5.19: The topography surrounding Rieppi.

The wind maps are re-
trieved at times where the mast 2503 shows high winds from the most dominant
directions. As pointed out in section 5.1, the prevailing wind directions are
wind from SSE and NNW, through the valley.

Figure 5.20 shows snapshots from the high wind events HWE4 (Fig. 5.20a),
HWE5 (Fig. 5.20b) and HWE13 (Fig. 5.20c). December 10 is chosen for rep-
resenting scenarios with high winds coming from a typical angle, i.e. from
SSE (Figure 5.20d). The horizontal dashed lines represents one quarter of a
latitude. The longitudes are plotted every half degree. The map projection is

Transversal Mercator.

The figure shows WRF simulations for domain 3 with horizontal wind at 60 meters a.g.l. as a contour-surface with wind barbs. The wind barbs shows direction and speed. The wind speed corresponding to the wind barbs can be examined in Appendix H: *Beuforts wind force scale*. As seen by the predominant measured wind directions from mast 2503, Fig. 5.4 and from the WAS climatology plotted in Fig. 5.7, wind from NE is very rare and wind fields from this direction are not plotted. It is important to notice that the colormaps are set dynamically, so that one color does not necessarily represent the same value in two different figures.
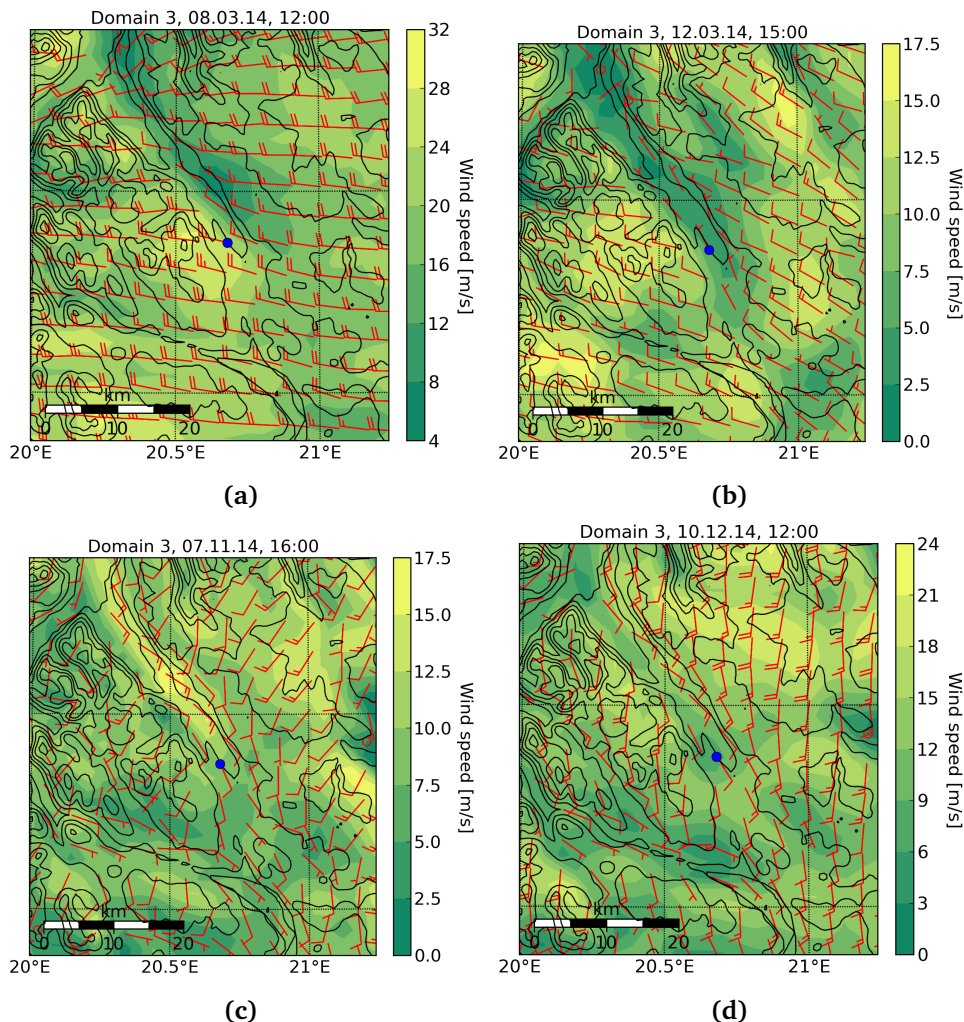
Figure 5.20: Local wind resource map over the surroundings at Rieppi. Note that the contour surfaces are set dynamically for each scenario.

Figure 5.20 indicates that there is no significant tunnelling effect at wind directions at SE and SSE when the wind direction is parallel to the valley.

Figure 5.21 shows the vertical wind fields as contour surfaces at the same time as Fig. 5.20. Wind barbs indicate the horizontal wind. The wind barbs are plotted more coarse than the other figures to visualize the horizontal wind direction, but not making Fig. 5.21 too busy. Mast 2503 is the blue dot.

Figure 5.21: Vertical wind fields as contour-surface with horizontal wind barbs over Rieppi.

The investigation of vertical winds is interesting for the potential wind park site as a wind park should be located where there is little vertical winds. A typical 3 MW wind turbine may have a rotor diameter of approximately 100 meters, a tower from 60 to 100 meters and a nacelle weight often exceeding

100 tonnes [73]. Because torque is the cross product of arm and force, the long tower and large thrust force exerted on the rotor by the wind will lead to a large torque on the turbine.

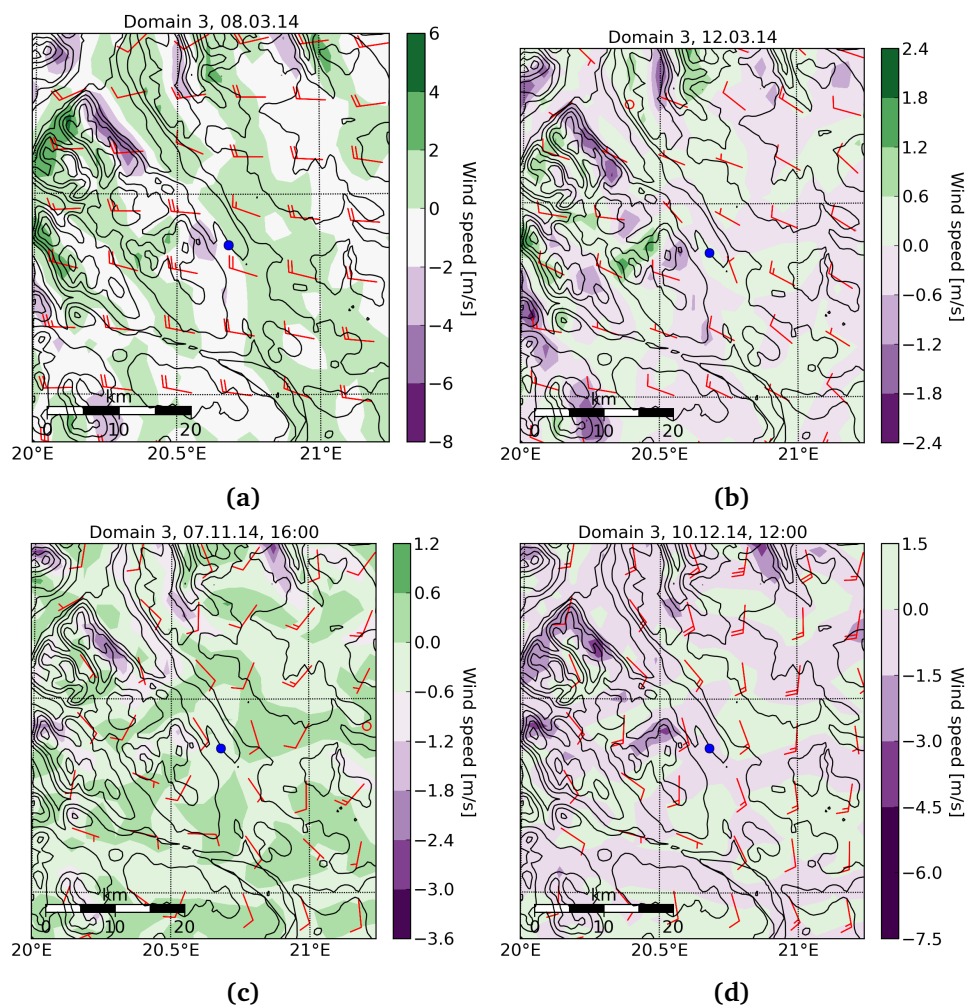As Rieppi is located in a valley with mountain surrounding the site and not on a flat ground, there will clearly always be some vertical movement in the wind due the surface wind that follows the terrain.

5.3.6   Turbulent kinetic energy

For minimizing material fatigue of the wind turbines and for stable operation conditions, the location of a potential wind park should be chosen where there are minimal turbulence. This section aims at investigating the scenarios at certain high wind events.

The high wind event with the highest mean wind speed is HWE4. At October 8, 15:00 mast 2503 recorded a wind speed of 32.67 m/s. This is a rare wind speed at the Rieppi site as only ~0.1% of all measured wind speeds exceed 30 m/s Here. According to the Beauforts wind force scale (Appendix H), 30 m/s is in the violent storm to hurricane category. An overview of the turbulent kinetic energy (TKE) of October 8 is simulated using WRF, domain 3, and plotted in Fig. 5.22a. The Rieppi site is marked with a green dot.

As a first comment, one can observe that the simulated wind speeds are around 15 m/s, i.e. under half the recorded wind speed. Three other scenarios of recorded wind speeds are also simulated using WRF and plotted in Fig. 5.22b - 5.22d. The TKE surface shows that the entire valley around the site will be turbulent for wind from certain directions. The wind speed used for the turbulence maps are simulated by WRF and are not as high as the wind speeds recorded at mast 2503 and one can therefore assume that the turbulence will be more severe in real scenarios.

Figure 5.22a indicates that the whole Skibotn valley will be turbulent at wind from WNW. It is not easy to conclude whether or not the location of the Rieppi site is optimal based on the scenarios depicted in Fig. 5.22b - 5.22d. Figure 5.22d indicates that the TKE is higher surrounding the Rieppi site than *at* the site. To elaborate on the best suited location of the Rieppi site, one should extract the TKE for the area for a whole year and make a TKE map over the mean turbulence in the area.
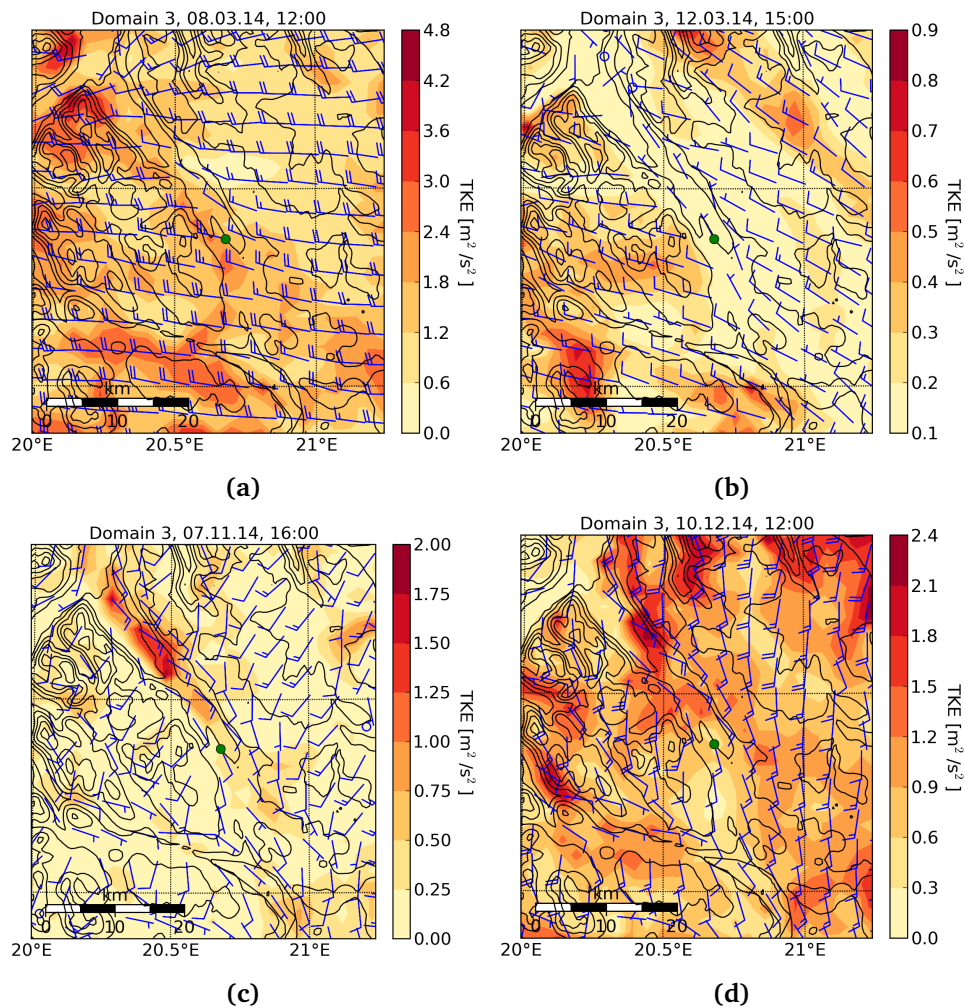
Figure 5.22: WRF simulation showing turbulent kinetic energy (TKE) over Rieppi with scenarios of high winds from different directions.

5.3.7 Wind fields at different height levels

As seen in Fig. 3.1b and Fig. 5.19, the topography surrounding the Rieppi site is mountainous with the highest nearby mountains at approximately 1400 meters above mean sea level (MSL).

At the December 10, there was a low pressure regime centred in the north sea travelling north. Figure 5.23 shows the horizontal wind field at approximately 10, 80, 450 and 1000 meters a.g.l. in Fig. 5.23a- 5.23d, respectively. The reason for this choice of height levels is that one would assume that the wind speed increases with the altitude and that the wind fields at higher altitudes are more

stable than the ground-surface wind fields. At approximately 450 meters a.g.l., the height of the wind field is approximately 1000 meters above mean sea level (MSL) which is slightly lower than some of the surrounding mountains in the surrounding area and one could expect the wind fields to be slightly deflected by the tallest mountains and mountain ridges. At approximately 1000 meters a.g.l. the wind field is above all the surrounding mountains.

(a) Wind speed at 10 m a.g.l.

(b) Wind speed at ~80 m a.g.l.

(c) Wind speed at ~450 m a.g.l.

(d) Wind speed at ~1000 m a.g.l.
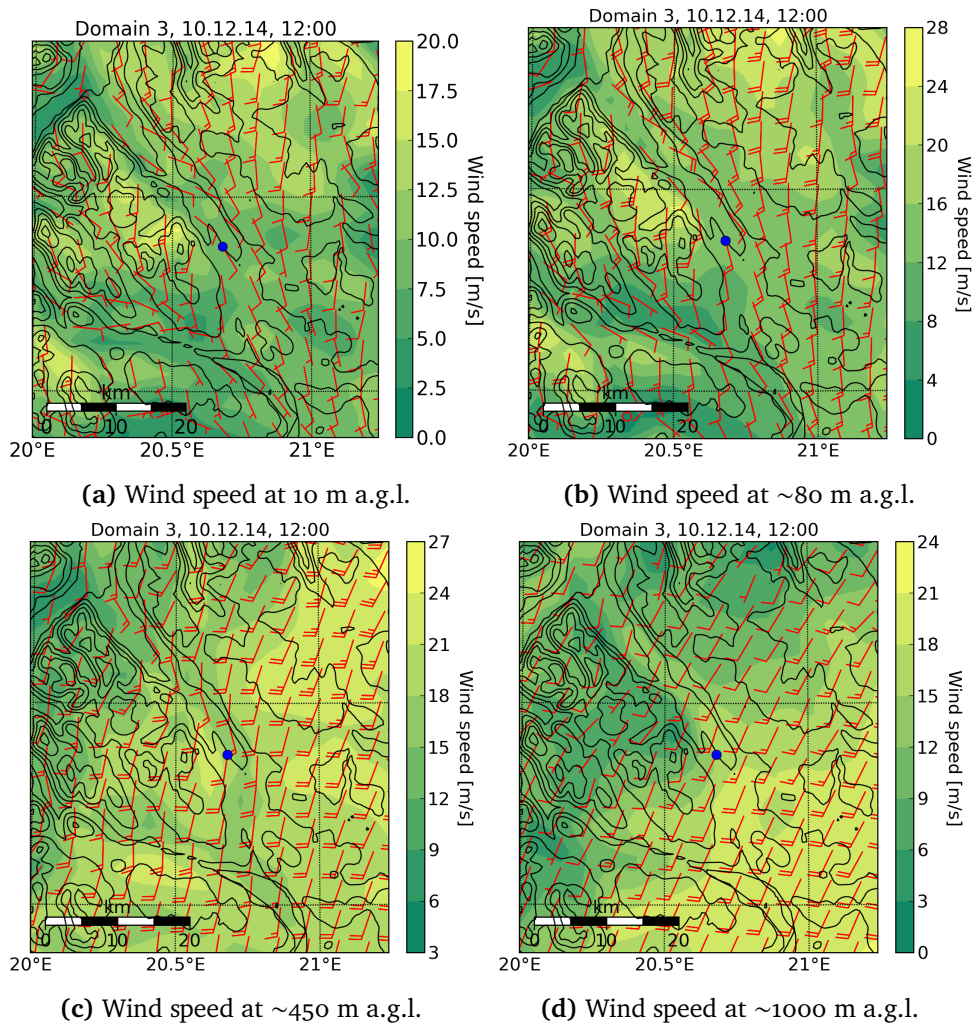
Figure 5.23: Map over wind fields at different heights. Note that the scales of the colormaps are not the same in the four figures.

From Fig. 5.23 it is clear that the wind field at 10 meters is following the terrain. At approximately 80 meters a.g.l. the wind is increasing, as discussed above and the flow regime is similar to that at 10 meter. At approximately 450 meters above mast 2503, the wind field is slightly deflected by the tallest mountains

as seen in Fig. 5.23c. Figure 5.23c shows that the wind speed increases towards the SE. Figure 5.23d shows a rectifying of the wind where the wind direction does not seem to be deflected by the underlaying terrain. The wind speed also increases towards the SE.

/ 6

Conclusion and further work

6.1 Wind simulation summary

This section will briefly outline the key aspects of the wind resources at Rieppi based on the available data from the three sources, on-site observations, ERA-Interim reanalysis data and WRF simulations along with some remarks on the performance of ERA-Interim data and WRF simulation results.

The on-site measurements from mast 2503 showed very little extreme winds throughout 2014 with only 0,5% of all recorded wind speeds exceeding 25 m/s and 0,1% exceeding 30 m/s.

In summary, the results retrieved from ERA-Interim showed little agreement to the wind speed with an overall correlation coefficient of 0.413 to the on-site observations. The wind direction and temperature at 2 meters a.g.l. showed better agreement, as tabulated in Chapter 5, Tab. 5.9. All three domains of the WRF model performed better at wind speed, wind direction and the 2 meter temperature than the reanalysis data. This is not surprising as the temporal and spatial resolution of the ERA-data is coarser. Judging from the wind rose comparisons in Fig. 5.14, ERA-Interim is not able to reproduce the prevailing wind directions as seen by the on-site measurements.

The wind directions from the on-site measurements and WRF simulations from domain 3 show that the prevailing wind directions are parallel to the Skibotn valley. Troms Kraft's suggestion of the placement of the wind turbines, illustrated in Chapter 3, Fig. 3.2a, might not be a good idea due to the wake effects discussed in Chapter 2.

When comparing the RMSE, correlation and Bias of the on-site temperature, wind speed and wind direction agains the WRF simulations, it is not clear which simulation domain that provides the most accurate results. The highest resolution domain, i.e. domain 3, provides the highest wind speed correlation to the on-site wind speed. Domain 2 is provides the highest correlation coefficient for the wind direction, and domain 2 and 3 give equally high correlation coefficients for the temperature.

The monthly means and standard deviations indicates that both ERA-Interim data and the all WRF domains tends to underestimate the on-site wind speeds. This is affirmed by the the negative Biases.

When looking at the wind field resolution from the three domains in Fig. 5.15, it is clear that domain 3 is better at capturing more high resolution spatial phenomena like local wind directions, wind deflections by terrain, and more rapid changes in wind speed. This is reflected by the wind rose comparisons in Fig. 5.16 where domain 3 show good agreement to the on-site measurements and Domain 1 and 2 both have larger spread. Figure 5.15 demonstrates that even if the wind speed and direction is approximately the same in all domains, the domain resolutions is important for representing a field, for example wind, temperature or TKE at a given site.

The underestimation of the wind speed might originate from the smoothened model terrain not having high enough resolution to represent the small ridge the mast 2503 is on. In a sensitivity study of the WRF model, Carvalho et al. [11] stated that the WRF simulation results were poorer in sites with higher terrain complexity. They argues that the increase of domain resolution alone is not sufficient for significantly improving the model performance. This points towards another factor that might lead to the underrepresentation of the wind speeds, namely the ERA-Interim input data. The mean wind speed from ERA-Interim of 4,3 m/s is over 40 % lower than the on-site mean wind speed of 7,5 m/s, according to Tab. 5.4. If the input data were closer to the observational data, one could have tried using grid nudging, as discussed in Chapter 4, subsection 4.2.4 for improving the simulations. The grid nudging "relaxes" the simulation data towards the input data. A third factor that might be the cause, or a contributing factor of the wind speed underrepresentation is the WRF configurations. Although there are many sensitivity studies on the different parameterizations schemes in the WRF model, there are not many studies that

investigates different WRF parameterization schemes in similar climate and terrain as the Rieppi site.

6.2 Concluding remarks

The wind resources at Rieppi has been investigated by the use of two on-site measurement masts, ERA-Interim reanalysis data from the ECMWF and simulation results from the WRF model. The study is based on the year 2014, but a climatology for wind speeds in the period 2004-2013 is also made. The climatology shows that the mean wind speed from 2014 is approximately 3,4 % below the climatology mean. The reanalysis data and the on-site observations did not provide a good correlation for the wind speed, and investigating the wind roses showed that the ERA-Interim data was not able to represent the same prevailing wind directions as the observational measurements.

The WRF model gave better overall correlation to the observations than the ERA-Interim data. However, all the simulation domains seems to underestimate high wind speeds. Whether this is due to a smoothened simulation terrain that does not capture the narrow ridge the measurement mast is on, the WRF parameterization setup, or due to the ERA-Interim input data is not known.

The highest resolution domain shows a good agreement to the wind directions from the measurement mast. The detailed wind maps from the highest resolution simulation domain demonstrated that the WRF model with this setup is an important tool for investigating early stage phase of wind farm projects. However, because of the underrepresentation of wind speed, the WRF model alone is not sufficient for providing a stand-alone wind resource assessment tool.

The WRF simulation shows that the location of the potential wind park is at a location where there are minimal vertical winds and turbulent kinetic energy in relation to other part of the valley and the nearby surroundings.

6.3 Future work

There are several interesting and important extensions for improving the accuracy of the WRF model and subsequently improving the knowledge of the the wind resource at Rieppi and similar sites. Some improvements are listed below.

- Because the WRF model seemingly underestimates high wind speeds, a sensitivity study of which planetary boundary layer (PBL) parameterization schemes provides the most realistic results should be carried out. Perhaps a new parameterization scheme for the PBL should be made to fit the arctic conditions and complex terrain similar to Rieppi. The model setup can be extended to sites with similar terrain, latitude and atmospheric conditions.

- As the ERA-Interim data are temporally and spatially coarse, a possible improvement is to use complementary input data sources like on-site observations, weather stations and satellites. The complementary data can be assimilated to the ERA-Interim data.

- The WRF setup can be tested at different locations for assessing the WRF setup performance at similar locations.

- Use WRF simulations for investigating regional wind patterns between the wind parks at Nygårdsfjellet (at Narvik, Nordland county) and Fakken (at Vannøya, Troms county) and Rieppi. Identifying the wind pattern could be valuable for predicting extreme weather and subsequently preventing the wind parks from damage.

- Use the WRF model for short-term wind predictions.

- Combine the WRF model with a microscale model like WAsP [20], COMSOL Multiphysics [15] and WindSim [79] for a more detailed analysis of e.g. the optimal location of wind turbines, detailed turbulence studies, and other applications that demands very high resolution.

In additions to possible improvements for wind resource mapping, there are some very interesting applications that can be investigated using the WRF model. Some of these applications are listed below.

- According to the Norwegian Geotechnical Institute (NGI), there has been 69 deaths related to snow avalanches the last ten years [54]. As a telemark skier, I see the utility of improving the avalanche forecasting and to increase the knowledge about the local avalanche risks. The WRF model one can estimate e.g. precipitation, temperature and wind speed history. By combining the WRF simulations for historical snow and weather conditions, on-site observations, drones and satellites together with high resolution WRF forecasts, one could improve the avalanche forecasting system which today is done at a regional scale.

- The WRF model can be used for extracting precipitation, cloud cover

mixing ratio, albedo and wind speed for investigating potential sites for hybrid systems. This is illustrated in Appendix J: *Additional figures*, where Fig. J.1a depicts the cloud mixing ratio at the Rieppi site for March 10. One could run a simulation for a year and plot the mean cloud cover over a potential area for investigating the amount of direct and diffuse solar irradiation on solar panels. Figure J.1b shows the surface albedo for November 2. For investigating how tall the solar panels have to be mounted and not being covered in snow, the snow depth could be of interest. The snow depth at March 10 is depicted in Fig. J.2a.

- The WRF model can be used for estimating the existing snow volume. Together with short-term forecasts of surface temperature and precipitation, the WRF model can be used for estimating flooding, especially for the snow melting in the spring. Figure J.2a show the snow depth for March 10. Figure J.2b depicts the temperature field at 2 meters a.g.l. at March 10.

- The WRF model can be used for for predicting dispersion of air for estimating spread of e.g. airborne diseases or the dispersion of radioactive effluents.

Appendices

Appendix A: Coriolis force and the coriolis parameter

This appendix is dedicated to the derivation of the coriolis force and the coriolis parameter.

A vector $\boldsymbol{r}$ that changes in a inertial frame due to rotation can generally be expressed

$$(\delta\boldsymbol{r})_I = (\delta\boldsymbol{r})_R + (\delta\boldsymbol{r})_{rot}, \tag{A.1}$$

where $(\delta\boldsymbol{r})_R$ denotes change of $\boldsymbol{r}$ measured in the rotating frame and $(\delta\boldsymbol{r})_{rot}$ is the change due to rotation. The change of the vector $\boldsymbol{r}$ with time gives

$$\left(\frac{\mathrm{d}\boldsymbol{r}}{\mathrm{d}t}\right)_I = \left(\frac{\mathrm{d}\boldsymbol{r}}{\mathrm{d}t}\right)_R + \Omega \times \boldsymbol{r} \tag{A.2}$$

$$\boldsymbol{v}_I = \boldsymbol{v}_R + \Omega \times \boldsymbol{r}, \tag{A.3}$$

where $\boldsymbol{v}_I$ and $\boldsymbol{v}_R$ are velocities seen from the initial and rotating reference frame respectively. Ω is the angular velocity. Equation A.2 is valid for any vector. By applying $\boldsymbol{v}_R$ to Equation A.2 and assuming that Ω is constant, Equation A.3 can be rewritten as

$$\left(\frac{\mathrm{d}\boldsymbol{v}_R}{\mathrm{d}t}\right)_R = \left(\frac{\mathrm{d}\boldsymbol{v}_I}{\mathrm{d}t}\right)_I - 2\Omega \times \boldsymbol{v}_R - \Omega \times (\Omega \times \boldsymbol{r}), \tag{A.4}$$

where the left hand term is the rate of change of the relative velocity as measured in the rotating frame. The first term on the right hand side is the rate of change of the initial velocity as measured in the inertial frame. The second and third term on the r.h.s. are the *Coriolis force* and the *Centrifugal force* which are not conventional forces, but rather "quasi-forces", meaning that a body in the rotating frame behaves as if these forces were acting on it.

The Coriolis force does no work because it is perpendicular to a body's velocity.

Decomposing the rotation vector gives

$$\Omega = \begin{cases} \Omega^x = 0, & (\Omega^x \text{ is perpendicular to } \Omega) \\ \Omega^y = \Omega \cos \vartheta \\ \Omega^z = \Omega \sin \vartheta, \end{cases}$$

where ϑ is the latitude. x, y and z denotes east-west, south-north and the altitude respectively.

In geophysical fluid mechanics, the vertical component, i.e. the z-component of the rotation vector is often the most important [72]. This leads to the definition of the Coriolis parameter, namely

$$f \equiv 2\Omega \sin \vartheta.$$

Appendix B: Physical constants

The physical constants used in this thesis are the same as used in the WRF model. The constants are from *A Description of the Advanced Research WRF Version 3* by Skamarock et al. [63].

Table B.1: List of physical constants used in the calculations in the thesis.

Symbol		Value and unit	Description
$c_{p,d}$	=	$7 \cdot R_v / 2$ Jkg^{-1}K^{-1}	Specific heat capacity for dry air at constant pressure
$c_{p,w}$	=	$4 \cdot R_w$ Jkg^{-1}K^{-1}	Specific heat capacity for water vapour at constant pressure
g_0	=	9.81 m s^{-2}	Acceleration due to gravity
k	=	5.67051×10^{-8} Wm^{-2}K^{-4}	Stefan-Boltzmann's constant
r	=	6.370×10^6 m	Radius of earth
R_d	=	287 J kg^{-1} K^{-1}	Gas constant for dry air
R_w	=	461.6 J kg^{-1} K^{-1}	Gas constant for water wapor

Appendix C: Atmospheric thermodynamics

The fundamental thermodynamic relation

Conservation of energy states that a change of internal energy in a body is due to heat exchange, work done on or of the body and/or change in the body's chemical composition. This is the *fundamental thermodynamic relation*, also referred to as *the first law of thermodynamics* and can be expressed

$$\mathrm{d}I = \mathrm{d}Q - \mathrm{d}W + \mathrm{d}C. \tag{C.1}$$

The heat input *to* the body is related to the temperature and the change in entropy in the body, namely $\mathrm{d}Q = T\mathrm{d}\eta$.

The work done *by* the body is the pressure times the change of the body's volume, namely $\mathrm{d}W = p\mathrm{d}\alpha$, where α is the specific volume of the body.

The change in internal energy due to a change of the body's composition is due to the *chemical potential* ϱ times the composition S, namely $\mathrm{d}C = \varrho\mathrm{d}S$.

Using these relations, the fundamental thermodynamic relation can be reformulated to

$$\mathrm{d}I = T\mathrm{d}\eta - p\mathrm{d}\alpha + \varrho\mathrm{d}S. \tag{C.2}$$

Enthalpy

Another way of expressing a systems energy is by using *enthalpy*. A change in enthalpy considers both the changes of the system and the energy transfer to the environment. Enthalpy is defined as

$$h \equiv I + p\alpha, \tag{C.3}$$

and using the thermodynamic relation, a small change in enthalpy can be expressed

$$\mathrm{d}h = T\mathrm{d}\eta + \alpha\mathrm{d}p. \tag{C.4}$$

Heat capacity and the gas constant

By using the expression for enthalpy and assuming that enthalpy is a function of only pressure and temperature, the thermodynamic relation can be reformulated as

$$T\mathrm{d}\eta = \left(\frac{\mathrm{d}h}{\mathrm{d}p}\right)_T \mathrm{d}p + \left(\frac{\mathrm{d}h}{\mathrm{d}T}\right)_p \mathrm{d}T - \alpha\mathrm{d}p. \tag{C.5}$$

Using Eq. C.5 at constant pressure gives the definition of the heat capacity at constant pressure

$$c_p \equiv T\left(\frac{\partial\eta}{\partial T}\right)_p = \left(\frac{\partial h}{\partial T}\right)_p. \tag{C.6}$$

In a similar manner, by assuming that the internal energy is a function of volume and temperature alone, the thermodynamic relation can be reformulated as

$$T\mathrm{d}\eta = \left(\frac{\partial I}{\partial T}\right)_\alpha \mathrm{d}T + \left(\frac{\partial I}{\partial \alpha}\right)_T \mathrm{d}\alpha + p\mathrm{d}\alpha. \tag{C.7}$$

At constant volume, the definition of heat capacity at constant volume is

$$c_v \equiv T\left(\frac{\partial\eta}{\partial T}\right)_\alpha = \left(\frac{\partial I}{\partial T}\right)_\alpha. \tag{C.8}$$

Appendix D: Derivation of directional variance

The two-dimensional covariance matrix can be expressed by

$$\Sigma_{xy} = \begin{bmatrix} \sigma_{xx} & \sigma_{xy} \\ \sigma_{yx} & \sigma_{yy} \end{bmatrix},$$

where $\sigma_{xx} = (1/n) \sum_{i=1}^{n} (\sin \alpha_i - \sin \overline{\alpha_0})^2$ and $\sigma_{yy} = 1/n \sum_{i=1}^{n} (\cos \alpha_i - \cos \overline{\alpha_0})^2$. $\overline{\alpha_0}$ is the angle of the resultant vector $\boldsymbol{R} = \sqrt{C^2 + S^2}$ [43]. The total sample variance is the trace of the covariance matrix [39];

$$
\begin{aligned}
s^2 &= \mathrm{Tr}(\Sigma_{xy}) \\
&= \frac{1}{n} \left(\sum_{i=1}^{n} \left(\sin \alpha_i - \sin \overline{\alpha_0} \right)^2 + \sum_{i=1}^{n} \left(\cos \alpha_i - \cos \overline{\alpha_0} \right)^2 \right) \\
&= \frac{1}{n} \left(\sum_i \sin^2 \alpha_i - 2 \sum_i \sin \alpha_i \sin \overline{\alpha_0} + \sum_i \sin^2 \overline{\alpha_0} \right. \\
&\qquad \left. + \sum_i \cos^2 \alpha_i - 2 \sum_i \cos \alpha_i \cos \overline{\alpha_0} + \sum_i \cos^2 \overline{\alpha_0} \right) \\
&= \frac{1}{n} \left(2n - 2 \left(\sum_i \sin \alpha_i \sin \overline{\alpha_0} + \sum_i \cos \alpha_i \cos \overline{\alpha_0} \right) \right),
\end{aligned}
$$

where the trigonometric identity is used. By noting that the components of the resultant vector can be expressed as

$$
C = \begin{cases} \frac{1}{n} \sum_i \cos \alpha_i \\ SR \cos \overline{\alpha_0} \end{cases}, \qquad \text{and} \qquad S = \begin{cases} \frac{1}{n} \sum_i \sin \alpha_i \\ R \sin \overline{\alpha_0} \end{cases}.
$$

Using these relations, the sample variance can be rewritten as

$$
\begin{aligned}
s^2 &= 2 - \frac{2}{n} \left(Cn \cos \overline{\alpha_0} + Cn \sin \overline{\alpha_0} \right) \\
&= 2 - 2 \left(R \cos^2 \overline{\alpha_0} + R \sin^2 \overline{\alpha_0} \right) \\
&= 2(1 - R).
\end{aligned}
$$

Appendix E: Namelists

As the namelists in the WRF model is where the simulation time and all configurations like domains, physics, boundary condition controls etc. are set, the most used WRF configurations in this study is exemplified in the appended *namelist.wps* and *namelist.input*. The function of the two namelists are discussed in Chapter 4, section 4.1.

namelist.wps

```
&share
 wrf_core = 'ARW',
 max_dom = 3,
 start_date = '2014-02-28_00:00:00',...
 '2014-02-28_00:00:00','2014-02-28_00:00:00',
 end_date  = '2014-04-01_00:00:00',...
 '2014-04-01_00:00:00','2014-04-01_00:00:00',
 interval_seconds = 21600
 io_form_geogrid = 2,
/

&geogrid
 parent_id        =   1,   1, 2,
 parent_grid_ratio = 1,   3, 3,
 i_parent_start   =   1,  25, 30,
 j_parent_start   =   1,  25, 30,
 e_we             = 100, 151, 301,
 e_sn             = 100, 151, 301,
 geog_data_res    = '2m','30s','30s',
 dx = 18000,
 dy = 18000,
 map_proj = 'polar',
 ref_lat  = 69.1867,
 ref_lon  = 20.6804,
 truelat1 = 60.0,
 stand_lon = 18.0,
 geog_data_path = '/home/WRF/WPS_GEOG/'
/
```

```
&ungrib
 out_format = 'WPS',
 prefix = 'Rieppi_Mar',
/

&metgrid
 fg_name = 'Rieppi_Mar'
 io_form_metgrid = 2,
/
```

namelist.input

```
&time_control
 run_days                   = 32,
 run_hours                  = 00,
 run_minutes                = 0,
 run_seconds                = 0,
 start_year                 = 2014, 2014, 2014,
 start_month                = 02,   02,   02,
 start_day                  = 28,   28,   28,
 start_hour                 = 00,   00,   00,
 start_minute               = 00,   00,   00,
 start_second               = 00,   00,   00,
 end_year                   = 2014, 2014, 2014,
 end_month                  = 04,   04,   04,
 end_day                    = 01,   01,   01,
 end_hour                   = 00,   00,   00,
 end_minute                 = 00,   00,   00,
 end_second                 = 00,   00,   00,
 interval_seconds           = 21600
 input_from_file            = .true.,.true.,.true.,
 history_interval           = 10, 10,   10,
 frames_per_outfile         = 144, 144, 144,
 restart                    = .false.,
 restart_interval           = 500000,
 io_form_history            = 2
 io_form_restart            = 2
 io_form_input              = 2
 io_form_boundary           = 2
 debug_level                = 0
/

&domains
 time_step                  = 90,
 time_step_fract_num        = 0,
 time_step_fract_den        = 1,
```

```
max_dom                         = 3,
e_we                            = 100,    151,   301,
e_sn                            = 100,    151,   301,
e_vert                          = 51,   51,   51,
p_top_requested                 = 1000,
num_metgrid_levels              = 38,
num_metgrid_soil_levels         = 4,
dx                              = 18000, 6000, 2000,
dy                              = 18000, 6000, 2000,
grid_id                         = 1,     2,     3,
parent_id                       = 0,     1,     2,
i_parent_start                  = 1,     25,    30,
j_parent_start                  = 1,     25,    30,
parent_grid_ratio               = 1,     3,     3,
parent_time_step_ratio          = 1,     3,     3,
feedback                        = 1,
smooth_option                   = 0
eta_levels =  1.0000, 0.9980, 0.9955, 0.9925, 0.9890, 0.9850,
              0.9805, 0.9755, 0.9700, 0.9640, 0.9575, 0.9505,
              0.9430, 0.9350, 0.9265, 0.9170, 0.9060, 0.8930,
              0.8775, 0.8590, 0.8363, 0.8104, 0.7803, 0.7456,
              0.7059, 0.6615, 0.6126, 0.5594, 0.5041, 0.4479,
              0.3919, 0.3384, 0.2897, 0.2474, 0.2107, 0.1792,
              0.1523, 0.1293, 0.1093, 0.0917, 0.0763, 0.0629,
              0.0513, 0.0413, 0.0328, 0.0255, 0.0194, 0.0144,
              0.0104, 0.0071, 0.0000,
/

&physics
mp_physics                      = 4,     4,     4,
ra_lw_physics                   = 5,     5,     5,
ra_sw_physics                   = 5,     5,     5,
radt                            = 9,     3,     1,
sf_sfclay_physics               = 2,     2,     2,
sf_surface_physics              = 2,     2,     2,
bl_pbl_physics                  = 2,     2,     2,
bldt                            = 0,     0,     0,
cu_physics                      = 2,     0,     0,
cudt                            = 5,     5,     5,
isfflx                          = 1,
ifsnow                          = 1,
icloud                          = 1,
surface_input_source            = 1,
num_soil_layers                 = 4,
sf_urban_physics                = 2,     2,     2,
/

 &fdda
/
```

```
&dynamics
w_damping                  = 0,
diff_opt                   = 1,
km_opt                     = 4,
diff_6th_opt               = 0,     0,      0,
diff_6th_factor            = 0.12,  0.12,   0.12,
base_temp                  = 290.
damp_opt                   = 0,
zdamp                      = 5000., 5000., 5000.,
dampcoef                   = 0.2,   0.2,   0.2
khdif                      = 0,     0,      0,
kvdif                      = 0,     0,      0,
non_hydrostatic            = .true., .true., .true.,
moist_adv_opt              = 1,     1,      1,
scalar_adv_opt             = 1,     1,      1,
/

&bdy_control
spec_bdy_width             = 5,
spec_zone                  = 1,
relax_zone                 = 4,
specified                  = .true., .false.,.false.,
nested                     = .false., .true., .true.,
/

&grib2
/

&namelist_quilt
nio_tasks_per_group = 0,
nio_groups = 1,
/
```

Appendix F: Numerical Integration

A ordinary differential equation (ODE) can be written in the general form [25]

$$\frac{\mathrm{d}\boldsymbol{y}}{\mathrm{d}t} - \boldsymbol{f}(t, \boldsymbol{y}) = 0. \tag{F.1}$$

By integrating both, the solution of this equation can be written as

$$\boldsymbol{y}(t) = \boldsymbol{y}(t_0) + \int_{t_0}^{t} \boldsymbol{f}(\boldsymbol{y}(t))\mathrm{d}t. \tag{F.2}$$

A solution over a small interval t_{i+1} can be expressed as an initial time t_i plus a step size h, where h is a positive constant. The next step can be approximated by

$$\boldsymbol{y}_{i+1} = \boldsymbol{y}_i + \int_{t_i}^{t_{i+1}} \boldsymbol{f}(t, \boldsymbol{y}(t))\mathrm{d}t \tag{F.3}$$

$$\approx \boldsymbol{y}_i + h\boldsymbol{f}(t_i, \boldsymbol{y}(t_i)). \tag{F.4}$$

There are basically two classes of methods for obtaining numerical solution of an ordinary differential equation, *one-step methods* and *linear multistep methods* [70].

The so-called on-step methods only use the present solution y_n to find the approximation for the new solution y_{n+1}. Given the initial value $y(t_0) = y_0$, one-step methods can all be expressed as

$$\boldsymbol{y}_{i+1} = \boldsymbol{y}_i + h\Phi(t_i, \boldsymbol{y}_i), \qquad \text{where} \qquad i = 0, 1, ...n - 1, \tag{F.5}$$

and n is the total number of data points. The function Φ is a continuous function of its variables [70].

One of the most basic explicit numerical integration methods is the Euler's method. In this case the function is just

$$\Phi(t_i, y_i; h) = f(t_i, y_i), \tag{F.6}$$

and Eq. F.5 is the same as the approximation in Eq. F.4.

For improved accuracy, the *Leapfrog method* can be used. This method evaluates the present solution at the midpoint for the new time step, namely

$$t_{i+1} = \frac{1}{2} h \boldsymbol{y}_i. \tag{F.7}$$

After calculating the new time step, the next step of the solution can be approximated by Eq. F.5.

Like the Leapfrog method, Runge-Kutta methods at higher order aim at achieving higher accuracy than the Euler method. This is done by evaluating the present solution at intermediate points between the time steps. Runge-Kutta schemes of second or higher orders can be derivated from Taylor series.

The function Φ for 2nd order Runge-Kutta can be expressed

$$\Phi = \frac{1}{2}(k_1 + k_2), \tag{F.8}$$

where

$$k_1 = \boldsymbol{f}(t_i, \boldsymbol{y}_i)$$
$$k_2 = \boldsymbol{f}(t_i + h, y_i + hk_1).$$

The 2nd order Runge-Kutta method is also referred to as the *improved Euler method* or the *midpoint method* [57].

The Runge-Kutta 3rd order can also be expressed by Eq. F.5, where the function Φ becomes

$$\Phi = \frac{1}{6}(k_1 + 4k_2 + k_3), \tag{F.9}$$

where k is the evaluated functions

$$k_1 = f(x_i, y_i)$$
$$k_2 = f(x_i + 1/2h, y_i + 1/2k_1 h)$$
$$k_3 = f(x_{i+h}, y_i - k_1 h + 2k_2 h)$$

The time step is important for stability as a too large time step will make lead to an unstable solution. A too small time step is also undesired as it makes the computation more laborious.

Appendix G: Geostrophic balance

The 2-D Navier-Stokes equations can be expressed

$$\frac{\partial \boldsymbol{u}}{\partial t} + \underbrace{\left(\boldsymbol{v} \cdot \nabla\right)\boldsymbol{u}}_{\text{Advective term}} + \underbrace{\boldsymbol{f} \times \boldsymbol{u}}_{\text{Coriolis term}} = -\frac{1}{\rho}\nabla_z p, \tag{G.1}$$

similar to the derivation of Eq. 2.1.11 in Chapter 2.

The Rossby-number is defined as the ratio between the advective and the Coriolis term [72], namely

$$Ro \equiv \frac{U}{fL}, \tag{G.2}$$

where U is a typical scale for the horizontal velocity in the atmosphere, f is the Coriolis parameter and L is a typical horizontal length scale for the atmosphere.

If the rotation dominates the advection of the fluid, leading to a small Rossby number, and the motion scales advectively, meaning that the largest factor in the material derivative is due to advection, the horizontal, rotational Navier-Stokes equation can be approximated by

$$\boldsymbol{f} \times \boldsymbol{u} \approx -\frac{1}{\rho}\nabla_z p, \tag{G.3}$$

This is referred to as geostrophic balance for the horizontal flow. The subscript z of the del operator is used because this is a horizontal gradient and the height is therefore held constant. From Equation G.3 it is easy to see that if the Coriolis parameter is positive, i.e. on the northern hemisphere, then the geostrophic flow around a high pressure is clockwise (anti-cyclonic) and flow around low pressures are anti-clockwise (cyclonic). The Coriolis parameter on the southern hemisphere is negative, $f < 0$ leading to a opposite effect compared to the northern hemisphere.

The geostrophic velocity is defined as the cartesian components of Equation G.3, namely

$$f u_g \equiv -\frac{1}{\rho}\frac{\partial p}{\partial y} \qquad \text{and} \qquad f v_g \equiv \frac{1}{\rho}\frac{\partial p}{\partial x}. \qquad \text{(G.4)}$$
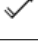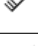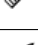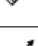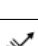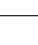
From Equation G.4 one can observe that the geostrophic flow is parallel to lines of constant pressure (isobars). One can say that geostrophic balance is the cause of geostrophic wind created by the pressure gradient force and deflected by the Coriolis force.

Because the flow is parallel to constant pressure, isobars will describe the flow's streamfunctions.

Appendix H: Beauforts wind force scale

The table is based on the british Met Office [47] and the Norwegian Meteorological institute [48].

Table H.1: The Beauforts wind force scale.

Force	Symbol	Wind speed [m/s]	Wind descriptive terms
0	○	0.0 - 0.2	Calm
1	↗	0.3 - 1.5	Light air
2	↗	1.6 - 3.3	Light breeze
3	↗	3.4 - 5.4	Gentle breeze
4	↗	5.5 - 7.9	Moderate breeze
5	↗	8.0 - 10.7	Fresh breeze
6	↗	10.8 - 13.8	Strong breeze
7	↗	13.9 - 17.1	Near gale
8	↗	17.2 - 20.7	Gale
9	↗	20.8 - 24.4	Strong gale
10	↗	24.5 - 28.4	Storm
11	↗	28.5 - 32.6	Violent storm
12	↗	32.6 <	Hurricane

Appendix I: Potential temperature

A common way of defining potential temperature is the temperature a fluid parcel would have if moved adiabatically and with constant composition to a reference pressure [72] .

Because the composition is constant, Eq. C.2 from Appendix C is reduced to

$$\mathrm{d}I = T\mathrm{d}\eta - p\mathrm{d}\alpha. \tag{I.1}$$

If the process is adiabatic, i.e. no heat enters or leaves the system, the entropy is constant. Solving Eq. C.6 with respect to the enthalpy and inserting this into Eq. I.1 gives

$$\alpha\mathrm{d}p = c_p\mathrm{d}T. \tag{I.2}$$

Dividing this equation by the equation of state Eq. 2.3.1 and integrating, I get

$$\frac{\mathrm{d}p}{p} = \frac{c_p\mathrm{d}T}{RT} \tag{I.3}$$

$$\int_{p_R}^{p} \mathrm{d}\log p = \frac{c_p}{R} \int_{T}^{\theta} \mathrm{d}\log T, \tag{I.4}$$

where p_R is the reference pressure and θ is the *potential temperature* which is just the fluid's temperature at the reference pressure. Solving with respect to the potential temperature yields

$$\theta = T\left(\frac{p_R}{p}\right)^{\kappa}, \tag{I.5}$$

where $\kappa \equiv R/c_p$. The reference pressure is usually the temperature at the surface. This implies that the potential temperature at the ground surface is the same as the temperature at the surface. The potential temperature in an adiabatic process is conserved.

Appendix J: Additional figures

The figures are illustrations to corroborate the suggestions for further work, Chapter 6.

The cloud cover mixing ratio could be simulated for period and averaged for obtaining a mean value for locating where there are maximal direct solar irradiation. The time for the averaging could be for example one year. The snow depth could be used for investigating the height the solar panels have to have for not being covered in snow during wintertime.
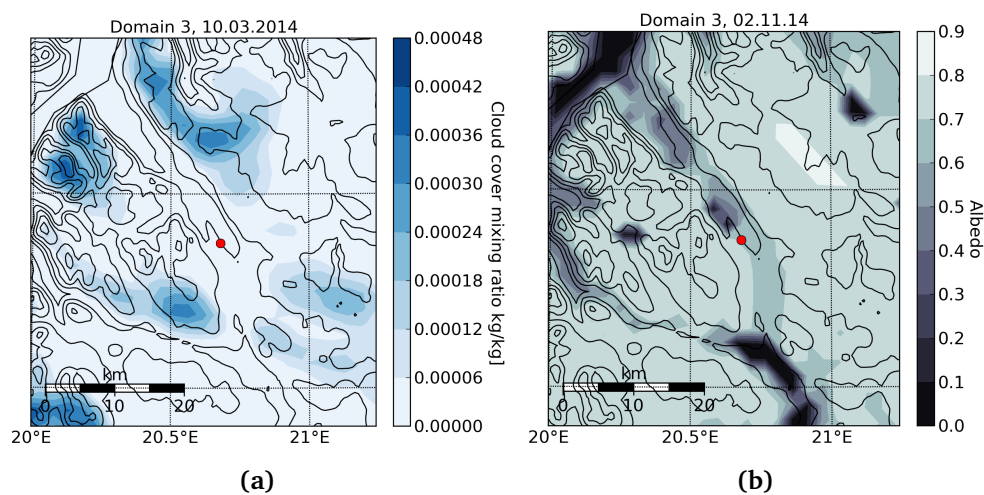

Figure J.1: a: Cloud cover mixing ratio for March 10. b: Surface albedo for November 2.

Figure J.2a show the snow depth on March 10. Together with the temperature at 2 meters a.g.l. in Fig. J.2b, and forecasting temperature and precipitation, it is possible to give a flooding forecast. This can improve the safety of inhabitants close to rivers and it might be useful for preventing eventual flooding.
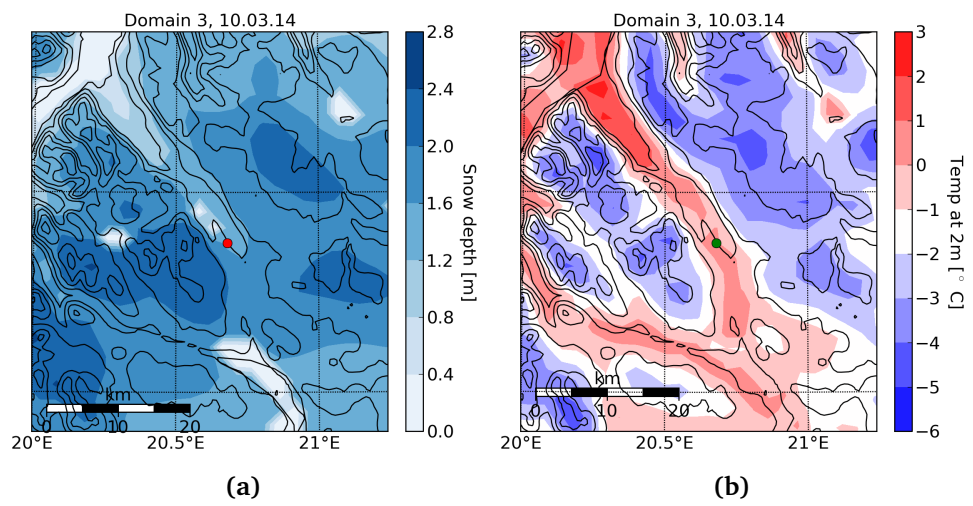
Figure J.2: a: Simulated snow depth for March 10. b: Temperature at 2 meters a.g.l. for March 10

Bibliography

[1] Malin Abrahamsen, Yngve Birkelund, et al. Coastal wind from satellite measurements and meteorological models for offshore wind power prediction. In *The Twenty-fifth International Offshore and Polar Engineering Conference*. International Society of Offshore and Polar Engineers, 2015.

[2] A Balzarini, F Angelini, L Ferrero, M Moscatelli, MG Perrone, G Pirovano, GM Riva, G Sangiorgi, AM Toppetti, GP Gobbi, et al. Sensitivity analysis of pbl schemes by comparing wrf model and experimental data. *Geoscientific Model Development Discussions*, 7(5):6133–6171, 2014.

[3] Philipp Berens et al. Circstat: a matlab toolbox for circular statistics. *J Stat Softw*, 31(10):1–21, 2009.

[4] L Bernardet, J Wolf, L Nance, A Loughe, B Weatherhead, E Gilleland, and B Brown. Comparison between wrf-arw and wrf-nmm objective forecast verification scores.

[5] Muhammad Bilal, Yngve Birkelund, and Matthew Homola. High winds at nygårdsfjell. *Journal of Clean Energy Technologies*, 3(2), 2015.

[6] Thomas L Black. The new nmc mesoscale eta model: Description and forecast examples. *Weather and forecasting*, 9(2):265–278, 1994.

[7] Philippe Bougeault and P Lacarrere. Parameterization of orography-induced turbulence in a mesobeta–scale model. *Monthly Weather Review*, 117(8):1872–1890, 1989.

[8] Godfrey Boyle. *Renewable energy*. OXFORD university press, 2004.

[9] BP. 2014 in review, 2014. URL http://www.bp.com/en/global/corporate/energy-economics/statistical-review-of-world-energy/2014-in-review.html.

[10] Øyvind Byrkjedal and Erik Berge. The use of wrf for wind resource

mapping in norway. In *9th WRF users' workshop*, 2008.

[11] David Carvalho, Alfredo Rocha, Moncho Gómez-Gesteira, and Carlos Santos. A sensitivity study of the wrf model in wind simulation for an area of high wind energy. *Environmental Modelling & Software*, 33:23–34, 2012.

[12] Yunus A Çengel, Víctor Cimbala, M John, et al. *Fluid mechanics fundamentals and applications.* Number TA357. C4318 2006. Mc Grav Hill, 3 edition, 2006.

[13] Ming-Dah Chou and Max J Suarez. A solar radiation parameterization for atmospheric studies. *NASA Tech. Memo*, 104606:40, 1999.

[14] Shih-Hung Chou. An example of vertical resolution impact on wrf-var analysis. *Electron J Oper Meteorol*, 12:1–20, 2011.

[15] COMSOL Inc. Comsol, May 2016. URL `https://www.comsol.com`.

[16] K Conradsen, LB Nielsen, and LP Prahm. Review of weibull statistics for estimation of wind speed distributions. *Journal of Climate and Applied Meteorology*, 23(8):1173–1183, 1984.

[17] DP Dee, SM Uppala, AJ Simmons, Paul Berrisford, P Poli, S Kobayashi, U Andrae, MA Balmaseda, G Balsamo, P Bauer, et al. The era-interim reanalysis: Configuration and performance of the data assimilation system. *Quarterly Journal of the Royal Meteorological Society*, 137(656):553–597, 2011.

[18] Adam J Deppe, William A Gallus Jr, and Eugene S Takle. A wrf ensemble for improved wind speed forecasts at turbine height. *Weather and Forecasting*, 28(1):212–228, 2013.

[19] R Dimitrova, Z Silver, HJS Fernando, L Leo, S Di Sabatino, C Hocut, and T Zsedrovits. Intercomparison between different pbl options in wrf model: Modification of two pbl schemes for stable conditions. 2014.

[20] DTU Wind Energy. Wasp, May 2016. URL `http://www.wasp.dk`.

[21] Dale R Durran. *Numerical methods for wave equations in geophysical fluid dynamics*, volume 32. Springer Science & Business Media, 2013.

[22] ECMWF. Era-interim, 2016. URL `http://www.ecmwf.int/en/research/climate-reanalysis/era-interim`.

[23] ECMWF. Era-interim, June 2016. URL `http://www.ecmwf.int/en/forecasts/datasets/era-interim-dataset-january-1979-present`.

[24] ECMWF. Data assimilation, May 2016. URL `http://www.ecmwf.int/en/research/data-assimilation`.

[25] Charles Henry Edwards and David E.. Penney. *Differential equations and boundary value problems*, volume 2. Prentice Hall, 2004.

[26] Peter Frohboese and Andreas Anders. Effects of icing on wind turbine fatigue loads. In *Journal of Physics: Conference Series,* volume 75. IOP Publishing, 2007.

[27] M García-Díez, J Fernández, L Fita, and C Yagüe. Seasonal dependence of wrf model biases and sensitivity to pbl schemes over europe. *Quarterly Journal of the Royal Meteorological Society*, 139(671):501–514, 2013.

[28] Zenon Gniazdowski. Geometric interpretation of a correlation. *Zeszyty Naukowe Warszawskiej Wyższej Szkoły Informatyki*, (9):27–35, 2013.

[29] James R Holton and Gregory J Hakim. *An introduction to dynamic meteorology*, volume 88. Academic press, 2012.

[30] Xiao-Ming Hu, John W Nielsen-Gammon, and Fuqing Zhang. Evaluation of three planetary boundary layer schemes in the wrf model. *Journal of Applied Meteorology and Climatology*, 49(9):1831–1844, 2010.

[31] Katy Human. In the wake of a wind turbine, April 2011. URL `http://www.noaanews.noaa.gov/stories2011/20110426_windwakes.html`.

[32] IEA. World energy outlook 2014, executive summary. Technical report, International Energy Agency, November 2014.

[33] S Rao Jammalamadaka and Ashis Sengupta. *Topics in circular statistics*, volume 5. World Scientific, 2001.

[34] William J Jasinski, Shawn C Noe, Michael S Selig, and Michael B Bragg. Wind turbine performance under icing conditions. *Journal of Solar Energy Engineering*, 120(1):60–65, 1998.

[35] WP Jones and BEi Launder. The prediction of laminarization with a two-equation model of turbulence. *International journal of heat and mass transfer*, 15(2):301–314, 1972.

[36] P Kållberg, A Simmons, S Uppala, and M Fuentes. Era-40 project report series, 17. *The ERA-40 archive*, 2004.

[37] Sujay V Kumar, Christa D Peters-Lidard, Joseph L Eastman, and Wei-Kuo Tao. An integrated high-resolution hydrometeorological modeling testbed using lis and wrf. *Environmental Modelling & Software*, 23(2):169–181, 2008.

[38] Brian Edward Launder and DB Spalding. The numerical computation of turbulent flows. *Computer methods in applied mechanics and engineering*, 3(2):269–289, 1974.

[39] Xingong Li. Deriving directional variance from covariance matrix. *Transactions in GIS*, 9(3):443–445, 2005.

[40] Steve Lindenberg. *20% Wind Energy By 2030: Increasing Wind Energy¿ s Contribution to US Electricity Supply*. DIANE Publishing, 2009.

[41] Heidi Lippestad. Varmest - kaldest - vaatest - toerrest. URL `http://met.no/Klima/Klimastatistikk/Klimanormaler/Varmest_-_Vatest_-_Kaldest/`.

[42] James F Manwell, Jon G McGowan, and Anthony L Rogers. *Wind energy explained: theory, design and application*. John Wiley & Sons, 2010.

[43] Kanti V Mardia and Peter E Jupp. *Directional statistics*, volume 494. John Wiley & Sons, 2009.

[44] Jonathan E Martin. *Mid-latitude atmospheric dynamics: a first course*. John Wiley & Sons, 2013.

[45] F Mesinger. A blocking technique for representation of mountains in atmospheric models. *Rivista di Meteorologia Aeronautica*, 44(1-4):195–202, 1984.

[46] Fedor Mesinger, Zaviša I Janjic, Slobodan Ničkovic, Dušanka Gavrilov, and Dennis G Deaven. The step-mountain coordinate: model description and performance for cases of alpine lee cyclogenesis and for a case of an appalachian redevelopment. *Monthly Weather Review*, 116(7):1493–1518, 1988.

[47] Met Office. Beaufort wind force scale, December 2014. URL `http://www.metoffice.gov.uk/guide/weather/marine/beaufort-scale`.

[48] Meteorologisk institutt. Vindpiler og -skala, March 2013. URL `http://om.yr.no/forklaring/symbol/vind/`.

[49] J Michalakes, S Chen, J Dudhia, L Hart, J Klemp, J Middlecoff, and W Skamarock. Development of a next generation regional weather research and forecast model. In *Developments in Teracomputing: Proceedings of the Ninth ECMWF Workshop on the use of high performance computing in meteorology*, volume 1, pages 269–276. World Scientific, 2001.

[50] J Michalakes, J Dudhia, D Gill, T Henderson, J Klemp, W Skamarock, and W Wang. The weather research and forecast model: software architecture and performance. In *Proceedings of the 11th ECMWF Workshop on the Use of High Performance Computing In Meteorology*, pages 156–168, 2005.

[51] C Monteiro, R Bessa, V Miranda, A Botterud, J Wang, and G Conzelmann. *Wind Power Forecasting: Stat-of-the-Art 2009*. Argonne National Laboratory, 2009.

[52] WMO No. 306, manual on codes. *World Meteorological Organization operational data formats. http://www. wmo. int/pages/prog/www/WMOCodes/WMO306_vI2/LatestVERSION/LatestVERSION. html*, 2001.

[53] Earth System Research Laboratory NOAA. Wrf namelist.input file description. URL `http://esrl.noaa.gov/gsd/wrfportal/namelist_input_options.html`.

[54] Norwegian Geotechnical Institute. Ulykker, May 2016. URL `http://www.ngi.no/no/snoskred/Ulykker/`.

[55] Jiri Nossent, Pieter Elsen, and Willy Bauwens. Sobol'sensitivity analysis of a complex environmental model. *Environmental Modelling & Software*, 26(12):1515–1525, 2011.

[56] Jeffrey E Passner and David I Knapp. Using wrf-arw data to forecast turbulence at small scales. In *Preprints, 13th Conf. on Aviation, Range and Aerospace Meteorology. New Orleans, LA: Amerian Meteoro-logical Society*, page P3, 2008.

[57] Timothy Sauer. *Numerical Analysis*. Addison-Wesley Publishing Company, USA, 2nd edition, 2011. ISBN 0321783670, 9780321783677.

[58] JV Seguro and TW Lambert. Modern estimation of the parameters of the weibull wind speed distribution for wind energy analysis. *Journal of Wind Engineering and Industrial Aerodynamics*, 85(1):75–84, 2000.

[59] Henry Seifert, Annette Westerhellweg, and Jürgen Kröning. Risk analysis of ice throw from wind turbines. *Boreas*, 6(9):2006–01, 2003.

[60] Hyeyum Hailey Shin and Jimy Dudhia. Evaluation of pbl parameterizations in wrf at sub-kilometer grid spacings: Turbulence statistics in the dry convective boundary layer. *Monthly Weather Review*, (2016), 2016.

[61] Hyeyum Hailey Shin and Song-You Hong. Intercomparison of planetary boundary-layer parametrizations in the wrf model for a single day from cases-99. *Boundary-Layer Meteorology*, 139(2):261–281, 2011.

[62] R Shrivastava, SK Dash, RB Oza, and MN Hegde. Evaluation of parameterization schemes in the weather research and forecasting (wrf) model: A case study for the kaiga nuclear power plant site. *Annals of Nuclear Energy*, 75:693–702, 2015.

[63] William C Skamarock, Joseph B Klemp, Jimy Dudhia, David O Gill, Dale M Barker, Wei Wang, and Jordan G Powers. A description of the advanced research wrf version 2. Technical report, DTIC Document, 2005.

[64] William C Skamarock, Joseph B Klemp, Jimy Dudhia, David O Gill, Dale M Barker, Wei Wang, and Jordan G Powers. A description of the advanced research wrf version 3. Technical report, DTIC Document, June 2008.

[65] William C Skamarock, Joseph B Klemp, Jimy Dudhia, David O Gill, Dale M Barker, Wei Wang, and Jordan G Powers. Wrf model users' page, April 2016. URL `http://www2.mmm.ucar.edu/wrf/users/index.html`.

[66] A Soares, P Pinto, and R Pilão. Mesoscale modelling for wind resource evaluation purposes: a test case in complex terrain. In *International Conference on Renewable Energies and Power Quality*, 2010.

[67] Carina C Soares, Guilherme O Chagas, and Ricardo André Guedes. Estimating wind resource using mesoscale modeling. In *European Wind Energy Conference (EWEC), Brussels, Belgium*, 2011.

[68] Roland B Stull. *An introduction to boundary layer meteorology*, volume 13. Springer Science & Business Media, 2012.

[69] Semion Sukoriansky, Boris Galperin, and Veniamin Perov. Application of a new spectral theory of stably stratified turbulence to the atmospheric boundary layer over sea ice. *Boundary-Layer Meteorology*, 117(2):231–257, 2005.

[70] Endre Süli and David F Mayers. *An introduction to numerical analysis*. Cambridge university press, 2003.

[71] Troms Kraft AS. Konsesjonssoeknad, May 2014. URL `http://viadora.tromskraft.no/dokumenter/TKP/Rieppi/Konsesjonssoeknad.pdf`.

[72] Geoffrey K Vallis. *Atmospheric and oceanic fluid dynamics: fundamentals and large-scale circulation*. Cambridge University Press, 2006.

[73] Vestas. V90-3.0mw at a glance, October 2015. URL `https://www.vestas.com/en/products/turbines/v112-3_3_mw#!power-curve-and-aep`.

[74] Ronald E Walpole, Raymond H Myers, Sharon L Myers, and Keying Ye. *Probability and statistics for engineers and scientists*, volume 5. Macmillan New York, 1993.

[75] Wei Wang, Dale Barker, John Bray, Cindy Bruyere, Michael Duda, Jimy Dudhia, Dave Gill, and John Michalakes. User's guide for advanced research wrf (arw) modeling system version 3, 2011.

[76] Wei Wang, Cindy Bruyère, Michael Duda, Jimy Dudhia, Dave Gill, Michael Kavulich, Kelly Keene, Hui-Chuan Lin, John Michalakes, Syed Rizvi, and Xin Zhang. Arw version 3 modeling system user's guide. Technical report, Mesoscale and Microscale Meteorology Division, April 2013.

[77] J.Dudhia W.C. Skamarock, J.B. Klemp. Prototypes for the wrf (weather research and forecasting) model. *National Center for Atmospheric Research*, 2001.

[78] Louis J Wicker and William C Skamarock. Time-splitting methods for elastic models using forward time schemes. *Monthly Weather Review*, 130 (8):2088–2097, 2002.

[79] WindSim AS. Windsim, May 2016. URL `https://www.windsim.com`.